Universidade Estadual Paulista
Campus de Araraquara
Programa de Pós-Graduação em Química

LAPONITE® in photonic materials: solid-state emission of nanocomposites based on carbon dots and its application as Hg^{2+} sensing; application as conformable substrates for OLEDs

Ph.D. thesis

Bruno Seiki Domingos Onishi

Araraquara
2024

Bruno Seiki Domingos Onishi

LAPONITE® in photonic materials: solid-state emission of nanocomposites based on carbon dots and its application as Hg^{2+} sensing; application as conformable substrates for OLEDs

Thesis presented to the Intitute of Chemistry, São Paulo State University, to obtain the Ph.D in Chemistry

Advisor: Prof. Dr. Sidney José Lima Ribeiro

Araraquara

Onishi, Bruno Seiki Domingos
O58L LAPONITE® in photonic materials: solid-state emission of nanocomposites based on carbon dots and its application as Hg2+ sensing; application as conformable substrates for OLEDs / Bruno Seiki Domingos Onishi – Araraquara: [s.n.], 2024
183 p.: il.

Thesis (doctor) – Universidade Estadual Paulista, Instituto de Química
Advisor: Sidney José Lima Ribeiro

1. Clay minerals. 2. Photoluminescence. 3. Biopolymers. 4. Heavy metals. 5. Light emitting diodes. I. Title.

Sistema de geração automática de fichas catalográficas da Unesp. Biblioteca do Instituto de Química, Araraquara. Dados fornecidos pelo autor(a).

Essa ficha não pode ser modificada

2024

Bruno Seiki Domingos Onishi

LAPONITA® em materiais fotônicos: Emissão do estado sólido de nanocompositos baseados em pontos quânticos de carbono e sua aplicação como sensoriamento de Hg^{2+}; aplicação como substratos conformáveis para OLEDs

Tese apresentada ao Instituto de Química, Universidade Estadual Paulista, como parte dos requisitos para obtenção do título de Doutor em química

Orientador: Prof. Dr. Sidney José Lima Ribeiro

Araraquara

Expected impact

Ongoing search for sustainable development leads to innovations that connect economic growth to the care of nature and social welfare. Modern developments in the fields such as photoluminescent hybrid materials and biopolymer-based organic light-emitting diodes (OLEDs) have profound influences on society, economy, and academia. The text discusses them with respect to CDLPs for Hg^{2+} detection and CMC/HA-LAPONITE® substrates for OLEDs.

Societal Impact

Development of sensors based on CDLP addresses a major societal requirement for detecting heavy metals that are harmful especially mercury (Hg^{2+}) in environmental matrices. Mercury pollution is associated with serious health impacts including neurological disorders and developmental problems. By providing an effective, selective means of detecting minute quantities of Hg^{2+}, CDLP sensors contribute to public health protection and environmental monitoring resulting in safer water and food supplies.

In addition, it has been noted that CMC/HA-LAPONITE® substrates can be applied in making OLEDs and thus achieving additional benefits for electronic devices. These biopolymer-based supports facilitate the generation of flexible, long-lasting and see-through OLEDs. This facilitates wearable electronics, advanced health care devices to improve the quality of life, more efficient light sources, and advanced displays among others. Sustainable materials are integrated as well so as to correspond with increasing societal request for green products.

Economic Impact

Green technology industries will be facilitated by the use of sensors based on CDLP and substrates such as CMC/HA-LAPONITE®. This could stimulate market expansion, job creation and investment in sensor manufacturing by way of increased demand for advanced non-toxic environmental monitoring sensors. In addition, these sensors are more efficient and sustainable resulting in reduced economic costs associated with environmental cleanup and health care expenditures related to mercury pollution.

The use of CMC/HA-LAPONITE® in OLED technology also has a great economic potential. Flexible and long lasting OLEDs are poised to revolutionize the electronics market by enabling development of new consumer products as well as enhancing competitiveness for companies adopting such innovations. Replacing traditional non-sustainable materials used in OLED production with these substrates has a potential to lower manufacturing costs and improve the economic viability of green products.

Academic Impact

From the academic point of view, the synthesis and characterization of CDLP and CMC/HA-LAPONITE® composites contribute to the advancement of material science and nanotechnology. These innovations provide rich research opportunities, promoting academic collaboration and driving the publication of high-impact studies. For example, the paper in this thesis has been published in a high impact factor journal (Nanoscale) with international colaboration, contributiong for enhancement of high-quality research in Brazil. The study of photoluminescent properties and the understanding of quenching mechanisms in CDs can potentially pave the way for further breakthroughs in sensor technology.

Furthermore, the development of biopolymer-based OLED substrates combines multiple disciplines, including chemistry, materials science, and engineering. This interdisciplinary approach enriches academic interaction and inspires new research initiatives aimed at sustainable development.

Sustainable Development Context

Both CDLP-based sensors and CMC/HA-LAPONITE® substrates exemplify the principles of sustainable development. The use of non-toxic, biodegradable materials in sensor and OLED fabrication aligns with the goal of minimizing environmental impact. These innovations support the United Nations Sustainable Development Goals (SDGs), particularly Goal 3 (Good Health and Well-being), Goal 6 (Clean Water and Sanitation), Goal 9 (Industry, Innovation, and Infrastructure), and Goal 12 (Responsible Consumption and Production).

By enabling efficient detection of pollutants and contributing to the development of sustainable electronic devices, these technologies reduce ecological footprints and promote the responsible use of resources. The enhancement of public health and

environmental protection, coupled with economic growth driven by green technologies, emphasise the integral role of scientific innovation in achieving sustainable development.

Conclusion

The societal, economic, and academic impacts of CDLP-based sensors and CMC/HA-LAPONITE® substrates are profound, driving progress in public health, environmental protection, economic growth, and scientific knowledge. These innovations embody the spirit of sustainable development, offering practical solutions to pressing global challenges while encourage interdisciplinary research and eco-friendly technological advancements. As these technologies continue to evolve, their contributions to a sustainable and prosperous future will only grow more significant.

Impacto Esperado

A busca contínua pelo desenvolvimento sustentável leva a inovações que conectam o crescimento econômico ao cuidado com a natureza e ao bem-estar social. Desenvolvimentos modernos em campos como materiais híbridos fotoluminescentes e diodos emissores de luz orgânicos (OLEDs) à base de biopolímeros têm profundas influências na sociedade, na economia e na academia. O texto discute esses impactos com respeito aos compósitos de pontos quânticos de carbono e LAPONITA® (CDLP) para detecção de Hg^{2+} e aos substratos CMC/HA-LAPONITA® para OLEDs.

Impacto Social

O desenvolvimento de sensores baseados em CDLP atende a uma importante necessidade social de detectar metais pesados que são prejudiciais, especialmente mercúrio (Hg^{2+}), em matrizes ambientais. A poluição por mercúrio está associada a sérios impactos na saúde, incluindo distúrbios neurológicos e problemas de desenvolvimento. Ao fornecer um meio eficaz e seletivo de detectar quantidades mínimas de Hg^{2+}, os sensores CDLP contribuem para a proteção da saúde pública e o monitoramento ambiental, resultando em suprimentos de água e alimentos mais seguros.

Além disso, foi observado que os substratos CMC/HA-LAPONITA® podem ser aplicados na fabricação de OLEDs, alcançando benefícios adicionais para dispositivos eletrônicos. Esses suportes à base de biopolímeros facilitam a geração de OLEDs flexíveis, duráveis e transparentes. Isso facilita a criação de eletrônicos vestíveis, dispositivos avançados de cuidados de saúde para melhorar a qualidade de vida, fontes de luz mais eficientes e displays avançados, entre outros. Materiais sustentáveis também são integrados para corresponder à crescente demanda da sociedade por produtos ecológicos.

Impacto Econômico

As indústrias de tecnologia verde serão facilitadas pelo uso de sensores baseados em CDLP e substratos como CMC/HA-LAPONITA®. Isso pode estimular a expansão do mercado, a criação de empregos e o investimento na fabricação de sensores devido ao aumento da demanda por sensores de monitoramento ambiental avançados e não tóxicos. Além disso, esses sensores são mais eficientes e sustentáveis, resultando em menores

custos econômicos associados à limpeza ambiental e aos gastos com saúde relacionados à poluição por mercúrio.

O uso de CMC/HA-LAPONITE® na tecnologia OLED também tem um grande potencial econômico. OLEDs flexíveis e duráveis estão prontos para revolucionar o mercado de eletrônicos, permitindo o desenvolvimento de novos produtos de consumo, bem como aumentando a competitividade das empresas que adotam tais inovações. A substituição de materiais tradicionais não sustentáveis usados na produção de OLEDs por esses substratos tem o potencial de reduzir os custos de fabricação e melhorar a viabilidade econômica de produtos ecológicos.

Impacto Acadêmico

Do ponto de vista acadêmico, a síntese e caracterização de compósitos CDLP e CMC/HA-LAPONITE® contribuem para o avanço da ciência dos materiais e da nanotecnologia. Essas inovações oferecem ricas oportunidades de pesquisa, promovendo a colaboração acadêmica e impulsionando a publicação de estudos de alto impacto. Por exemplo, o artigo desta tese foi publicado em uma revista de alto fator de impacto (Nanoscale) com colaboração internacional, contribuindo para o crescimento de pesquisas de alta qualidade no Brasil. O estudo das propriedades fotoluminescentes e a compreensão dos mecanismos de supressão em pontos quânticos de carbono podem potencialmente abrir caminho para novos avanços na tecnologia de sensores.

Além disso, o desenvolvimento de substratos OLED à base de biopolímeros combina múltiplas disciplinas, incluindo química, ciência dos materiais e engenharia. Essa abordagem interdisciplinar enriquece a interação acadêmica e inspira novas iniciativas de pesquisa voltadas para o desenvolvimento sustentável.

Contexto do Desenvolvimento Sustentável

Tanto os sensores baseados em CDLP quanto os substratos CMC/HA-LAPONITA® exemplificam os princípios do desenvolvimento sustentável. O uso de materiais não tóxicos e biodegradáveis na fabricação de sensores e OLEDs está alinhado com o objetivo de minimizar o impacto ambiental. Essas inovações apoiam os Objetivos de Desenvolvimento Sustentável (ODS) das Nações Unidas, particularmente o Objetivo 3 (Saúde e Bem-estar), Objetivo 6 (Água Limpa e Saneamento), Objetivo 9 (Indústria, Inovação e Infraestrutura) e Objetivo 12 (Consumo e Produção Responsáveis).

Ao permitir a detecção eficiente de poluentes e contribuir para o desenvolvimento de dispositivos eletrônicos sustentáveis, essas tecnologias reduzem as pegadas ecológicas e promovem o uso responsável dos recursos. A melhoria da saúde pública e da proteção ambiental, juntamente com o crescimento econômico impulsionado por tecnologias verdes, enfatizam o papel integral da inovação científica na consecução do desenvolvimento sustentável.

UNIVERSIDADE ESTADUAL PAULISTA

Câmpus de Araraquara

CERTIFICADO DE APROVAÇÃO

TÍTULO DA TESE: "LAPONITE® in photonic materials: solid-state emission of nanocomposites based on carbon dots and its application as Hg2+ sensing; application as conformable substrates for OLEDs"

AUTOR: BRUNO SEIKI DOMINGOS ONISHI

ORIENTADOR: SIDNEY JOSE LIMA RIBEIRO

Aprovado como parte das exigências para obtenção do Título de Doutor em Química, pela Comissão Examinadora:

Prof. Dr. SIDNEY JOSE LIMA RIBEIRO (Participaçao Virtual)
Departamento de Química Analítica, Físico-Química e Inorgânica / Instituto de Quimica - UNESP- Araraquara

Prof. Dr. SERGIO ANTONIO MARQUES DE LIMA (Participaçao Virtual)
Departamento de Física, Química e Biologia / Faculdade de Ciências e Tecnologia - UNESP - Presidente Prudente

Profa. Dra. CINTYA D' ANGELES DO ESPIRITO SANTO BARBOSA (Participaçao Virtual)
Instituto de Quimica e Biotecnologia / Universidade Federal de Alagoas - UFAL - Maceió

Dr. CAUE RIBEIRO DE OLIVEIRA (Participaçao Virtual)
Empresa Brasileira de Pesquisa Agropecuária / EMBRAPA - CNPDIA - São Carlos

Prof. Dr. JOSÉ MAURÍCIO ALMEIDA CAIUT (Participaçao Virtual)
Departamento de Química / Faculdade de Filosofia, Ciências e Letras - USP - Ribeirão Preto

Araraquara, 10 de julho de 2024

gov.br Documento assinado digitalmente
SIDNEY JOSE LIMA RIBEIRO
Data: 18/07/2024 16:27:51-0300
Verifique em https://validar.iti.gov.br

DATA

Personal Information

- Full Name: Bruno Seiki Domingos Onishi
- Name in bibliography Citation: Onishi, B. S. D.; Bruno S. D. Onishi; Onishi, Bruno Seiki Domingos
- Nationality: Brazilian
- Birth city: Dracena - SP
- Profession: Chemist
- Adress: Instituto de Química – Universidade Estadual Paulista "Júlio de Mesquita Filho" – Av. Prof. Francisco Degni, 55 – Jardim Quitandinha – Araraquara -SP. CEP: 14800-060
- E-mail: bruno.onishi@unesp.br

Academic education

- Bachelor's degree in Chemistry (2018), State Univerity of Londrina (UEL - Universidade Estadual de Londrina), Londrina – PR
- Master's degree in Chemistry (2020), State Univerity of Londrina (UEL - Universidade Estadual de Londrina), Londrina – PR

Work Experience

- Undergraduate research (PROIC) in the physics department (UEL), in the field of Electronic Paramagnetic Resonance (EPR) – Advisor: Prof. Dr. Eduardo Di Mauro (2015-2016);
- Undergraduate research in the food science department (UEL), in the field of soy research – Advisor: Prof. Dr. Elza Iouko Ida (2016);
- Undergraduate research (PROIT) in the chemistry department (UEL), in the field of soil sorption of hazardous compounds - Advisor: Prof. Dr. Maria Josefa Santos Yabe (2016-2018);
- Scholarship holder of CAPES in master's degree (UEL - 2018 – 2020);
- Scholarship holder of CAPES in Ph.D degree (UNESP - 2020-2024);
- Research Internship and scholarship holder by CAPES PrInt in physics at Universidade de Aveiro (Aveiro – Portugal) – PHANTON group – Advisors: Prof.

Dr. Luís Carlos Dias and Prof. Dr. Maria Rute de Amorim e Sá Ferreira André. (2022-2023);

- Internship supervision – Beatriz Demasio de Freitas - Green host urethanesil based on castor oil doped with Eu3+ complex (UNESP - 2023-2024)

Participation in scientific events

- Rare-Earth Spectroscopy: 2nd Workshop on the JOYSpectra platform June 10th-11th 2024 (2024) – seminar participant;
- 2º Workshop sobre Materiais Conversores de Luz à Base de Terras Raras: Marcadores Luminescentes, Sensores e Amplificadores Ópticos. Sustainable urethanesil based on Castor Oil doped with Eu^{3+} complex for luminescent solar concentrator (2024) – poster presentation;
- 1st Machine Learning School for Materials @Ilum (2022) – seminar participant;
- Latin American Optics and Photonics. Development of hybrid organic-inorganic coating based on carbon dots on bacterial cellulose using sol-gel route (2022) – oral presentation;
- XXIV Congresso de Iniciação Científica da Unesp-IQ/Araraquara (2022) – Poster evaluator;
- V Escola de Inverno de Quimiometria (2022) – seminar participant;
- 6º Congresso de Analitica, 2019. Transporte de pesticidas organoestânicos: Azociclotina e Cihexatina em solos (2019) – poster presentation;
- XXV Encontro de Química Região Sul, SBQ-Sul.Modificação de hidróxido duplo lamelar para liberação controlada de fósforo em solos (2019) – poster presentaion;
- XXV Encontro anual de Iniciação Científica da UEL.Investigação da substituição de Fe^{3+} em goethita por Al^{3+} com espectroscopia Raman (2016) – oral presentation;
- XXIV Encontro Anual de Iniciação Científica EAIC - Investigação da substituição de Fe^{3+} por Al^{3+} em goethita com a espectroscopia de ressonância paramagnética eletrônica (RPE) (2015) - oral presentation;
- XX Semana da Física Ano Internacional da Luz 2015 (2015) – seminar participant;
- XXX Semana da Química: Novos Rumos para a Química da UEL (2014) - seminar participant;

Scientific production

- **B. S. D. Onishi**, Rafael S. Carvalho, Ricardo Bortoletto-Santos, Silvia H. Santagneli, Arthur R. J. Barreto, Aline M. Santos, Marco Cremona, Omar G. Pandoli, Mario N. B. Junior, Thales A. Faraco, Hernane S. Barud, Renan L. de Farias, Sidney J. L. Ribeiro Cristiano Legnani. Laponite-Modified Biopolymers as a Conformable Substrate for Optoelectronic Devices. *ACS Omega*. **2024.** DOI - https://doi.org/10.1021/acsomega.4c03463.
- **B. S. D. Onishi**, B. H. Costa, L. Marchiori, B. D. de Freitas, R. S. Pugina, J. R. Bartlett, L. D. Carlos, E. P. Ferreira-Neto, S. J. L. Ribeiro. Organic–inorganic hybrid silica systems: synthesis strategies and optical applications *J. Solgel Sci. Technol.* **2024.** DOI - https://doi.org/10.1007/s10971-024-06406-9;
- L. Marchiori, L. S. Santos, T. Schuler, J. C. Bernardes, B. O. Mattos, **B. S. D. Onishi**, R. Bortoletto-Santos, U. P. Rodrigues-Filho, R. D. Domeneguetti, S. Ullah, C. R. Ramno, E. P. Ferreira-Neto, S. J. L. Ribeiro. Effect of drying methods on the structure and properties of bacterial nanocellulose/MoS_2 hybrid gel membranes and sphere-like particles for enhanced adsorption and photocatalytic applications *J. Solgel Sci. Technol.* **2024**. DOI - https://doi.org/10.1007/s10971-024-06380-2
- **B. S. D. Onishi**, A.N. C. Neto, R. Bortoletto-Santos, V. R. Mastelaro, L. D. Carlos, R. A. S. Ferreira, S. J. L. Ribeiro. Carbon dots on LAPONITE® hybrid nanocomposites: solid-state emission and inter-aggregate energy transfer. *Nanoscale.* 2024, 16, 6286. DOI - https:// 10.1039/d3nr06336d;
- B. D. de Freitas, **B. S. D. Onishi,** R. Bortoletto-Santos, F. J. Caixeta, F. D. R. Garcia, Y. Messaddeq, S. J. L. Ribeiro. Green host urethanesil based on castor oil doped with Eu^{3+} complex. *Opt. Mater.* 2023, 138, 113706. DOI - http:// doi.org/10.1016/j.optmat.2023.113706;
- A. V. Rodrigues, **B. S. D. Onishi**, S. J. L. Ribeiro. Facile Formation of Sulfurized Nanorod-Like ZnO/$Zn(OH)_2$ and Hierarchical Flower-Like γ-$Zn(OH)_2$ /ϵ-Zn(OH) 2 from a Green Synthesis and Application as Luminescent Solar Concentrator. *ChemPhysChem.* 2023, 24, e202300134. DOI – http:// doi.org/10.1002/cphc.202300134;
- A. A. A. Lima, J. N. Quirino, R. Cavina, **B.S.D. Onishi**, M. J. Santos. Bentonite functionalized with magnetite nanoparticles synthesized from mining sludge: a

new magnetic material for removing iron and manganese ions from water. *J. Nanopart. Res.* **2023**, 81, 155. DOI: https://doi.org/10.1007/s11051-023-05745-y;

- C.U. Mussagy, D. Remonatto, F. P. Picheli, A. V. Paula, R. D. Herculano, V. C. Santos-Ebinuma, R. L. Farias, **B. S. D. Onishi**, S. J. L. Ribeiro; J. F. B. Pereira; A. Pessoa. A look into Phaffia rhodozyma biorefinery: From the recovery and fractionation of carotenoids, lipids and proteins to the sustainable manufacturing of biologically active bioplastics. *Bioresour. Technol.* **2022**, 362, 127785, DOI - https://doi.org/10.1016/j.biortech.2022.127785;
- A. A. A. Lima, **B.S.D. Onishi**, L. S. Watanabe, M. J. Santos. Mobility of organotin pesticides: azocyclotin and cyhexatin in clayey and sandy soils from the Northern Paraná state-Brazil. *Environ. Earth Sci.* **2022**, 81, 236. DOI - https://doi.org/10.1007/s12665-022-10351-7;
- **B.S.D. Onishi**, C. S. R. Ferreira, A. Urbano, M. J. Santos, Modified hydrotalcite for phosphorus slow-release: Kinetic and sorption-desorption processes in clayey and sandy soils from North of Paraná state (Brazil). *Appl. Clay Sci.***2020**, 197, 105759. DOI - https://doi.org/10.1016/j.clay.2020.105759

FOREWORD

This Ph.D thesis was written in the chapters/article format in accordance with the norms of "programa de pós-graduação em química" at the Institute of Chemistry, UNESP – Araraquara -SP.

The content of Chapter 2 was reproduced from a paper published in Nanoscale (impact factor: 6.7) after peer review. All the co-author's permissions were acquired as well as the Copyright © 2024 from The Royal Society of Chemistry. To access the final published work see: https://doi.org/10.1039/d3nr06336d.

The content of Chapter 3 has not yet been published. However, it will be submitted soon for Chemical Communications (Impact factor:4.9). All the co-authors permissions were acquired.

The content of Chapter 4 was reproduced from paper publish in ACS Omega (Impact Factor 4.1). All the co-authors permissions were acquired, and as open open-access journal, the author retain the copyright.

The results in Chapter 2 were collected at the host institution and during the studies abroad PHANTON group-CICECO at University of Aveiro, Aveiro-Portugal. The results in Chapter 3 were collected fully at the host institution. The results in Chapter 4 were partially collected at the host institution and partially at PUC-Rio and UFJF institutions.

Chapter 2 Carbon Dots on LAPONITE® Hybrid Nanocomposites: Solid-State Emission and Inter-aggregate Energy Transfer

Authors Bruno S. D. Onishi, Albano N. Carneiro Neto, Ricardo Bortoletto-Santos, Valmor R. Mastelaro, Luís D. Carlos, Rute A. S. Ferreira, Sidney J. L. Ribeiro

Journal Nanoscale, 2024, 16, 6286

DOI 10.1039/d3nr06336d

State Received 12th December, 2023, Accepted 3rd March 2024

Chapter 3 Carbon dots on LAPONITE® hybrid nanocomposite: Hg^{2+} sensing and photoluminescence emission quenching mechanism

Authors Bruno S. D. Onishi, Albano N. Carneiro Neto, Sidney J. L. Ribeiro

Journal This work is expected to be submitted to ACS Nanoscience Au

Chapter 4 Laponite-Modified Biopolymers as a Conformable Substrate for Optoelectronic Devices

Authors Bruno S. D. Onishi, Rafael S. Carvalho, Ricardo Bortoletto-Santos, Silvia H. Santagneli, Arthur R. J. Barreto, Aline M. Santos, Marco Cremona, Omar G. Pandoli, Mario N. B. Junior, Thales A. Faraco, Hernane S. Barud, Renan L. de Farias, Sidney J. L. Ribeiro Cristiano Legnani

Journal ACS OMEGA

DOI 10.1021/acsomega.4c03463

State Received 10th April, 2024, Accepted 24rd June 2024

I dedicate this thesys to my mother Luciana, my father Antônio and my brother "Lipe". As well as to my lovely girlfriend Thabata

ACKNOWLEDGMENT

First, I am deeply grateful to my advisor, Prof. Dr. Sidney Ribeiro, for his unwavering support and trust in my ability to execute this project. I also appreciate the invaluable lessons and guidance he provided during our advisory meetings, where he consistently valued the knowledge and growth of his students.

Secondly, I am grateful to Prof. Dr. Rute and Prof. Dr. Luís Carlos for their support and guidance at the University of Aveiro during my research internship in Portugal. Their co-supervision was instrumental in the execution of this thesis, and the knowledge I gained there was fundamental to the project's success.

I would like to thank the examination committee members for agree to evaluate this thesis.

I am deeply grateful to Prof. Dr. Ricardo Bortoletto for all the contributions to this thesis. Particularly in facilitating characterization measurements and providing insightful advice.

I would like to thank Dr. Albano for his support and for teaching me extensively about spectroscopic theory related to the photoluminescence process. His valuable contributions to the energy transfer calculations were essential for this thesis.

I extend my sincere appreciation to Prof. Dr. Renan Lira for his friendship, guidance and advice. Additionally, I am grateful for his exemplary leadership in the execution of Chapter 4 of this thesis.

I am also grateful to Dr. Sandra for her support with spectroscopic measurements in Portugal.

Additionally, I would like to thank Dr. Fernando Eduardo for his assistance with data analysis and for his hospitality during my time in Portugal.

I would like to thank all co-authors for their contributions to the published and submitted works, as well as for the permission to reproduce the works in this thesis.

I would like to thank all the help in the laboratory and friendship of Rafael Domeneguetti.

I would like to thank Beatriz Costa for all the scientific discussion and friendship.

I would like to thank Beatriz de Freitas, who helped me in some experiments and trusted me for her co-supervision in the internship.

I appreciate all my lab-mates and professors at the Laboratory of Photonic Materials in Araraquara.

I am grateful to the Institute of Chemistry of the São Paulo State University.

I am grateful to the University of Aveiro and CICECO, where i spent my research internship, as well as CAPES PrInt for the scholarship.

I express my sincere gratitude to my mom Luciana, my father Antônio, and my brother "Lipe" for always supporting and encouraging me in the pathways that i follow.

I express my deep gratitude for all the emotional support and motivation provided by my beloved girlfriend Thabata Mendes Natividade.

I would like to thank the financial support (scholarship) from Coordenação de Aperfeiçoamento de Pessoa de Nível Superior (CAPES) for the scholarship (Finance code: 001).

I also thank The Royal Chemistry Society for their kind permission to reproduce and use the content of the published article in Nanoscale for this thesis.

“There’s plenty of room at the bottom”

– Richard P. Feynman

ABSTRACT

LAPONITE® is a nanometric synthetic clay mineral widely explored in the biomedical field. However, its features such as suspension transparency and the ability to functionalize it with fluorophores and nanoparticles also make it a promising candidate for photonic applications. To avoid aggregation-caused quenching (ACQ) in solid-state carbon dots (CDs), LAPONITE® can be used to induce a steric hindrance between the nanoparticles. Thus, part of this thesis (chapter 2) delves into the photoluminescent characteristics of solid-state hybrid carbon dots/LAPONITE® (CDLP). These hybrid materials were synthesized using the hydrothermal method with a precise pH control set at 8.5. The LAPONITE® structure remained intact without a structural collapse in these conditions as indicated by the diffractograms of powder XRD. The use of different concentrations of citric acid during synthesis results in different CDs concentrations in CDLP-A (low precursors concentration) and CDLP-D (high concentration) with an amorphous structure and average size around 2.8-3.0 nm, according to STEM. By XPS and FTIR, carboxylate groups formed in the CDLP surface. The CDLP displayed visible photoluminescence (PL) emission in aqueous and powder, which the last underwent quenching according to lifetimes and quantum yield measurements. Low-temperature measurements revealed an enhancement of the non-radiative pathways induced by aggregation, associated with coupled surface states. Energy transfer modeling based on Förster-Dexter suggests an approximate mean distance of 9.5 nm between clusters of CDs. According to the quantum yield measurements (CDLP-A = 0.09 $\pm$ 0.01 and CDLP-D = 0.02 $\pm$ 0.01), and in comparison with CD without LAPONITE®, the synthetic clay mineral was crucial resist ACQ.

The synthesized nanocomposites presented structure characteristics, such as carboxylate groups for the application as photoluminescence chemical sensors (PCS) using PL quenching. Due to the harmful effect on the environment and human health of Hg^{2+}, its detection in low concentrations is needed, which can be achieved using PCS While several studies have reported that Hg^{2+} detection using CDs PL emission there is a lack of in-depth investigation into the quenching mechanisms involved in turn-off sensors. In this study (chapter 3), a Stern-Volmer analysis at three different temperatures (288, 298, and 303 K) is proposed. The results indicated selectivity for Hg^{2+} over the other evaluated metals. The optimum detection range for Hg^{2+} was found to be 1-40 μM, with limits of detection (LOD) and quantification (LOQ) of 2.5 and 8.3 μM respectively.

Using the Stern-Volmer models, it was found that static quenching dominates over collisional quenching, possibly due to the complexation between the nanocomposite's carboxylate groups and Hg^{2+}. Additionally, the modified Stern-Volmer model, which accounts for the fractional accessibility of the fluorophores by the quenchers, suggests that some parts of the sensor are inaccessible to the quencher.

Reinforcement material for organic light-emitting diodes (OLEDs) substrates is another photonics application of LAPONITE®. Biopolymers such as carboxymethyl cellulose and hyaluronic acid are alternative substrates for conformable OLEDs. However, drawbacks such as mechanical stress susceptibility can hinder the device's performance under stretched conditions. To overcome these limitations, herein (chapter 4) a nanocomposite based on CMC/HA (Carboxymethyl cellulose/Hyaluronic acid) and LAPONITE® was developed, intending to improve the mechanical strength without compromising the film flexibility and transparency (transmittance >80% - 380-700 nm) as substrates for conformable OLEDs. From XRD, FTIR, CP-MAS NMR, and TGA/DTG characterization techniques, it was possible to conclude the presence of LAPONITE® randomly dispersed between the polymer chains. The CMC/HA with 5 % (wt/wt) of LAPONITE®, CMC/HA 5, presented higher tensile strength (370.6 MPa) and comparable Young's Modulus (51.0 ± 1.2 Mpa) in comparison to the nanocomposites and pristine films, indicating a better candidate for device's substrates. To produce the OLED, the multilayer structure ITO/MoO_3/NPB/ TCTA:$Ir(ppy)_3$/TPBi:$Ir(ppy)_3$/Bphen/ LiF was deposited onto CMC/HA 5 substrate. of the OLEDs fabricated using CMC/HA 5 substrates showed higher luminance (12 kcd/m^2) and irradiance (0.9 mW/cm^2) values when compared with those based on commercial bacterial cellulose (BC). However, the same device presented lower efficiency (3.2 cd/A) due to higher current density. Moreover, the OLED fabricated onto LAPONITE® modified biopolymer presented a reproducible behavior when submitted to continuous bending stress. Thus, CMC/HA 5 demonstrates potential as a transparent conductor substrate for biopolymer-based OLED with comparable performance to commercial BC features.

RESUMO

LAPONITA® é um argilomiral sintético nanométrico amplamente explorado no campo biomédico. No entanto, suas características, como transparência da suspensão e a capacidade de funcionalizá-lo com fluoróforos e nanopartículas, também o tornam um candidato promissor para aplicações fotônicas. Para evitar a supressão causada por agregação (SCA) em pontos quânticos de carbono (PQC) no estado sólido, a LAPONITA® pode ser utilizada para induzir um impedimento estérico entre as nanopartículas. Dessa forma, parte desta tese (cápitulo 2) investiga as características fotoluminescentes de híbridos em estado sólido PQC/LAPONITA® (CDLP). Esses materiais híbridos foram sintetizados usando o método hidrotérmico com um controle preciso do pH ajustado em 8,5. A estrutura da LAPONITA® permaneceu intacta sem colapso estrutural nessas condições, conforme indicado pelos difratogramas de XRD em pó. O uso de diferentes concentrações de ácido cítrico durante a síntese resulta em diferentes concentrações de PQCs em CDLP-A (baixa concentração de precursores) e CDLP-D (alta concentração) com uma estrutura amorfa e tamanho médio em torno de 2,8-3,0 nm, de acordo com o STEM. Por XPS e FTIR, g rupos carboxilato foram formados na superfície de CDLP. Amostras de CDLP apresentou emissão fotoluminescente (FL) visível em estado aquoso e em pó, com este último sofrendo supressão de emissão conforme o decaimento de emissão e rendimento quântico. As medições de FL em baixa temperatura revelaram um aumento de contribuições não-radiativas induzidas pela agregação, associadas a estados de superfície acoplados. A modelagem de transferência de energia baseada em Förster-Dexter sugere uma distância média aproximada de 9,5 nm entre os aglomerados de PQCs. De acordo com as medições de rendimento quântico (CDLP-A = 0,09 ± 0,01 e CDLP-D = 0,02 ± 0,01), e em comparação com CD sem LAPONITA®, o argilomineral sintético foi crucial para resistir à SCA.

Os nanocompósitos sintetizados apresentaram características estruturais, como grupos carboxilato, para aplicação como sensores químicos de fotoluminescência (SQF) usando supressão de FL. Devido ao efeito nocivo do Hg^{2+} no meio ambiente e na saúde humana, é necessário detectá-lo em baixas concentrações, o que pode ser alcançado usando SQF. Embora vários estudos tenham relatado a detecção de Hg^{2+} usando a emissão FL de PQCs, há uma falta de investigação aprofundada sobre os mecanismos de supressão envolvidos

nos sensores de desligamento. Neste estudo, é proposta uma análise de Stern-Volmer a três temperaturas diferentes (288, 298 e 303 K). Os resultados indicaram seletividade para Hg^{2+} em relação aos outros metais avaliados. O intervalo ótimo de detecção para Hg^{2+} foi encontrado entre 1-40 μM, com limites de detecção (LD) e quantificação (LQ) de 2,5 e 8,3 μM, respectivamente. Utilizando os modelos de Stern-Volmer, foi constatado que a supressão estática domina sobre a supressão colisional, possivelmente devido à complexação entre os grupos carboxilatos híbrido e o $Hg^{2+.}$ Além disso, o modelo de Stern-Volmer modificado, que considera a acessibilidade fracionada dos fluoróforos pelos supressores, sugere que algumas partes do sensor são inacessíveis ao supressor.

Material de reforço para substratos de diodos emissores de luz orgânicos (OLEDs) é outra aplicação fotônica da LAPONITA®. Biopolímeros como carboximetilcelulose e ácido hialurônico são substratos alternativos para OLEDs. No entanto, desvantagens como a suscetibilidade ao estresse mecânico podem prejudicar o desempenho do dispositivo sob condições de estiramento. Para superar essas limitações, neste estudo (capítulo 4), um nanocompósito baseado em CMC/HA (Carboximetilcelulose/Ácido Hialurônico) e LAPONITA® foi desenvolvido, visando melhorar a resistência mecânica sem comprometer a flexibilidade e transparência do filme (transmitância >80% - 380-700 nm) como substratos para OLEDs conformáveis. A partir das técnicas de caracterização XRD, FTIR, CP-MAS NMR e TGA/DTG, foi possível concluir a presença da LAPONITA® disperso aleatoriamente entre as cadeias poliméricas. O CMC/HA com 5% (wt/wt) de LAPONITA®, CMC/HA 5, apresentou maior resistência à tração (370,6 MPa) e Módulo de Young comparável (51,0 ± 1,2 MPa) em comparação aos nanocompósitos e filmes puros, indicando uma melhor candidata para substratos de dispositivos. Para produzir o OLED, a estrutura multicamadas ITO/MoO_3/NPB/ TCTA$(ppy)_3$/TPBi$(ppy)_3$/Bphen/ LiF foi depositada no substrato CMC/HA 5. Os OLEDs fabricados usando substratos CMC/HA 5 mostraram valores mais altos de luminância (12 kcd/m²) e irradiância (0,9 mW/cm²) quando comparados aos baseados em celulose bacteriana comercial (CB). No entanto, o mesmo dispositivo apresentou menor eficiência (3,2 cd/A) devido à maior densidade de corrente. Além disso, o OLED fabricado sobre o biopolímero modificado com LAPONITA® apresentou um comportamento reprodutível quando submetido a estresse contínuo de flexão. Assim, o CMC/HA 5 demonstra potencial como um substrato condutor transparente para OLEDs baseados em biopolímeros, com desempenho comparável às características comerciais de CB.

Resumo expandindo da tese em português

Para o resumo expandido, foi apresentado a metodologia, resultados e discussões apresentados nos capítulos 2, 3 e 4, com uma breve introdução apresentando a motivação para os trabalhos executados.

A LAPONITA® é uma argilomineral sintético de fórmula empírica $Na_{0,7}^{+}[(Si_8Mg_{5,5}Li_{0,3})O_{20}(OH)_4]_{0,7}^{-}$ da família de esmectitas, um grupo de silicatos lamelares constituídos por camadas alternadas na forma TOT, em que a camada O representa os agrupamentos Mg-O arranjados de forma octaédrica e dispostas entre duas camadas T contento grupos Si-O na forma tetraédrica. O centro octaédrico é coordenado por ânions oxigênio e hidroxilas, e o tetraédrico preferencialmente por oxigênio. O centro octraedro de Mg^{2+} pode sofrer substituição isomórfica por Li^{+} levando à cargas negativas na superfície entre as lamelas contrabalanceadas por Na^{+}. As lamelas tem formato de nanodiscos com diâmetro de 25 nm e espessura de 1 nm, e quando dispersa em água são esfoliadasde forma a interagirem entre si por forças eletrostáticas de atração entre a face e a borda e repulsão entre a face-face e borda-borda de acordo com o pH da solução. A estrutura formada e a alta capacidade de troca catiônica permite a LAPONITA® formar compósitos com polímeros e nanopartículas, resultando em uma melhora principalmente em propriedades mecânicas e evitando agregação, respectivamente.

Dessa forma, para evitar a supressão causada por agregação (SCA) em pontos quânticos de carbono (PQC) no estado sólido, a LAPONITA® pode ser utilizada para induzir um impedimento estérico entre as nanopartículas. Embora os PQC, definidos como nanopartículas fotoluminescente de carbono de 1 a 30 nm, apresentam características desejáveis para aplicações na fotônica como boa dispersão em água e fotoluminescência (FL) em ampla região do espectro visível, o mecanismo de emissão por FL continua indefinido. Dentre as principais hipóteses, o confinamento quântico, emissão por estados de superfície e emissão devido a subprodutos fluorescentes apresentam mais evidências experimentais. Portanto, os estudos espectroscópicos com objetivo de desvendar esse mecanismo são essenciais para o avanço na área. Outro desafio é a emissão do estado sólido. PQC sólidos na forma de pó normalmente sofrem supressão da FL devido ao empilhamento $\pi - \pi$. A estratégia para contornar esse problema é a indução de um efeito estérico entre as nanopartículas para impedir o contato direto. Como por exemplo, a síntese de forma *in situ* utilizando uma matrix inorgânica lamelar como argilominerais.

Considerando os pontos apresentados, o objetivo do trabalho apresentado no capítulo 2 foi sintetizar e caracterizar o nanocompósito baseado em PQC/LAPONITA® (CDLP), assim como investigar as mudanças nas propriedades de emissão por FL no estado sólido em pó e aquoso, uma vez que a LAPONITA® poderia induzir a um impedimento estérico entre as nanopartículas, evitando a SCA. Também, estabelecer uma estimativa da transferência de energia envolvida utilizando o modelo Förster-Dexter.

Os nanocompósitos foram sintetizados utilizando a síntese hidrotermal sob uma temperatura de 180 ºC por 6 h. Os precursores foram ácido cítrico e etilenodiamina em uma proporção de 1:1 mol e 0.5 g de LAPONITA®, no qual foi fixado a quantidade de argilomineral e variado a concentração dos precursores mantendo a proporção molar. O argilomineral foi disperso em água ultrapura sob agitação vigorosa e posterior sonicação. Posteriormente, adicionado os precursores e ajustado em seguida o pH para 8.5. O mais concentrado foi nomeado CDLP-D enquanto com menor concentração de precursores CDLP-A. PQC isolados também foram sintetizados pela mesma metodologia sem o argilomineral e sem ajuste de pH, nomeados como CD, porém os mesmos foram submetidos ao processo de diálise, enquanto que os nanocompósitos a lavagem com água e etanol. Adicionalmente, o mesmo processo de síntese dos nanocompósitos foi realizados para a LAPONITA® sem os precursores, nomeada Lap. Os pós resultantes da síntese foram submetidos à caracterização estrutural e morfológica por Infravermelho com transformada de Fourier (abreviaturas das técnicas em inglês - FTIR), difração de raios-X em pó (XRD), espectroscopia de fotoelétrons excitados por raios X (XPS), análise elementar (CHN), análise termogravimétrica (TGA) e microscopia óptica, microscopia eletrônica de varredura de alta resolução utilizando feixe eletrônico por emissão de campo (MEV-FEG) e microscopia eletrônica de transmissão por varredura (STEM). A caracterização óptica por espectroscopia de absorção no UV-Vis (amostras suspensas em água) e espectroscopia de fotoluminescência (pó e suspensas em água). As medidas de FL foram realizadas em temperatura de 298 K e 13 K, analisando excitação, emissão e decaimento da emissão. Também, o rendimento quântico absoluto foi medido utilizando uma esfera integradora em 298 K.

A partir dos difratogramas obtidos pela análise de XRD em pó dos nanocompósitos, foi possível verificar um aumento do espaço interlamelar quando comparadas com as amostras de LAPONITA® pura e submetida pelo processo hidrotérmico sem os precursores de PQC. Adicionalmente, foi obtido o mesmo padrão cristalográfico independente da concentração utilizada dos precursores. Foi possível constatar a

importância do pH do meio reacional, uma vez que a síntese executada sem o ajuste causou o colapso da estrutura da LAPONITA®, confirmado por XRD. Por microscopia óptica utilizando uma fonte de excitação UV, foi possível verificar a emissão das lamelas, indicando deposição dos PQC. As imagens de MEV-FEG também revelaram mudanças morfológicas de uma superfície lisa de Lap para rugosa do nanocompósito, além de um contorno ao redor que pode indicar agregados de carbono. Pelo STEM foi possível verificar a morfologia amorfa dos PQC depositados no nanocompósito assim como o tamanho médio de ~3,0 nm para ambas as amostras CDLP-D e CDLP-A, enquanto a amostra CD o tamanho médio foi de ~15,0 nm. Grupos funcionais principalmente a base de carboxilatos foram identificados nos nanocompósitos independente da concentração de precursores.

Os espectros eletrônicos de UV-Vis nas amostras aquosas revelaram banda de absorção atribuída à transição $\pi \rightarrow \pi^*$ e $n \rightarrow \pi^*$ devido à grupos C=C e C=O/C=N respectivamente. As amostras de nanocompósitos apresentaram emissão em suspensão aquosa e no estado sólido em pó resistiram a auto supressão completa, como indica os valores de rendimento quântico obtidos (> 0.01). Em comparação com CD em pó, a supressão foi total de acordo com o rendimento quântico (< 0.01). No entanto, em ambas as amostras é possível verificar uma supressão da banda de emissão em 450 nm como mostra os valores de rendimento quântico excitando em 360 nm e pela diminuição do tempo de vida quando essa banda foi monitorada. A banda centrada em 517 nm por outro lado, se torna mais proeminente no estado sólido. Em comparação com a suspensão, o rendimento quântico associado a esses estados de menor energia não muda significativamente, indicando que no estado sólido essas transições não sofrem supressão da emissão. Os estados de maior energia (estados intrínsecos) forma associados à subprodutos de síntese ou a própria emissão do núcleo, e os estados de menor energia à estados de superfície devido aos grupos carboxilatos presentes.

Uma investigação mais aprofundada foi realizada utilizando medições de FL a 13 K já que os processos de desativação não-radiativa poderiam ser minimizados, permitindo o exame das contribuições radiativas. Os espectros de emissão revelaram um aumento relativo da banda de emissão centrada em 575 nm em ambas as amostras, com uma intensidade relativa I_{575}/I_{450} = 0,4 e 1,9 para CDLP-A e CDLP-D, respectivamente. Este aumento é muito menor à temperatura ambiente, com relações de intensidade de I_{575}/I_{450} = 0,1 e 0,2 para CDLP-A e CDLP-D, respectivamente. Como a diferença entre as amostras reside nas concentrações dos precursores e que CDLP-D exibe uma maior

quantidade de carbono, conforme análise de XPS e CHN, espera-se que uma maior concentração de CDs se forme na superfície de LAPONITE®, potencialmente levando à agregação. Portanto, esse aumento da banda de emissão nos estados de menor energia pode estar associados ao acoplamento entre estados de superfície devido à agregação. Pela comparação do decaimento de emissão a 575 nm em 13 K e 298 K, foi verificado uma diminuição do tempo de vida há maior temperatura, indicando perda de energia dissipada pelo meio que pode ser absorvida pelos estados intrínsecos de CDs agregados vizinhos. Para investigar essa transferência de energia, foi estimado um valor da taxa de transferência de energia a partir da diferença do inverso do tempo de vida a 298 K e 13 K, que significa a taxa em que o doador perde energia para o aceitador. Utilizando o modelo de Förster-Dexter e a taxa de transferência estimada, foi possível calcular o valor médio da distância entra agregados igual a 9.6 nm.

Portanto, foi possível desenvolver os híbridos nas condições de pH estabelecida com estabilidade estrutural como mostrado os resultados de DRX. Também, prevaleceram grupos de carboxilatos na superfície dos híbridos como evidenciado por XPS e FTIR. E além dos nanocompósitos apresentarem emissão em suspenssão aquosa, de acordo com as medições de rendimento quântico (CDLP-A = 0,09 ± 0,01 e CDLP-D = 0,02 ± 0,01), e em comparação com CD sem LAPONITA®, o argilomineral sintético foi crucial para resistir à SCA dos PQCs em estado sólido.

Os nanocompósitos sintetizados exibiram características estruturais, como grupos carboxilato, tornando-os adequados para uso como sensores químicos de fotoluminescência (SQF) que utilizam a supressão de FL. Devido aos efeitos nocivos dos metais pesados no corpo humano e no meio ambiente, estratégias de monitoramento em corpos d'água são necessárias para detecção e quantificação com alta sensibilidade e seletividade, que podem ser alcançados pelos SCF. Íons metálicos como Cd^{2+}, Cr^{6+}, Co^{2+}, Cu^{2+}, Pb^{2+}, Hg^{2+}, Zn^{2+}, As^{3+} e Ag^{+}, mesmo em concentrações mínimas, causam efeitos prejudiciais. O Hg^{2+} é altamente tóxico e pode causar danos ao DNA celular e iniciar processos cancerígenos. Técnicas analíticas como espectroscopia de absorção atômica (AAS) e espectrometria de massa com plasma acoplado indutivamente (ICP-MS) são usadas para quantificação de metais pesados, mas apresentam desvantagens como alto custo e necessidade de preparação extensa de amostras. SQF são uma alternativa de baixo custo, utilizando a interação da radiação eletromagnética com o analito para gerar um sinal analítico. A intensidade da emissão de FL é a medida mais comum, onde a supressão da emissão indica a presença do analito.

Os PQCs têm sido aplicados em várias áreas da fotônica, incluindo como sensores químicos e físicos, devido às rotas sintéticas simples e às propriedades ópticas, como fotoluminescência ajustável e rendimento quântico notável. A predominância de grupos carboxilatos no nanocompósito desenvolvido no capítulo 2 pode interagir com íons Hg^{2+}, motivando a investigação de sua aplicação como sensor químico para Hg^{2+}. Dessa forma, o capítulo 3 propôs uma investigação de Stern-Volmer em três temperaturas diferentes (288, 298 and 303 K), para estudar os mecanismos de supressão de fotoluminescência induzidos pelo Hg^{2+} sobre CDs, ainda não totalmente elucidados na literatura.

Primeiramente, foram conduzido ensaios de fotoestabilidade para avaliar as condições do meio que poderiam interferir com o sensoriamento de Hg^{2+} em água. Os parâmetros avaliados foram pH, concentração do sensor, tempo de exposição à excitação e força iônica. De acordo com os espectros de emissão a intensidade de emissão do CDLP-D permanece estável no intervalo de pH 4 a 7, com leve supressão em pH 8 e 9 e supressão considerável em pH 2 e 3; 10 e 11. A intensidade de emissão aumentou com a concentração no intervalo de 0.01 a 2 mg mL^{-1}, seguindo uma supressão à medida que a concentração aumentou de 3 a 5 mg mL^{-1}. A amostra de CDLP-D teve uma redução de 16% na área integrada relativa da emissão após 8 horas de exposição por fonte UV. Do ponto de vista experimental, a concentração de trabalho do CDLP-D para ensaios de detecção foi de 0.1 mg mL^{-1}, onde o pH da suspensão era igual a 6.0. Cada medição leva cerca de 3 minutos de irradiação contínua de luz UV por amostra. Levando em conta que apenas 2% da área integrada foi reduzida em 1 hora de exposição, a amostra pode ser considerada fotostável dentro do período medido, equivalendo a uma redução proporcional de 0.1%. Além disso, apesar da interferência de uma alta concentração de KCl resultando em uma redução de 10% na emissão de FL, a concentração dos sais metálicos utilizados ficou dentro da faixa de μM.

Para verificar a seletividade do CDLP-D para Hg^{2+}, foram realizados ensaios de detecção com outros íons metálicos na concetração de 100 μM, como Mn^{2+}, Fe^{3+}, Fe^{2+}, Co^{2+}, Ni^{2+}, Zn^{2+}, Cd^{+} e Pb^{2+}. Notavelmente, na concentração de 100 μM de $Hg^{2+,}$ houve uma redução de 58% na área integrada relativa de emissão do CDLP-D, indicando grande supressão devido à interação com Hg^{2+}. Em comparação com outros metais, a área integrada foi afetada em menos de 5%, exceto para $Fe^{3+,}$ que afetou em 18%. No entanto, na faixa do sensor de 1 a 40 μM, a área integrada é afetada em menos de 7%, além disso, os outros metais também não afetaram significativamente a supressão de Hg^{2+} quando avaliados concomitantemente com o íon metálico.

Na faixa de 1 a 90 μM, os espectros de emissão diminuíram em intensidade à medida que a concentração de Hg^{2+} aumenta. A faixa ótima encontrada para a detecção de Hg^{2+} foi entre 0 a 40 μM, onde foi possível estabelecer uma boa curva de calibração linear com um excelente coeficiente de correlação (R^2 = 0.992) e equação linear de y = 0.016x + 0.024, que pode ser usada para quantificar a concentração de Hg^{2+}, onde y = $(F_0-F)/F_0$ e x é a concentração de Hg^{2+} (F_0 é a área integrada de emissão sem a presença do íon Hg^{2+} e F na presença com concentração x). Os limites de detecção (LOD) e de quantificação (LOQ) encontrados, medindo 10 amostras em branco, foram 2.5 e 8.3 μM, respectivamente.

As curvas de Stern-Volmer apresentaram um desvio da linearidade em todas as temperaturas. Isso pode ser associado a uma alta concentração do supressor ou, quando o desvio é em direção ao eixo x, a presença de mais de uma população de emissores. Conforme mencionado no capítulo 2 a emissão do CDLP-D origina-se dos subprodutos na superfície ou do núcleo da nanopartícula (alta energia) e dos estados de superfície devido aos grupos funcionais orgânicos (baixa energia). Portanto, o desvio é esperado. O aumento da temperatura resultou em valores de Ksv mais baixos, o que não é característico do comportamento de supressão colisional, pois temperaturas mais altas promovem uma difusão mais rápida. Pelo contrário, é consistente com um comportamento estático com a formação de um complexo não emissor, no qual a temperatura mais alta promove a dissociação da ligação supressor-emissor. No caso de supressão colisional, o supressor afeta o estado excitado do emissor por interação colisional, com possíveis mecanismos de transferência de energia ou carga envolvidos. Os resultados da curva de decaimento da emissão revelaram que, em alta concentração de Hg^{2+} (100 μM), o estado excitado foi afetado. O tempo de vida sem Hg^{2+} obtido foi τ_0 = 12.74 ± 0.03 ns, e com 100 μM diminuiu para $\tau_{100\ \mu M}$ = 9.16 ± 0.03 ns. No entanto, em baixas concentrações de Hg^{2+} (10 μM), $\tau_{10\ \mu M}$ = 12.05 ± 0.03 ns. Portanto, a supressão colisional pode ocorrer em altas concentrações de Hg^{2+}. De acordo com os resultados, o processo de supressão estática parece ser dominante em baixas concentrações de Hg^{2+} em vez do processo colisional, mas este último não pode ser desconsiderado. Isso poderia explicar a seletividade de Hg^{2+} em relação a outros metais, que possivelmente se coordenam através dos grupos carboxilatos de superfície do CDLP-D ou através dos subprodutos formados. A equação de Stern-Volmer modificada que considera a acessibilidade fracionária dos fluoróforos pelos supressores idicaram que 0.3 da fração

total de emissão do sensor está disponível para o supressor. Esses resultados indicaram que há partes do CDLP-D que não são acessíveis para a surpressão por Hg^{2+}.

Como mostrado nos capítulos anteriores, a LAPONITA® pode ser aplicada na fotônica a fim de evitar a SCA em PQC e como SQF. Além disso, como evidenciado na literatura, argilominerais são amplamentes aplicados como materiais de reforço de polímeros. Portanto, para integrar essa propriedade com a fotônica, o trabalho desenvolvido no capítulo 4 teve como objetivo de desenvolver substratos biopolímericos a base de carboximetilcelulose (CMC) e ácido hiaulurônico (HA) com LAPONITA® para OLEDs. Apesar da conformabilidade e transparência de polímeros petroquímicos usados em substratos de OLED, os mesmos levantam preocupações em relação à sua não degradabilidade, resultando em poluição ambiental indesejada. Consequentemente, o interesse na "eletrônica verde" tem aumentado, visando criar substratos renováveis, biodegradáveis, biocompatíveis, transparentes e flexíveis. Nesse contexto os biopolímeros CMC e HÁ são ótimos candidatos para atender os requisitos mencionados. Entretando, os substratos a base CMC e HA podem apresentar desvantagens como baixa resistência mecânica e estabilidade térmica, que pode superado com a adição da LAPONITA®.

Os filmes de CMC/HA-LAPONITA® foram produzidos utilizando uma mistura de CMC e HA em 50 % (massa/volume) na proporção de água deionizada. A quantidade de LAPONITA® previsamente dispersa e sonicada em água, foi adicionada na mistura na proporção de 2,5, 5 e 20 % em relação a massa de CMC/HA (nomeados CMC/HA 2.5; CMC/HA 5 e CMC/HA 20). A mistuta foi seca em placas de poliestireno a 30 ºC por 48h em estufa de circulação de ar. Para preparação do dispositivo OLED, foram transferidas para uma câmara de vácuo. Foi depositada uma camada de SiO_2 para funcionalizar o substrato, seguido de uma deposição de ITO, ambas pelo método de sputter em atmosfera de argônio. As camadas orgânicas, LiF, MoO_3 e Al foram depositadas pelo método de evaporação térmica em alta vácuo. A arquitetura do OLED sobre o substrato CMC/HA 5 foi a seguinte estrutura: ITO (150 nm)/MoO_3 (2 nm)/ NPB (30 nm)/ TCTA:$Ir(ppy)_3$ (7 wt% (20 nm) /TPBi:$Ir(ppy)_3$ (7% wt% (10 nm)/ Bphen (40 nm)/ LiF (0.1 nm)/Al (100 nm).

Os filmes apresentaram transmitância na região do visível de 90, 87 e 80% para CMC/HA 2.5, 5 e 20. Utilizando ATR-FTIR foi possível confirmer a presença da LAPONITA® pela presença de bandas relacionadas à vibrações de ligações Si-O e Mg-O. Entretanto, o padrão de difração obtidos por XRD em pó da LAPONITA® nas

amostras 2.5 e 5 não foi possível identificar, sugerindo que o argilomineral se encontra esfoliado ou devido à baixa concentração. Apenas em CMC/HA 20 foi possível verificar um aumento no espaço interlamelar da LAPONITA®, indicando que os polímeros podem estar combinados parcialmente através do argilomineral esfoliados ou nos tactóides de LAPONITA® formado. Os resultados de ^{29}Si e ^{13}C NMR indicaram que não há uma interação química entre os polímeros e a LAPONITA®, e possivelmente o argilomineral se encontra disperse de forma aleatórica na cadeia polimérica CMC/HA. A análise térmica indicou uma diminuição na organização das cadeias poliméricas em função da concentração de do argilomineral, que pode estar associado à dispersão aleatória entre as cadeias poliméricas, o que reduz as interações cruzadas entre elas devido à interação física da LAPONITA® com os polímeros. A análise de tensão mecânica revelou melhor performace da amostra CMC/HA 5, sendo o mais resistente à tração mas com um grau de flexibilidade. A amostra com 20 % de LAPONITA® apresentou menor valor de resistência a tração provavelmente devido a agregações pontuais que reducem a interação entre os biopolímeros.

A análise de AFM revelou o sucesso da deposição de ITO sobre CMC/HA 5. Embora a superfície granular com a deposição de ITO, a resistividade elétrica ficou próxima de ITO depositados em vidro comercial. As caracterizações do dispositivo de OLED, resultaram em uma maior luminância (12 kcd/m^2) e irradiância (0,9 mW/cm^2) do dispositivo a base de CMC/HA 5 em comparação com substratos de celulose bacteriana comercial. Entretanto, a eficiência (EQE – 2,5%) foi menor devido a alta desidade de corrente. Os resultados mostram que o novo biopolímero é comparável com o substrato comercial de celulose bacteriana. Testes de dobramento em função da corrente medida também foram realizados, mostrando uma perda na condução de corrente conforme há o dobramento do dispositivo depois de 10 ciclos de dobramento.

LIST OF SYMBOLS AND ABBREVIATIONS

PL – Photoluminescence

E_{low} – Low Energy State

E_{exc} – Excited Energy State

S_1 – Singlet Excited State

S_0 - Singlet Ground State

T_1 - Triplet Excited State

τ – Lifetime

N_0 – Concentration od Excitate Species in t = 0

t – Time

k_r – Radiative Constant Rate

k_{nr} - Nonradiative Constant Rate

ϕ – Quantum efficiency

Φ – Quantum Yield

FRET – Förster Ressonance Energy Transfer

$W_{d\text{-}d}$ – Dipole-Dipole Energy Transfer Rate

R_0 – Förster Distance

n – Refractive Index

Na – Avogadro Number

$F_\lambda(\lambda)$ – Donor's emission Area

$\varepsilon(\lambda)$ – Acceptor's extinction coefficient

S_D – Dipole Strenght of the Donor

S_A – Dipole Strenght of the Acceptor

ħ – Reduced Planck Constant

G_D – Donor degeneracies

G_A – Acceptor degeneracies

F – Energy Mismatch Factor

γ_D – Bandwidth of Half-Height of the Donor

γ_A - Bandwidth of Half-Height of the Acceptor

Δ – Energy Difference

h – Planck's Constant

σ – Barycentre of the emission band

F_0 – Emission Band Area in the Absence of Quencher

F – Emission Band Area in the Presence of Quencher

K_{sv} – Stern-Volmer Quenching Constant

[Q] – Quencher's Concentration

K_D – Collisional Quenching Constant

k_q - Collisional Quenching Constant

τ_q – Lifetime in the Presence of Quencher

τ_0 – Lifetime in the Absence of Quencher

K_s – Constant Binding Complex

[E-Q] – Non-Emissive Complex Concentration

[E] - Emitter Concentration

f_a – Fractional of the Total PL Emission Available

K_a – Stern-Volmer Quenching Constant of the Accessible Fraction

PCS – PL Chemical Sensors

LOD – Limit of Detection

LOQ – Limit of Quantification

AAS – Atomic Absorption Spectroscopy

ICP-MS – Inductively Coupled Mass Spectroscopy

XRF – X-Ray Fluorescence Spectrosopy

CDs – Carbon dots

GQD – Graphene Quantum Dots

CQD – Carbon Quantum Dots

CND – Carbon Nanodots

CPD – Carbon Polymer Dots

QC – Quantum Confinement

SS – Surface States

ACQ – Aggregation Caused Quenching

PVA – Polyvinyl Alcohol

PDMMA – N-N’ dimethyl acrylamide

PEI – Poly(ethylenimine)

HSAB – Hard Soft Acid Bases

PET – Photoinduced Electron Transfer/ Polyethylene Terephtalate

LUMO – Lowest Unoccupied Molecular Orbital

HOMO – Highest Occupied Molecular Orbital

FE – Face-Edge

FF- Face-Face

EE – Edge-Edge

w/w – Weight/Weight

Acf – Acriflavine

Rhb – Rhodamine B

TTA – 2-Thenoytrifluoroacetone

XRD – X-Ray Diffraction

XPS – X-Ray Photoelectron Spectroscopy

TEM - Transmission Electron Microscopy

WLED – White Light Emitting Diodes

P-TPE – Substitute Tetraphenylethene

OLED – Organic Light Emitting Diodes

LED - Light Emitting Diodes

EML – Emissive Layer

ITO – Tin-doped Indium Oide

EIL – Electron Injection Layer

HIL - Hole Injection Layer

ETL - Electron Transport Layer

HTL – Hole Transport Layer

EQE – External Quantum Efficiency

w/v – Weight/Volume

PXRD – Powder X-Ray Diffraction

FTIR – Föurier Transformed Infrared

FEG-SEM – Field Emission Gun-Scanning Electron Microscopy

STEM – Scanning Transmission Electron Microscopy

EDX – Energy Disperse X-Ray

UV – Ultraviolet

Vis – Visible

CHN – Carbon Hydrogen Nitrogen Elemental Analysis

TGA – Thermogravimetric Analysis

DTG – Derivative Thermogracimetric

UHV – Ultra High Vacuum Chamber

d – Interlayer Spacing

ν – Stretching Vibration

δ – Angular Deformation

IPCA – 5- Oxo – 1,2,3,5 – Tetrahydroimidazo [1,2-a] pyridine – 7 carboxylic

IRF – Instrumental Response Function

I – Intensity

AIE – Aggregation Induced Emission

CSS – Coupled Surface States

IS – Intrinsic States

W_{ex} – Exchange Energy Transfer Rate

λ_{exc} – Excitation Wavelength

$[Hg^{2+}]$ – Hg^{2+} Concentration

CMC – Carboxymethyl Cellulose

HA – Hyauluronic Acid

OFET – Organic Field Effect Transistor

OTFT - Organic Thin Films Transistor

BC – Bacterial Cellulose

β-NPB – N,N'-Bis(naphthalen-2-yl)-N,N'-bis(phenyl)-benzidine

TCTA – 4,4',4-Tris(carbozol-9-yl)triphenylamine

TPBi – 1,3,5-Tris(1-phenyl-1Hbenzimidazol-2-yl)benzene

$Ir(ppy)_3$ – Tris(2-phenylpyridine)iridium(III)

Bphen - 4,7-Diphenyl-1,10-phenanthroline

CP-MAS-NMR – Solid State Cross Polarization Magic Angle Spinning Nuclear Magnetic Resonance

ATR – FTIR – Attenuated Total Reflectance Föurier Transformed Infrared

UTS – Ultimate Tensil Strength

EAB – Elongation at the Break

YM – Young's Modulus

AFM – Atomic Force Microscopy

LIST OF FIGURES

Figure 2.S13. Room and low temperature decay curves of CDLP-D monitored at 450 nm and excited at 375 nm using a nano-LED. IRF is the instrumental response function. The model used was $y = y0 + nAn\exp(-(tn - x0)/\tau n)$, where y is the PL intensity, y_0 is a constant, A_n the amplitude of the n component of the decay, t_n is the experimental decay data, and x_0 = 6.96 ns is obtained by the instrument response function. The best fitting was achieved by applying one component. Lifetime obtained at 298 K was $\tau 450298$ = 7.0 $\pm$ 0.1 ns and at 13 K was $\tau 45013$ = 10.0 $\pm$ 0.1 ns. 127

LIST OF TABLE

TABLE OF CONTENTS

CHAPTER 1

Introduction/ literature review and objectives

1. INTRODUCTION/LITERATURE REVIEW

1.1. LAPONITE® FEATURES AND PHOTONIC APPLICATIONS

Clay minerals have proven efficient in the adsorption of metals at low concentrations. In addition to their large surface area, they are low-cost, non-toxic to the environment, and have a high ion exchange capacity (UDDIN, 2017). These physicochemical characteristics make clay minerals promising materials for the construction of sensors for heavy metals, primarily due to their high ion exchange capacity, which possibly contributes to greater reversibility at binding sites, ensuring more versatility in metal detection. Unlike traditional sensors, which, despite the selectivity provided by immobilizing molecules to metals, face difficulties in reversing the reaction, affecting reproducibility.

LAPONITE® is a synthetic clay mineral with the empirical formula $Na_{0.7}^{+}[(Si_8Mg_{5.5}Li_{0.3})O_{20}(OH)_4]_{0.7}^{-}$ belonging to the smectite family, a group of layered silicates consisting of alternating layers in the TOT form, where the O layer represents Al-O and/or Mg-O groups arranged octahedrally and positioned between two T layers containing Si-O groups in tetrahedral form, as shown in Figure 1.4 also known as a 2:1 structure (BECHER et al., 2019; ZHAO et al., 2015). The octahedral center is coordinated by oxygen and hydroxyl anions, and the tetrahedral center is preferably by oxygen; both can undergo isomorphic substitution by species of lower charge (in LAPONITE®, Mg^{2+} by Li^{+}), leading to negative charges on the surface between the layers, counterbalanced by cations such as Na^{+}, K^{+} and Ca^{2+}(in LAPONITE®, Na^{+}) (PEROTTI et al., 2011; ZHAO et al., 2015).

The layers of LAPONITE®, have the shape of nanodiscs with a diameter of 25 nm and a thickness of 1 nm. When dispersed in water, they exfoliate, as illustrated in Figure 1.4 interacting through electrostatic attraction between face and edge (FE), repulsion between face-face (FF) and edge-edge (EE), as well as Van der Waals interactions (BECHER et al., 2019; HUANG; ZHI, 2016). This occurs because of the acquired permanent change on the clay mineral's surface when dispersed in the water while the edges composed of Mg-OH are pH-dependent charges, susceptible to protonation and deprotonation (SUMAN; JOSHI, 2018). Pilavtepe et al. (2018) systematized the interaction of these layers based on the relationship between the solution pH and the point of zero charge at the edges (pH_{pcz-e} ~11). When the pH is greater than pH_{pcz-e}, FF and EE

interactions dominate, with Na^+ ions present between the layers. At high pH and ionic strength, the FF orientation is preferable. Conversely, when the pH is lower than $pH_{pcz\text{-}e}$, FE interactions occur, leading to the formation of a “house of cards” structure, as illustrated in Figure 1.4(b). This attraction force reflects the high viscosity of LAPONITE® suspensions and the gel-like behavior (BECHER et al., 2019). According to Ruzicka and Zaccarelli (RUZICKA; ZACCARELLI, 2011) and Bonn et al. (BONN et al., 1999) gel-state are disordered solid states with no long-range order and with low density. Attractive forces hold the particle network together. While glassy-state the particles remain with long-range repulsive forces, with no network formed. At high clay concentrations and low ionic strengths, the state adopted by LAPONITE® is glassy, also called Wigner glasses (BECHER et al., 2019; RUZICKA; ZACCARELLI, 2011; SUMAN; JOSHI, 2018).

The chemical stability of LAPONITE® depends on pH and Na^+ concentration. The dissolution of the clay mineral can occur according to the reaction R1, which is observed by the Mg^{2+} release. The work by Thomson and Butterworth (1992) using 10.0 $g{\cdot}L^{-1}$ of LAPONITE® revealed no release of Mg^{2+} and silicates at pH 10. Conversely, Jatav and Joshi (2014) verified low Mg^{2+} release at pH>10, using 1% (w/w) LAPONITE®. According to them Na^+ with 7.2 mM of NaCl added plays an important role in preventing LAPONITE® dissolution. Pilavtepe et al. (2018) described that the minimal pH to set is 8.5 since values below the LAPONITE ® start to dissolve.

$$\begin{aligned} &Na_{0.7}Si_8Mg_{5.5}Li_{0.3}O_{20}(OH)_{4(s)} + 12\ H^+_{(aq)} + 8\ H_2O_{(l)} \rightarrow \\ &0.7\ Na^+_{(aq)} + 8\ Si(OH)_{4(s)} + 5.5\ Mg^{2+}_{(aq)} + 0.3\ Li^+_{(aq)} \end{aligned} \qquad \text{(R1)}$$

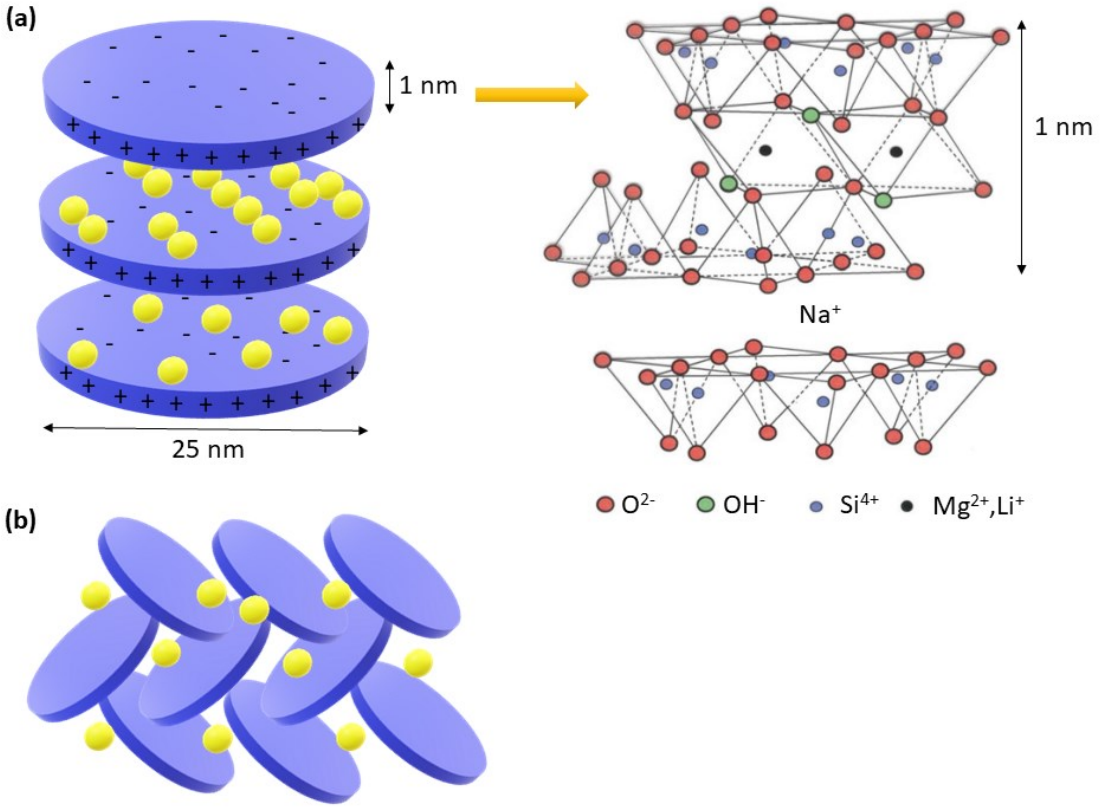

Figure 1.1. Representation of the structure of LAPONITE® with a basal spacing of approximately 1 nm and a diameter of 25 nm; yellow spheres represent Na+ ions (a). Representation of LAPONITE® structure when dispersed in water if pH < pHpcz-e (b). Adapted from Huang and Zhi (2016)

1.1.1. LAPONITE® in photonic applications

LAPONITE® is widely explored in the biomedical field due to its drug-loading capacity and potential for a slow-release effect (DAS et al., 2019; MARIA J. RODRIGO; MARIA J. CARDIEL; JOSE M. FRAILE; JOSE A. MAYORAL; LUIS E. PABLO; ELENA GRACIA-MARTINS, 2024). However, its transparency and the ability to functionalize it with fluorophores and nanoparticles also make it a promising candidate for photonic applications. For example, Dey et al. (2013) demonstrated its use in pH recognition via PCS. The authors investigated the effect of the clay mineral in the FRET between the two dyes acriflavine (Acf) and Rhodamine B (RhB) in different pH, either in solutions and in the layer-by-layer films on glass slides. In either case, in comparison with the mixture Acf-RhB without the clay, there was a significant enhancement of RhB (aceptor) fluorescence. The calculations also showed an increase in the energy transfer efficiency, R_0 and r, indicating that the clay allowed closer interactions of the adsorbed molecules, achieving an energy transfer efficiency of 92.50% when the acceptor concentration was 90%. The pH could also be monitored by the spectral overlap, showing

a linear relationship with increasing pH. At higher pH levels, RhB can deprotonate and interact more closely with Acf, increasing the spectral overlap with high pH. LAPONITE® also increases the thermal and photostability of lanthanide coordination compounds, as demonstrated by Yang, Wang and Li. (2015). The authors cation-exchanged the Na^+ in LAPONITE® with Eu^{3+} and then added the β-diketone ligand (TTA) to the system, resulting in the formation of $Eu(tta_n)$ coordination compound within the interlayers. This was further confirmed by the enlargement of *d*-space verified by X-Ray diffraction (XRD) measurements. Compared to pure $Eu(TTA)_3.2H_2O$, the emission intensity of the composite did not decrease after 10 hours of constant UV irradiation, whereas the pure compound's intensity decreased to 70%. Additionally, when heated to 120 ºC, the composite showed only a 17% decrease in emission intensity after 10 h, while the pure compound showed a 72% decrease. Immobilization of ZnO (JOO et al., 2013) and TiO_2 (DÉCSINÉ et al., 2020) nanoparticles using LAPONITE® for photocatalysis applications also were reported. In order to understand the process involved in photonics applications, it is important to comprehend the photoluminescence principle discussed in the next topic

1.2. PHOTOLUMINESCE'S PRINCIPLE

Photoluminescence (PL) is considered a specific case of luminescence, a phenomenon characterized by the emission of photons from the excited electronic states of a substance. Excitation and emission are the two main processes that occur in PL. Excitation consists of the absorption of energy by an electronic state, which causes an electron promotion to higher excited states. When electrons in an excited energy state (with energy E_{exc}) decay to a lower energy state (E_{low}), a "release" of photons with specific energy $E_{photon} = E_{exc} - E_{low}$ may occur and, this process is called emission. If it occurs between states of the same spin multiplicity, it is denominated as fluorescence. For example, when the electron in singlet excited state S_1 (with a lifetime between 10^{-10} to 10^{-7} s) returns to the singlet ground state S_0. The state is termed a singlet due to the multiplicity (2S+1) equating to one, as the total spin angular momentum is zero in paired electrons. In addition, according to the quantum mechanics selection rule for electric dipole transitions, either the spin and orbital angular momentum are conserved, thus, singlet-singlet transitions are allowed (CHOWDHURY, 1996; ELLIS, 1999; LAKOWICZ, 2006; VALEUR, 2001).

Besides the emission process, the excited state can undergo several de-excitation pathways, also denominated as nonradiative transitions. This can be visualized in the

Perrin-Jablonski diagram, represented in Figure 1.1. Most of these processes are related to the structure and medium of the substance, in which the vibrational and rotational motions introduce energy levels within the excited and ground states, leading to these non-radiative pathways. When the vibrational levels of the electronic states have similar energies and the same multiplicity, internal conversion can occur, followed by non-radiative relaxation to reach the lowest vibrational level of the endmost electronic state. Intersystem crossing is a non-radiative transition between electronic states with different multiplicities that have vibrational levels of similar energy. This can be accompanied by non-radiative relaxation, or reverse intersystem crossing due to energy gain in the form of heat and return to the initial state, leading to "delayed fluorescence". Phosphorescence, on the other hand, is the radiative process that occurs between states of different multiplicity (with an excited state lifetime between 10^{-6} to 10^{1} s), such as between triplet T_1 (excited state) and singlet S_0 (ground state). In contrast to fluorescence, this process is forbidden because the angular momentum changes in the decay process in order to pair with the ground state spin. Energy transfer also can occur and will be discussed in the next topic (LAKOWICZ, 2006; VALEUR, 2001).

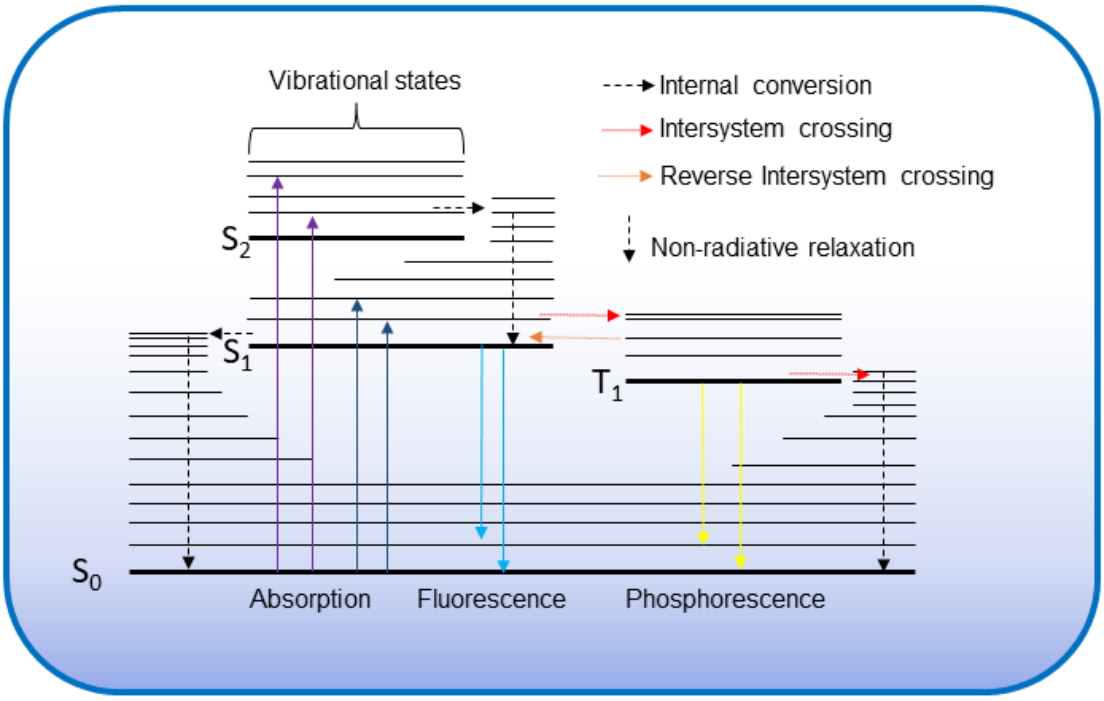

Figure 1.2. Perrin-Jablonski diagram adapted from Valeur, 2001

The excited species has a “time to stay” in the excited states, described as the lifetime. The lifetime (τ) of an excited state is defined as the time that an initial population N_0 reaches the value of 1/e, experimentally estimated by measuring the emission decay of the excited state to the ground state following equation (1). N(t) is the concentration of excited species at time t and N_0 is the concentration of excited species at t = 0. These are proportional to the emission intensity I(t) measured by the spectrofluorometer, defined as the amount of photons emitted per unit time (s). The relation between the decay rates (based on first-order kinetics behavior) considers the rate constants for radiative (k_r) and non-radiative (k_{nr}) processes as described by equation (2) (HORIBA, [s.d.]; LAKOWICZ, 2006; VALEUR, 2001)

$$N(t) = N_0 \exp\left(-\frac{t}{\tau}\right) \tag{1}$$

$$\tau = \frac{1}{k_{nr}+k_r} \tag{2}$$

Due to the various non-radiative pathways following the excitation process, the absorbed energy is not entirely emitted. The quantum efficiency ϕ, described by equation (3) is a useful parameter for assessing whether radiative processes prevail over non-radiative ones or not. It is represented as the ratio between k_r and the sum of k_r and k_{nr}. Quantum yield Φ is the number of emitted photons over the number of absorbed photons. It can be measured by an integrated sphere coupled to a spectrofluorometer, according to equation (4) (FERY-FORGUES; LAVABRE, 1999; FRAIJI; HAYES; WERNER, 1992).

$$\phi = \frac{k_r}{k_{nr}+k_r} \tag{3}$$

$$\Phi = \frac{\text{number of emitted photons}}{\text{number of absorbed photons}} \tag{4}$$

1.2.2. Energy transfer

The process described above outlines the basic pathways and parameters of PL for a single system (e.g. a specific molecule). However, in complex systems involving more than one substance, possible interactions can introduce new pathways in the PL process, such as nonradiative energy transfer. When two substances interact and their vibrational

states have approximately the same energy, resonance between these transitions can lead to nonradiative energy transfer. This energy is transferred by the molecule known as the donor, and subsequently absorbed by another molecule, called the acceptor. This process requires spectral overlap between the donor's emission spectrum and the acceptor's absorption spectrum. As a result, the emission intensity of the donor decreases in the spectral overlap range, while the emission of the acceptor tends to increase (VALEUR, 2001).

These interactions can be between electric dipole (or multipole) transitions of the donor and acceptor, leading to dipole (or multipolar) mechanisms. This occurs predominantly for electric dipole-allowed transitions, with long-range interaction if it is dipole-dipole (Förster) and short-range if multipolar. The mechanism, called Föster resonance energy transfer (FRET), is described as a simultaneous process of energy transfer between the excited donor's electron that is returning to the ground state, and the acceptor's electron that is being promoted to the excited state. On the other hand, if the interaction is due to intermolecular orbital overlap, electron exchange mechanism (Dexter mechanisms) may occurs. In this case, is predominant for forbidden transition with short-range interactions. The mechanism is described as an energy transfer associated with an exchange between donor-acceptor electrons. For example, an electron from the donor's excited state to the acceptor's excited state, simultaneously from the acceptor's ground state to the donor's ground state (N CARNEIRO NETO et al., 2022; VALEUR, 2001).

Initially, by quantum-mechanics and classical considerations regarding the dipole-dipole interactions, Förster could establish the equations (5) and (6) that calculate the energy transfer rate ($W_{d\text{-}d}$, in s^{-1}), based on spectroscopic measurements. Whereas τ_0 is the donor's lifetime without the acceptor's presence, r the distance between donor-acceptor and R_0 the Förster distance calculated by equation (5). Whereas k^2 is the orientation factor between donor-acceptor transition moments, Φ_D^0 the quantum yield of the donor without the acceptor's presence, n the refractive index of the medium and N_a the Avogadro number. The integral part represents the degree of spectral overlap between the donor emission spectrum and acceptor absorbance spectrum, with $F_\lambda(\lambda)$ representing the donor's emission area and $\varepsilon(\lambda)$ the acceptor's extinction coefficients .(LAKOWICZ, 2006; VALEUR, 2001). According to Valeur (2001) R_0 is " the distance at which the probability of donor decay by energy transfer to an acceptor is equal to the probability of decay by all intrinsic processes, be they radiative or nonradiative". By this definition, it

is clear that energy transfer leads to non-radiative pathways which directly impact the emission decay of the donor-acceptor pair. Thus, spectroscopic measurements using emission decay and PL emission can underlie even the distance between the donor-acceptor molecules.

$$W_{d\text{-}d} = \frac{1}{\tau_0}\left(\frac{R_0}{r}\right)^6 \tag{5}$$

$$R_0^6 = \frac{9(\ln 10)k^2\Phi_D^0}{128\pi^5 N_a n^4}\int_0^\infty F_\lambda(\lambda)\varepsilon(\lambda)\lambda^4 d\lambda \tag{6}$$

This equation works well for donor-acceptor with fixed distance as labeled proteins (LAKOWICZ, 2006). For organic-inorganic systems, the $W_{d\text{-}d}$ can be calculated by Förster-Dexter expression (7) (NOBRE et al., 2007). Where S_D and S_A are the dipole strength of the donor and acceptor transition respectively, ħ is the reduced Planck's constant and G_D and G_A are the donor and acceptor degeneracies (if singlet, $G_D = G_A = 1$). F is the energy mismatch factor that considers the vibrational state overlaps and temperature effects, described by (8) (CARNEIRO NETO et al., 2019; MALTA, 2008). γ_D and γ_A are the bandwidths at half-height (in cm^{-1}) of the donor and acceptor respectively. Δ is the energy difference between donor-acceptor states, c is the speed of light, and h the Planck's constant. The dipole strength also can be calculated by (10), whereas the σ is the barycentre of the emission band and τ the lifetime of the donor or acceptor.

$$W_{d\text{-}d} = \frac{2\pi}{\hbar}\frac{S_D S_A}{G_D G_A r^6} F \tag{7}$$

$$F = \frac{Y}{(\gamma_D^2+\gamma_A^2)^{\frac{1}{2}}} \times e^{-\left(\frac{\Delta}{\gamma_D}\right)^2 \Gamma} \tag{8}$$

$$\Gamma = \left[1 - \frac{1}{1+(\gamma_D+\gamma_A)^2}\right]\ln 2, \quad Y = \left(\frac{\ln 2}{\pi}\right)^{\frac{1}{2}}\left(\frac{1}{ch}\right) \tag{9}$$

$$S = \frac{3\hbar}{32\pi^3\sigma^3\tau} \quad (10)$$

1.2.3. Quenching mechanisms

It is worth highlighting the influence of external factors on the quantum yield of emission. Besides intermolecular and intramolecular interactions, which are responsible for non-radiative contributions, the system is also mainly exposed to the effects of specific substances, temperature, pH, and solvent polarity (LAKOWICZ, 2006; VALEUR, 2001). The effect of temperature is typically associated with the thermal agitation of molecules at high temperatures, leading to increased collisions, rotations, and intramolecular vibrations. These effects, can promote non-radiative processes and reduce the quantum yield. pH can influence the formation of non-radiative species or shift the emission to other wavelengths. Similar to pH, solvent polarity can shift the emission to longer wavelengths, reducing the energy of the excited state as the solvent becomes more polar. A substance can interact with the emitter and deactivate the excitation state or form a non-emissive species. These perturbation phenomena cause a decrease in emission intensity recorded by the spectrofluorometer, and it is known as PL quenching (LAKOWICZ, 2006; VALEUR, 2001).

A useful model to evaluate how much a species may be acting as a quencher is the Stern-Volmer equation, shown in equation (11). where: F_0 and F are the emission area in the absence and presence of the quencher, respectively; K_{sv} is the Stern-Volmer quenching constant and [Q] is the quencher's concentration. The most common form of PL emission quenching occurs due to collisions between diffused molecules in the solution, called collisional quenching. As mentioned before, this promotes vibrational energy transfer, increasing the probability of internal conversion and deactivating the excited state. If it is established that the quenching is collisional, $K_{sv} = K_D = k_q\tau_0$. Whereas k_q is the bimolecular quenching constant and τ_0 is the lifetime in the absence of the quencher. In addition $\frac{F_0}{F} = \frac{\tau_0}{\tau_q}$, which τ is the lifetime in the presence of the quencher (LAKOWICZ, 2006; VALEUR, 2001; ZU et al., 2017).

The quencher can also interact with the emitter to form a non-emissive complex, which upon excitation, returns to the ground state without emitting photons—a process

known as static quenching. The same equation can be used for static quenching, however, in this case, $K_{sv} = K_s = \frac{[E\text{-}Q]}{[E][Q]}$. Whereas the K_s is the constant for complex binding constant [E-Q] the non-emissive complex concentration and [E] the emitter concentration. In contrast with collisional quenching, the emission decay is unaffected and $\frac{\tau_0}{\tau_q} = 1$. Furthermore, changes in the absorption spectra may occur (LAKOWICZ, 2006; VALEUR, 2001; ZU et al., 2017).

$$\frac{F_0}{F} = 1 + K_{sv}[Q] \tag{11}$$

In most systems, both mechanisms can be present, typically indicated by a deviation from linearity in the plot. A good parameter to evaluate the mechanism tendency is their temperature dependence. Higher temperature promotes faster diffusion resulting in enhanced values of K_{sv}. Conversely, the same effect causes the dissociation of the quencher-emitter bond, decreasing K_{sv} values (LAKOWICZ, 2006; ZU et al., 2017). Deviations from linearity also can be associated with higher quencher concentrations or the presence of more than one emitter present (LAKOWICZ, 2006).

Fractional accessibility to quencher is a modified Stern-Volmer model to evaluate the last case mentioned, described by equation (12). Whereas f_a is the fraction of the total PL emission available to quencher and K_a the Stern-Volmer quenching constant of the accessible fraction. This model considers that at least one emitter is not accessible to the quencher.

$$\frac{F_0}{F_0 - F} = \frac{1}{f_a K_a[Q]} + \frac{1}{f_a} \tag{12}$$

1.3. PHOTOLUMINESCENCE CHEMICAL SENSOR FOR HEAVY METALS

1.3.1. Photoluminescence chemical sensor features

Although quenching effects are associated with low undesired quantum yields, it is possible to exploit the phenomenon for the benefit of an application, such as PL chemical sensors (PCS). Optical chemical sensors utilize the interaction of electromagnetic radiation with the analyte to generate an analytical signal based on a specific optical parameter, such as absorption, PL emission, lifetime, and anisotropy, which can be

correlated with concentration (LI et al., 2013; ULLAH et al., 2018). Although selectivity depends on specific chemical interactions between the sensor and the analyte, PCS exhibit high sensitivity and low limit of detection (LOD), along with enhanced functional versatility (RASHEED et al., 2018). For example, the ability to manufacture sensors in the form of optical fibers allows for the propagation of signals over long distances for *in situ* and online measurements, aiming to reduce exposure to contaminated samples and data acquisition time (JOE et al., 2018).

The PL emission intensity is the most commonly monitored measure, and quenching acts by decreasing the emission intensity. When an analyte exerts quenching, it is possible to establish a relationship between the concentration of the quencher and the emission intensity by developing an analytical curve, thus detecting and quantifying the concentration of the quencher analyte . The process describes the basic principle of a turn-off PSC. Other measures can also be monitored, such as the wavelength shift of emission, lifetime, anisotropy, and absorption (VALEUR, 2001). The interaction of an analyte with the sensor can also increase the emission intensity, in this case, called turn-on PSC.

PSC for the detection of heavy metals typically contains functional groups responsible for complexing with the metal and quenching PL emission. The stability of the complex depends primarily on various factors, such as the nature of the cation, solvent, temperature, ionic strength, and pH. In metal detection, the sensor's selectivity to a specific cation arises from the sensor's structural characteristics, such as the nature and quantity of functional groups, and configurational factors. Additionally, these must align with the characteristics of the cation: ionic radius, charge density, coordination number, and intrinsic nature (hardness and softness). The medium will mainly influence the difference between the complex's coordination energy and solvation energy, as well as the interaction difference between the ligand sphere and the dielectric medium outside the first solvation sphere. Therefore, monitoring pH and ionic strength is important in the process of sensing heavy metals (LI et al., 2013; ULLAH et al., 2018; VALEUR, 2001).

1.3.2. Heavy metals and detection methods

Environmental monitoring has become increasingly necessary due to anthropogenic actions in recent years. One of the main problems related to environmental contamination is chemical pollution in aquatic environments by inorganic species mainly from industrial and agricultural effluents. Metallic ions such as Cd^{2+}, Cr^{6+}, Co^{2+}, Cu^{2+}, Pb^{2+}, Hg^{2+}, As^{3+} and Ag^{+} at minimal concentrations cause harmful effects on humans, flora, and fauna

(TCHOUNWOU et al., 2012), and several works (ASSIS et al., 2019; CARVALHO et al., 2017; DA SILVA et al., 2019; GONCALVES et al., 2014; SOUZA et al., 2016) have associated high concentrations of these contaminants with industrial and urban waste, due to both negligence in waste treatment and industrial accidents. The term 'heavy metal' is used to describe a group of metallic and semi-metallic elements with an atomic density greater than 4±1 g cm^{-3}, such as those mentioned above, assuming an association between mass and toxicity (BURAKOV et al., 2018; DUFFUS, 2002). Although the term is not recommended by the IUPAC (DUFFUS, 2002), various regulatory agencies and the scientific community continue to use it.

The toxicity of metals is primarily associated with their ability to bind to physiological sites intended for essential metals (KLAASSEN; EATON, 1991). An example is itai-itai disease, where Ca^{2+} is replaced by Cd^{2+} in osteogenic cells, causing bone fragility (KAZANTZIS, 2004). Contaminant metals are transported within the body via mimicry, forming stable and insoluble compounds, such as the substitution of phosphates with arsenates (KLAASSEN; EATON, 1991). Many metal ions can also interact with DNA, causing structural damage and conformational changes that lead to carcinogenic effects. For instance, Cr^{6+} is reduced to Cr^{3+} by intracellular reducing agents once it enters cellular organelles, contributing to the formation of DNA adducts (BEYERSMANN; HARTWIG, 2008; SHI et al., 2001). Similarly to Cd^{2+}, Cr^{6+} can inhibit or mimic the actions of Ca^{2+}, induce genetic mutations, and cause cellular damage and death. Experiments in rats indicate a potential carcinogenic activity in humans (TCHOUNWOU et al., 2012).

Another highly toxic metal ion is Hg^{2+}, which has a high affinity for thiol groups, forming covalent bonds with cysteine residues in proteins and producing reactive oxygen species. This reduces antioxidant concentrations and leads to the accumulation of free radicals, causing cellular DNA damage and potentially initiating carcinogenic processes (TCHOUNWOU et al., 2012; VALKO; MORRIS; CRONIN, 2005). Ions Hg^{2+} can be released in the aquatic environment from: detonators in explosives, such as mercury (II) fulminate [$Hg(CNO)_2$]; fireworks and as intensifiers in photography, such as mercury (II) thiocyanate [$Hg(SCN)_2$]; waste from the refining or smelting of ores, such as mercury (II) selenide HgSe; gold and silver extraction, such as mercury (II) sulfate $HgSO_4$ and as biocides such as phenyl mercury (II) acetate $Hg(C_6H_5)(C_2H_3O_2)$ (EPA, 2009; SOUZA, JULIANA; BATISTA; BERNSTEIN, 2014). In this environment, conditions such as low pH, high dissolved organic matter concentration, and low particulate matter content can contribute to the conversion of mercury (II) to methylmercury (CH_3Hg^+ , the most toxic

form of mercury) by microorganisms (SOUZA; BARBOSA, 2000). For example, the methylation by *Desulfovibrio desulfuricans* bacteria, which can be found in aquatic sediments and anaerobic bottom Waters (GILMOUR et al., 2011). Methylmercury is extremely toxic because it is highly absorbed by the organism and transported through the bloodstream to the central nervous system, causing severe disorders. Methylmercury poisoning leads to symptoms such as paralysis and mental retardation, a condition also known as Minamata disease, named after the Minamata incident in Japan. In this incident, methylmercury was discharged into the effluent by the Chisso Corporation as a byproduct of acetic acid production, resulting in the poisoning of the local population due to the consumption of contaminated fish and seafood (HONG; KIM; LEE, 2012; SOUZA, JULIANA; BATISTA; BERNSTEIN, 2014). According to resolution 430/2011 of CONAMA, in Brazil the maximum amount allowed of total dissolved mercury is 0.01 mg mL^{-1} in hydric effluents (CONAMA, 2011).

Humans can be exposed to these metals through inhalation, ingestion, or dermal contact. Metals can spread in the environment through anthropogenic activities or naturally (such as volcanic eruptions, erosion, and biogenic sources), affecting soil, water, and air (MASINDI; MUEDI, 2018). Soil is highly vulnerable, accumulating residues from water sources and anthropogenic activities, particularly conventional agriculture with excessive use of contaminated fertilizers and irrigation water. The non-biodegradable nature of heavy metals leads to their accumulation, reducing soil quality. They can also be absorbed by plants, entering the human food chain. Water is the main compartment for metal dissemination, where metals are transported due to industrial waste. Even at trace levels, metals in water exhibit high toxicity, affecting humans and all organisms, especially aquatic life. In the air, heavy metals are associated with particulate matter, causing health issues such as skin and eye irritation, respiratory infections, and cardiovascular diseases. They also induce acid rain formation and corrosion, deteriorating infrastructure (MASINDI; MUEDI, 2018; MISHRA et al., 2019).

The detection process must consider not only cost and analysis time but also environmentally friendly methods and good sensitivity at trace levels. Analytical methods for determining metal concentrations in water samples typically use atomic absorption spectroscopy (AAS), inductively coupled plasma mass spectrometry (ICP-MS), X-ray fluorescence spectroscopy (XRF), and voltammetry (APHA, 2017; NIESSNER, 2000).

Common disadvantages of conventional metal detection techniques include high costs, extensive analysis times, complex instrumentation, and extensive sample preparation for

field evaluations. Low-cost chemical sensors are frequently reported in the literature as effective means for detecting and determining the concentration of heavy metals. Two approaches are commonly highlighted: optical chemical sensors and electrochemical sensors. Despite differences in their detection response mechanisms, both types offer advantages such as miniaturization, portability, low cost, ease of handling, and low limits of detection (LOD), making them promising alternatives to conventional techniques.

The primary challenge in this field is enhancing the selectivity and sensitivity of sensors. This is generally achieved through structural chemical modifications with specific groups that interact with metals and induce changes in optical or electrical physicochemical properties. In the case of electrochemical sensors, since each metal has a defined redox potential, their selectivity can be considered superior to that of optical chemical sensors. However, they face sensitivity issues due to measurement fluctuations, such as overpotential, interference from other metals, and ions from the supporting electrolyte (LI et al., 2013; ULLAH et al., 2018). Among the PCS materials, carbon dots (CD) are an interesting choice due to the features demonstrated in the next topic.

1.4. CARBON DOTS: DEFINITION AND CLASSIFICATION, PROPERTIES, SYNTHESIS, SOLID-STATE EMISSION AND APPLICATION AS PHOTOLUMINESCENCE CHEMICAL SENSORS FOR HEAVY METALS

The first report on Carbon Dots (CDs) was in 2004 when Xu et al. 2004 were investigating purification methods for carbon nanotubes using electrophoresis. Their analysis revealed fluorescent impurities generated during synthesis, surprising the researchers with emissions at multiple wavelengths from these subproduct fractions. Due to their nanometric size, they termed them fluorescent carbon nanoparticles. Two years later, Sun et al. (2006) synthesized them via laser ablation and named them Carbon Dots, attributing their emission to surface states and quantum confinement—concepts still used to explain CD emission.

1.4.1. Definition and Classification

The most widely accepted definition of CDs describes them as nearly spherical carbon nanoparticles ranging from 1 to 30 nm. They are biocompatible and environmentally friendly due to their solubility in aqueous media and the absence of toxic metals in their structure. CDs are notable for their PL across a broad region of the visible spectrum.

Recently, the classification of CDs has gained prominence in the literature. This classification is based on the arrangement of the carbon core structure, which can be crystalline or amorphous, and the presence of specific surface groups (LANGER et al., 2021; XIA et al., 2019). According to Langer et al. (2021) the groups are divided into:

- Graphene Quantum Dots (GQD): Single or few layers of graphene, typically derived from graphene or graphite materials, with well-defined shapes primarily composed of sp^2 carbon, and functional groups at the edges;
- Carbon Nanodots (CND) and Carbon Quantum Dots (CQD): Both are nearly spherical with diameters below 10 nm. CQDs have a crystalline graphite structure with surfaces functionalized typically with oxygen and nitrogen, whereas CNDs have an amorphous structure with a high degree of carbonization and similarly functionalized surfaces.
- Carbon Polymer Dots or Carbonized Polymer Dots (CPD): These form when non-carbonized luminescent residues from synthesis attach to the amorphous carbon core surface.

1.4.2. Photoluminescent Properties

The most notable feature of CDs is their PL across a wide range of the visible spectrum. Typically, an excited luminophore at a high electronic level dissipates excess energy through internal conversion, emitting only from the lowest vibrational level of S_1, according to Kasha's rule (LAKOWICZ, 2006). This characterizes emission as excitation-independent. However, unlike general luminophores, CDs can exhibit excitation-dependent PL emission, allowing a nanoparticle suspension to emit at different wavelengths under several excitation energies (JELINEK, 2017). The PL emission mechanism remains a topic of discussion, with various factors contributing to this behavior. The two most accepted theories are quantum confinement (QC), which relates the size of the nanoparticle to the emitted wavelength due to more discrete energy levels, and different surface states (SS) produced by functional groups.

1.4.2.1. Quantum Confinement

The QC theory, developed in 1984 to explain the blue shift in semiconductor nanoparticles known as quantum dots, is derived from band theory. This model describes

energy levels in semiconductor solids and evaluates photo and electroluminescence. Felix Bloch, who developed the model, studied electron movement in solids and found that the electronic wave function was delocalized across space, meaning the electron experienced no confinement. Therefore, the system couldn't be described as individual energy states but as a continuous density of states across the crystal lattice, depending on its periodicity (BIMBERG; GRUNDMANN; LEDENTSOV, 1999; BIMBERG; POHL, 2011). In semiconductors, the lowest energy state density forms the valence band, and the highest forms the conduction band, with the energy difference resulting in the band-gap (BERA; QIAN; HOLLOWAY, 2008; BIMBERG; POHL, 2011; RONDA, 2008). The promotion of an electron from the valence band to the conduction band creates a hole in the valence band, seen as a particle with +1 charge and effective mass. The electron in the conduction band and the hole in the valence band interact via Coulomb attraction, forming a quasi-particle called an exciton, with the electron-hole distance estimated by the Bohr exciton radius. When the particle size decreases, quantum barriers limit electron movement in the lattice, confining the electron and resulting in a discrete atomic-like energy state. In a nanoparticle, the number of atoms is greatly reduced compared to a solid, down to just hundreds of atoms. A minimal size difference can remove atoms from the nanoparticle. Thus, when reduced to a size comparable to the Bohr exciton radius, energy states become more discrete, with a larger band-gap and consequent blue emission shift (BERA; QIAN; HOLLOWAY, 2008; MURPHY, 2002).

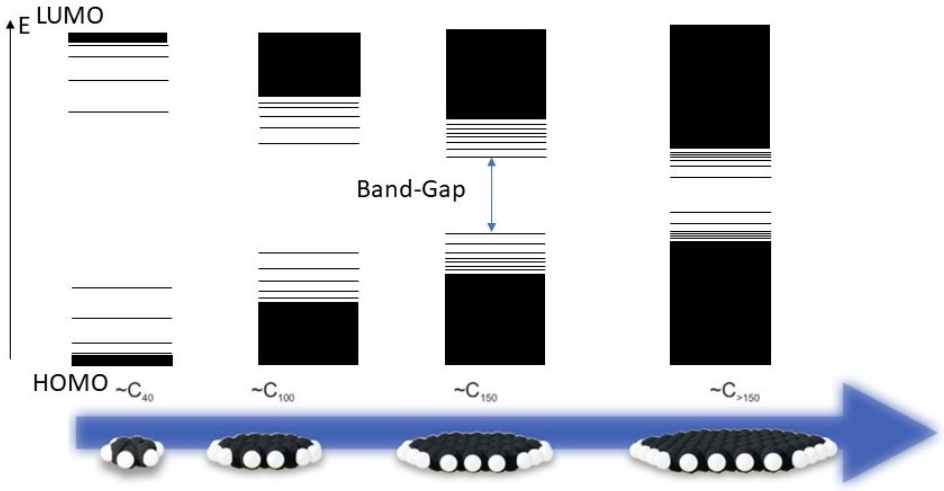

Figure 1.3. The representation of quantum confinement in CD illustrates that the more carbons in the core, the larger the nanoparticle and the lesser the effect of quantum confinement, shifting the emission towards the red. The highlighted bars represent density of states, while the dashed lines depict discrete energy states. Adapted from Langer et al. (2021)

In CDs, the carbon core size influences the nanoparticle size. CDs with more aromatic rings in the core form larger nanoparticles with red emissions, and fewer rings result in smaller nanoparticles with blue-shifted emissions, as shown in Figure 1.2. The intrinsic emission comes from the π→π* transition of sp^2 carbons (KOZÁK et al., 2016; LANGER et al., 2021; LIU et al., 2019b; MINTZ; ZHOU; LEBLANC, 2019; ZHU et al., 2015).

1.4.2.2. Surface states

SS are similar to trap levels introduced within the band-gap due to the disruption of periodicity in the crystalline lattice. Essentially, when a valence electron on the surface fails to find an orbital for covalent bonding due to lattice discontinuity, dangling bonds are formed, resulting in SS generated within the band-gap (GUERRA et al., 2018). As they possess energy lower than the conduction band and higher than the valence band, there's a preference for the SS in the promotion or return to the electron's ground state. This phenomenon is common in semiconductors and typically hinders electron-hole recombination.

In nanoscale materials, the number of atoms on the surface per volume is much higher compared to larger particles, hence SS are much more relevant due to the majority of atoms residing on the material's surface. In CDs, the surface is composed of multiple functional groups (Figure 1.3(a)) mainly hydroxyl, carbonyl, and carboxylic groups originating from most carbon precursors or generated during synthesis. The sp^2 domains in the core structure lead to the π→π* transition with higher energy emission, subject to quantum confinement. However, the functional groups present introduce SS within the π→π* transition, as illustrated in Figure 1.3(b), responsible for emission at different energies according to the electronic transition of the functional groups. Carbonyls and amines induce the n→π* transition, leading to a shift towards the red, and in some cases even a n→σ* transition, albeit more prone to non-radiative emissions (LANGER et al., 2021; WANG et al., 2016; ZHU et al., 2015).

As illustrated in Figure 1.3(b), it is possible to observe the energy levels within the intrinsic transition of CDs. Due to the small energy difference between these states, electrons can transition to lower levels and emit lower-energy photons. Several studies have demonstrated multiple emissions resulting from functional modifications on the surface (LI; DONG, 2018; SUN et al., 2006; TANG et al., 2019). Nitrogen doping, in particular, has been shown to achieve higher quantum yields, as it induces radiative

transitions and prevents non-radiative transitions caused by electron trapping in certain SS (DONG et al., 2013; HU; ZHU, 2015; WANG et al., 2015; XU et al., 2014; YU et al., 2018, 2012; ZHANG et al., 2016; ZHU et al., 2013a).

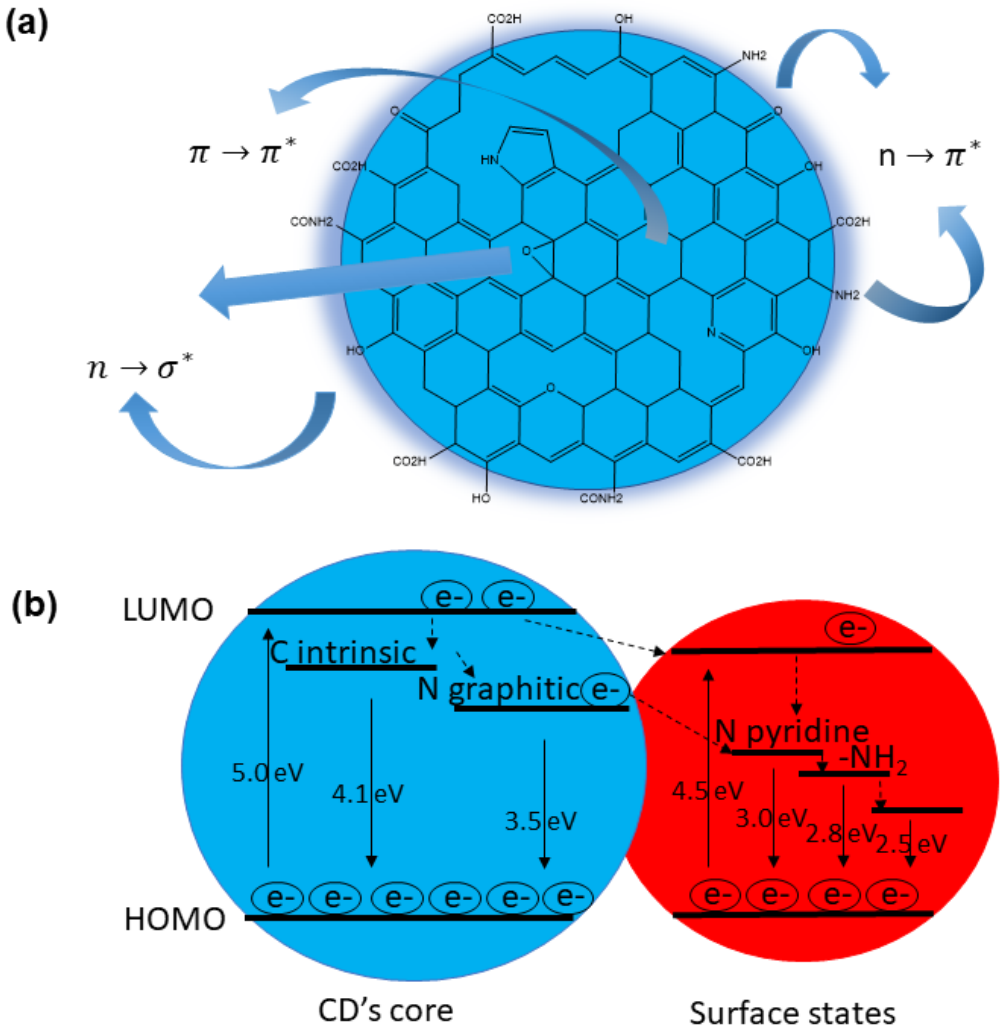

Figure 1.4. Structural representation of a CD with surface functional groups and corresponding electronic transitions (a); Surface states of different functional groups incorporated within the intrinsic emission, with estimated band-gap values, adapted from Yu et.al (2018)

1.4.2.3. Other mechanisms

Although the presented theories are widely accepted and convenient for explaining the multiple emissions of CDs, other mechanisms have been proposed in the literature. Bao et al. (2011) observed a relationship between the degree of surface oxidation and the red-shifted emission of electrochemically synthesized CNDs with homogeneous dimensions, controlled by the applied potential during synthesis. This will be discussed in the next section. According to the authors, the higher the oxygen content on the surface, the more

defect states are introduced, causing a red-shift in emission. Ding et al. (2016) confirmed this relationship through XPS and pH studies, also controlling the nanoparticle size to assess whether quantum confinement was a contributing factor. According to them, quantum confinement did not influence the emission.

Another increasingly recognized mechanism is the emission from luminophores remaining from the synthesis process. Song et al. (2015) reported the presence of a luminophore derived from citrazinic acid (IPCA), formed during hydrothermal synthesis. Kasprzyk et al. (2022) identified the formation of luminophores from the 2-pyridone family through the reaction of citric acid (CA) and α,β-diamines, substrates used in CD synthesis. Song et al. (2015) also found that the hydrothermal synthesis temperature influenced the presence of the luminophore; mild temperatures below 250 ºC favor the stability of the luminophore, thus remaining attached to the surface of CDs. Above 250 ºC, the equilibrium is disrupted as substrates contribute to forming the graphitic carbon core. A more detailed study by Hinterberger et al. (2019) varying hydrothermal synthesis conditions (time and temperature) and purifying via chromatographic column, reinforced these findings. They also detected multiple free luminophores in solution and those attached to the nanoparticle under mild (130 ºC) and medium (150 ºC) conditions, using CA and cysteine as precursors. Additionally, they observed changes in quantum yield under different conditions, implying the influence of luminophores on emission: the highest quantum yield was 70% under medium conditions, with luminophores still attached to the surface, whereas under harsh conditions (250 ºC), only the carbon core remained, resulting in a 44% quantum yield. Studies by Dekaliuk et al. (2014) and Gude et al. (2016) support the theory that CDs are aggregates or nanoclusters of a single luminophore or several luminophores with individual emissions contributing to the multiple emissions of CDs. As can be seen, the synthesis conditions are important to establish the possible PL mechanisms. Thus, the next topic presents the possible synthesis for CDs.

1.4.3. Synthesis

CDs synthesis, the main components are the precursors, the functional groups—which may or may not already be present in the precursor—and the synthesis medium. During synthesis, the key stages are essentially fragmentation (in the case of top-down synthesis), crystalline organization, and surface functionalization. Two synthesis approaches can be adopted: the top-down approach, which involves fragmenting a bulk

carbon precursor into nanometric dimensions through brute force; and the bottom-up approach, which starts with carbon precursor molecules, such as citric acid, and forms the nanoparticle through aggregation processes (JELINEK, 2017; LIU et al., 2019b; WU; LIU; YUAN, 2017).

1.4.3.1. Top-down synthesis

In the top-down approach, the precursors are typically graphite, oxidized graphite, carbon soot, activated carbon, carbon nanotubes, carbon fibers, or other carbon sources. These materials are usually subjected to rigorous high-temperature conditions. The first synthesis for obtaining CDs used laser ablation, where the high energy of the laser beam removes particulates from the solid substrate, reducing them to nanometric sizes (JELINEK, 2017; SUN et al., 2006). The advantage of this technique is that it produces CDs with structures that are generally similar to the substrates, often resulting in GQD and CQD with periodic lamellar structures that favor quantum confinement over other mechanisms. The disadvantage is the complexity of the apparatus and the need for subsequent surface functionalization (JELINEK, 2017; LIU et al., 2019b; SUN et al., 2006; WU; LIU; YUAN, 2017).

The electrochemical process is an interesting approach due to its simple instrumentation and low cost. It typically involves carbon electrodes, or a carbon electrode with a platinum counter-electrode, and an electrolyte solution of NaOH and ethanol (JELINEK, 2017; WU; LIU; YUAN, 2017). The electric current induces the cleavage of C-C bonds and produces hydroxyl residues that create defects in the electrode substrate structure. Hydroxyl and oxygen radicals formed by the electrochemical reaction can penetrate these defects and fragment the precursor particles, resulting in crystalline nanoparticles with structures similar to the precursor. This method favors the formation of CQD and GQD, and its primary advantage is the greater homogeneity of particle sizes, as the applied potential is inversely proportional to particle size. Higher applied potential synthesize smaller CDs. The drawback is the need for subsequent functionalization (BAO et al., 2011; JELINEK, 2017; LI et al., 2010; WU; LIU; YUAN, 2017).

Chemical oxidation with strong acids under reflux is another inexpensive technique. It involves dissolving carbon aggregates in a strong acid or a mixture of strong acids under reflux, typically HNO_3 and H_2SO_4. Besides being cost-effective, this technique introduces OH and COOH groups, as well as nitrogen from the nitric acid. Due to the strong oxidative effect of the acids, surface defects are produced, which influences fluorescence

emission. The structure is generally more amorphous, forming CNDs that are susceptible to surface states. The disadvantage is the poor control over shape, homogeneity, and low quantum yield (JELINEK, 2017; RAY et al., 2009; WU; LIU; YUAN, 2017).

1.4.3.2. Bottom-up synthesis

The bottom-up approach is the most commonly used in the literature due to its greater versatility and better quantum yield results. In both hydrothermal and microwave-assisted methods, the following processes occur: the formation of intermediates through condensation reactions, followed by polymerization or aggregation, also known as carbon clusters, and nucleation, which is responsible for developing the core at high temperatures. The remaining intermediates can passivate the surface (JELINEK, 2017; LIU et al., 2019b; SONG et al., 2015).

The hydrothermal method uses an autoclave, which allows the creation of a high-temperature isolated system to promote better nucleation. This synthesis generates a high quantum yield, and all classes of CDs can be synthesized depending on the precursor and conditions. It is crucial to note the synthesis conditions, such as temperature and time, which are fundamental to the nucleation process. Low temperatures can result in incomplete carbonization of intermediates, forming free luminophores attached to the surface, while high temperature and prolonged time lead to a more amorphous carbon structure (ANWAR et al., 2019; JELINEK, 2017; LIU et al., 2019b; WU; LIU; YUAN, 2017; XIA et al., 2019).

In the case of microwave-assisted hydrothermal synthesis, temperature is replaced by microwave radiation, which allows faster synthesis, typically taking around 5 minutes to obtain the nanoparticles. This method generally achieves better homogeneity compared to hydrothermal synthesis but with a lower quantum yield. Microwave-assisted synthesis is more prone to incomplete carbonization of intermediates, resulting in free or surface-bound luminophores that can influence the emission process (ANWAR et al., 2019; JELINEK, 2017; TANG et al., 2012).

1.4.4. Carbon dots in solid-state

It is clear that the PL emission mechanism in CDs is not yet fully understood, and its origin is influenced by experimental conditions, such as the nature of the organic precursor and the synthesis temperature. Therefore, spectroscopic investigations focused on studying the PL emission mechanism are essential for advancing this field. Another challenge in the field is the solid-state PL emission self-quenching of CDs.

CDs typically experience aggregation-caused quenching (ACQ), as evidenced by the reduction in PL emission intensity at high suspension concentrations. ACQ is a consequence of the π orbitals overlapping of planar polycyclic aromatic structures, in which the alignment of these structures results in the intermolecular $\pi - \pi$ stacking interactions, triggering nonradiative transitions (MEI et al., 2015; RU; WATERHOUSE; LU, 2022). Wang, Yang and Liu (2020), Ren, Stagi and Innocenzi (2020), and Xu et al (2024) have thoroughly detailed strategies and examples to address this issue. Essentially, these strategies involve creating steric hindrance within the CDs dispersions to prevent ACQ. The most common method to avoid direct contact between the nanoparticles is the physical dispersion of post-synthesized CDs in solid matrices, such as polymers. For instance, Zhu et al. (2013) embedded CDs in polyvinyl alcohol (PVA) by electrospinning, producing nanofiber and bulk poly *N,N'*-dimethylacrylamide (PDMMA) by polymerizing CDs in a DMMA solution. They report the PL emission in solid-state with greater PL stability under constant UV light exposure in comparison to CDs suspensions. Another interesting example is the incorporation of CDs into the culture media of *Gluconacetobacter xylinus*, which produces a cellulose membrane called bacterial cellulose, in this case with PL, as demonstrated by Lv et al. (2019). Although this method is straightforward, it involves a two-step process. In addition, as pointed out by Wang, Yang and Liu (2020), high concentrations are required for practical applications, such as optoelectronics devices.

The "one-step" method is another synthesis strategy to achieve solid-state CDs. In this approach, long-chain structures or polymers are used as precursors along with the CD source to prevent direct contact between the formed nanoparticles. The resulting powder after the drying process can exhibit PL emission. For example, Liu et al. (2019a) used branched poly(ethylenimine) (PEI) with citric acid via the hydrothermal method to obtain green-emissive solid-state CDs in powder form with a quantum yield of 26%. According to the authors, the long chains passivated the CD surface, preventing ACQ. Inorganic hosts can also be used to achieve solid-state PL emission. By incorporating salts, oxides,

mesoporous materials, and layered materials into the CD reaction medium, hydrogen bonding, coordination, and electrostatic interactions may arise between the CD moieties and the inorganic structures. As a result, the nanoparticles remain in a “dispersed state” in powder form, resisting total ACQ (REN; STAGI; INNOCENZI, 2021; XU et al., 2024; YANG et al., 2019b).

The PL emission properties of solid-state CDs can differ from those in suspension form. A red shift or quenching of higher energy states is often observed due to energy transfer between the energy states of the CDs. Chen et al. (2016) and Chang et al. (2019) attributed the red shift in the emission spectra of powdered CD samples to FRET between the aggregated nanoparticles. This hypothesis was supported by the decreased lifetime in powdered samples compared to suspensions, as well as the overlap between the absorption and emission spectra. For example, in the first case, the PL emission in the solid state was achieved by functionalizing CDs with PVA according to the one-step method synthesis. The long chains prevent the $\pi - \pi$ stacking of conventional CDs while maintaining the nanoparticles at a suitable Föster distance (R_0). According to them, this allowed the FRET between the aggregated nanoparticles, resulting in the red-shift observed in the PL emission spectrum of powder samples. Besides the aforementioned lifetime and overlapping evidence to support this hypothesis, they verified a red-shift emission by increasing the CDs concentration in water suspension, the same effect was verified by Zhang et al. (2019). As observed by Zhang et al. (2019), Zhou et al.,(2018) and Song et al. (2019) the emergence of an energy state due to the aggregation is also possible. According to Zhang et al. (2019) monodispersed CDs energy transfer to the aggregate states, leading to a longer wavelength emission. On the other hand, Zhou et al. (2018) hypothesize that intrinsic states or coupled surface states can transfer energy to these aggregate states, resulting in the quenching of higher energy state bands.

Thus, it is possible to employ clay minerals, such as LAPONITE®, to avoid the ACQ by the steric hindrance of the layers on CDs using it as an inorganic host in the synthesis. Three works have been found involving LAPONITE® and CDs nanoparticles. The first was published by Dimos et al.(2017) who fabricated films based on polyethylene terephthalate (PET) by drop-casting suspensions of LAPONITE®-CDs (with previous stirring for 24h and centrifugation); They also created layer-by-layer films on glass substrates using LAPONITE® suspensions combined with a polyanion, followed by the formation of CD layers after LAPONITE® deposition. In both cases, the PL emission of CDs was preserved, and according to XRD results, the CDs remained in the clay’s

interlayer. The CDs were synthesized via microwave using L-arginine and ethylenediamine as precursors. The second work was published by Yang et al. (2019a) who synthesized the hybrid *in situ* using the clay mineral as a host for CDs formation. The precursors used were citric acid and urea, which were heated in an autoclave using acetone as the solvent along with LAPONITE®. The authors evaluated different temperatures and the molar ratio between the precursors, observing multiple color emissions according to changes in these synthesis parameters. According to XRD results, the clay mineral exhibited larger interlayer spaces, which were consistent with the CD sizes confirmed by transmission electron microscopy (TEM). Due to this confined interlayer space, the authors noted that ACQ was avoided, resulting in solid-state emission. The multiple color emissions were related to the extent of graphitization and the amount of carboxylic groups on the surface, with a red shift observed as these parameters increased. The materials were used to develop a white light emitting diode (WLED). The third work published by Zhou et al. (2024) used CDs (not informed the precursors) to obtain full-color luminescence together with the supramolecular tetraphenylethylene (P-TPE) molecule and with RhB. LAPONITE® avoided the free rotation of P-TPE molecule and assisted in the energy transfer between P-TPE to RhB. The white light emission was obtained by tuning the concentration ratios of the blue emitted CDs with the yellow powder P-TPE-LAPONITE®-RhB nanocomposite. The resulting powder was used for multi-level logic digital encryption and sensing perfluorinated pollutants in water as PCS qualitatively by the turn-off method.

Although the reported works, the PL mechanism was not fully elucidated and they did not demonstrate the behavior of the nanocomposite suspension in an aqueous medium, which is one of the aims of Chapter 2 in this thesis. In addition, to demonstrate in Chapter 3 the possibility of using nanocomposite as PCS.

1.4.5. Carbon dots as photoluminescence chemical sensors for heavy metals

One significantly reported CDs application in the literature is as sensors, both chemical, for identifying and quantifying ions and molecules, and physical, such as temperature sensors (LIU et al., 2019b; MOHAMMED; OMER, 2020; XU; LIN; CHANG, 2020). Their solubility in aqueous media and easily modifiable surface make them potential candidates for various biological and environmental applications, adaptable for greater selectivity to the analyte. Additionally, due to their large surface area, surface states are highly sensitive, allowing for easy interaction with the

environment and resulting changes in emission, either as turn-off or turn-on PL emission, which are desirable characteristics in PCS.

Li and Li (2019) summarized the main binding strategies used in the sensing of heavy metals involving CDs, such as coordination and electrostatic bonding. Coordination involves the formation of a complex between functional groups on the CDs and heavy metals in solution, with consequent PL emission quenching used to identify the metal. This strategy employs functional groups similar to the metal in terms of hard and soft acid-base (HSAB) properties to form covalent bonds. Heteroatoms of S, N, O, and P are commonly used to functionalize the surface and create groups to bind with the metal; however, other molecules can be introduced to the surface to increase selectivity to the desired analyte, such as crown complexes where the metal coordinates in the cavities of the macromolecule (LI; LI, 2020).

The electrostatic effect between CDs and heavy metals can occur depending on the pH of the medium. Functional groups can be deprotonated at a pH exceeding the pKa of the species, contributing to the interaction with the positive charge of heavy metals; this is usually observed with hydroxyl, carboxyl, sulfonate, and phosphate groups. A neutral medium also contributes to the deprotonation of acidic groups, such as carboxyls. Some metals in anionic form, like Cr^{6+} in CrO_4^{2-}, tend to bind to positive species, such as amine groups in an acidic medium, which is positively charged when the pH is below the pKa (LI; LI, 2020).

There are several PL emission quenching mechanisms involving CDs-metal besides the collisional and static. For example, during the formation of the CD-metal complex, the *d* orbitals of heavy metals can receive electrons from the excited state of CDs, quenching the PL emission (AHMADIAN-FARD-FINI et al., 2020; RADHAKRISHNAN; SIVANESAN; PANNEERSELVAM, 2020; YOO et al., 2019). This mechanism resembles the photoinduced electron transfer (PET) process and occurs if the LUMO of the CDs has higher energy than the metal's high-energy orbital. In this case, the CDs act as a donor of photoexcited electrons and the metal as an electron acceptor, resulting in the electron returning to the ground state without photon emission in the formed complex. The reverse process is also possible, with the CD acting as an acceptor if the low orbital energy of the metal has a small energy difference from the HOMO of the CD (DEVI et al., 2019; LI; LI, 2020; ZU et al., 2017).

FRET processes can also occur if the CDs and the quencher have dipole-dipole interactions and are at the appropriate distance. This scenario represents indirect sensing,

where a molecule with selectivity for the metal target acts as an acceptor in FRET with the CDs. Typically, metal detection is based on the competition between molecule-metal binding and the FRET process, as the latter interferes with the CDs-quencher interaction (MOLAEI, 2020; SOUZA; SIGOLI, 2012; ZU et al., 2017). Additionally, if there is a match between the redox potentials of the CDs and heavy metals, electron transfer through redox reactions is possible (LI; LI, 2020; ZU et al., 2017).

1.5. ORGANIC LIGHT EMITTING-DIODES (OLED)

The structure formed and the high cationic exchange capacity allow LAPONITE® to form composites with polymers, resulting in an improvement mainly in mechanical properties. LAPONITE® and polymer composites have a wide range of applications, particularly in the field of biomaterials, due to the non-toxicity and biocompatibility of LAPONITE®. Additionally, due to the large surface area and cationic exchange capacity (0.6 – 0.8 meq g^{-1}) (SUMAN; JOSHI, 2018), it can be used as adsorbents for heavy metals. A study published by Silva et al. (2019) reveals an improvement in thermal properties and water permeability due to the addition of synthetic clay mineral to cellulose nanofibers. As demonstrated in the previous topics, LAPONITE® can be applied in the photonic fields to resist the ACQ and PCS. In addition, another interesting application due to its improvement in mechanical properties can be as reinforcement material in OLEDs substrates, aim of the Chapter 4.

Nakamura (2015) describes light-emitting diodes (LEDs) as optoelectronic devices consisting of an active emitting thin layer situated between n-type and p-type semiconductor layers. The n-type layer injects electrons into the active layer (acting as the cathode), while the p-type layer injects holes (serving as the anode). LEDs operate on the principle of electroluminescence, where a forward bias potential causes electrons and holes to recombine radiatively, emitting photons from the active layer with energy corresponding to its band gap. The complete LED structure includes a substrate layer where the active layer “sandwiched” between the p-n junction (with a thickness within the nanometer range) are epitaxially deposited (HELD, 2016; NAKAMURA, 2015). If the active layer is made of an organic electroluminescent compound, typically π-conjugated molecules, the device is known as an organic light-emitting diode (OLED)

(GEFFROY; LE ROY; PRAT, 2006). This active layer is also called an emissive layer (EML). The electrodes are typically made of inorganic materials such as aluminum (Al) for the cathode and tin-doped indium oxide (ITO) for the anode. However, the interface between these electrodes and the emissive layer (EML) presents a large energy barrier for electrons or holes, compromising the OLED's efficiency. To address this, electron or hole injection layers (EIL or HIL, respectively) are introduced below the cathode or above the anode to reduce this energy barrier. When charges travel across the interfaces of the layers to the EML, overflow due to high injection can occur, leading to low efficiencies because of the high probability of nonradiative recombination. To prevent this issue, electron or hole transport layers (ETL or HTL, respectively) with high charge carrier mobility are incorporated. These layers help mitigate the problem by ensuring efficient charge transport from the EIL or HIL to the EML, ensuring the eletrcon-hole recombination in the EML (GASPAR; POLIKARPOV, 2015; JOU et al., 2018).

The classical architecture of OLED can be represented as shown in Figure 1.5(a), and by Figure 1.5(b) it is possible to note that the charge mobility starts from the electrode's Fermi level, going through the LUMO or HOMO (electron or hole respectively) of each neighboring molecule for the final electron-hole recombination.

Regarding the substrates, there are important parameters required for OLED efficiency, as highlighted by Gaspar and Polikarpov (2015), and Bauri, Choudhary and Mandal (2021). The substrate must be:

- Uniform and flat to avoid defects that interfere with the layers' alignment. The roughness should be $R_{rms} < 2$ nm, $R_{max} < 20$nm;
- Transparent, with transmission higher than 90% in the visible spectrum;
- Low oxygen and moisture permeability;
- Low coefficient of thermal expansion.

OLEDs offer several benefits, including higher brightness, lighter weight, faster response times, low power consumption, and suitability for large-area color displays and flexible applications (FARACO et al., 2023; GEFFROY; LE ROY; PRAT, 2006; HELD, 2016). These characteristics enable the use of OLEDs in TV display technologies, including foldable screens. In recent years, there has been increasing interest in wearable and biomedical applications of OLEDs. However, these applications demand significant mechanical flexibility, robust encapsulation, potential for miniaturization, and biocompatibility (GEFFROY; LE ROY; PRAT, 2006; MURAWSKI; GATHER, 2021;

SONG et al., 2020). The rigidity of traditional glass-based OLED substrates primarily obstructs these requirements. Therefore, polymers have been utilized as OLED substrates to address the flexibility concern. However, despite their flexibility, petrochemical polymers used in OLED substrates raise concerns regarding non-degradability, resulting in undesirable environmental pollution. Consequently, interest in "green electronics" has surged (KONG et al., 2022; SU et al., 2022), aiming to create renewable, biodegradable, biocompatible, transparent, and flexible substrates.

To evaluate the OLED display performance, three important measurements can be made. The external quantum efficiency (EQE), luminance and irradiance. According to Schubert (2006), the EQE is the ratio between the emitted photons to the number of injected charged particles, measured by the absolute value of the optical power obtained in an integrated sphere and the injection current obtained by the multimeter respectively. The units are often reported in percentage. Luminance (cd/m^2) is the luminous intensity given in candela unit (cd) divided by the projected surface area, given in m^2. It is measured by a luminance meter. The irradiance can be interpreted as the power density expressed by W/m^2. It is the radiant flux received by a surface, measured by a radiometer or photometer.

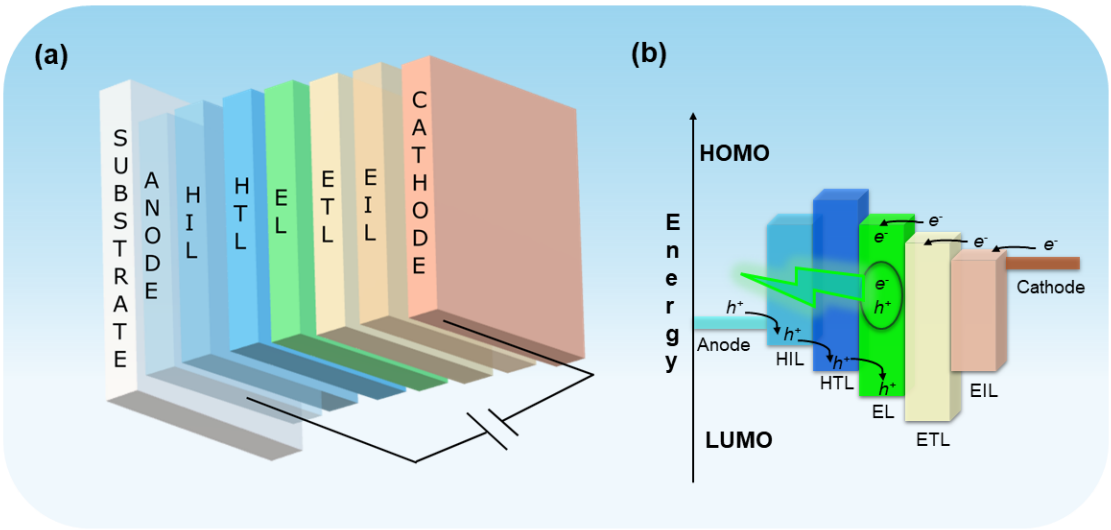

Figure 1.2. Representation of a multilayer OLED's architecture (a) and its respective energy diagram showing the charges mobility to EL. and the electron (e-) - hole (h+) recombination for light emission via electroluminescence (b). Adapted from Bauri, Choudhary and Mandal (2021)

References

AHMADIAN-FARD-FINI, S. et al. Electro-spinning of cellulose acetate nanofibers/Fe/carbon dot as photoluminescence sensor for mercury (II) and lead (II) ions. **Carbohydrate Polymers**, v. 229, n. September 2019, p. 115428, fev. 2020.

ANWAR, S. et al. Recent Advances in Synthesis, Optical Properties, and Biomedical Applications of Carbon Dots. **ACS Applied Bio Materials**, v. 2, n. 6, p. 2317–2338, 17 jun. 2019.

APHA. **Standard Methods For The Examination Of Water And Wastewater**. 23 ed. 2017.

ASSIS, E. M. DE et al. High concentrations of toxic metals in water consumed by the Maxakali indigenous community in Brazil. **Ambiente e Agua - An Interdisciplinary Journal of Applied Science**, v. 14, n. 1, p. 1, 25 jan. 2019.

BAO, L. et al. Electrochemical Tuning of Luminescent Carbon Nanodots: From Preparation to Luminescence Mechanism. **Advanced Materials**, v. 23, n. 48, p. 5801–5806, 22 dez. 2011.

BAURI, J.; CHOUDHARY, R. B.; MANDAL, G. Recent advances in efficient emissive materials-based OLED applications: a review. **Journal of Materials Science**, v. 56, n. 34, p. 18837–18866, 13 dez. 2021.

BECHER, T. B. et al. The structure–property relationship in LAPONITE® materials: from Wigner glasses to strong self-healing hydrogels formed by non-covalent interactions. **Soft Matter**, v. 15, n. 6, p. 1278–1289, 2019.

BERA, D.; QIAN, L.; HOLLOWAY, P. H. Phosphor Quantum Dots. *In:* John Wiley & Sons, Ltd **Luminescent materials and Applications.** 2008

BEYERSMANN, D.; HARTWIG, A. Carcinogenic metal compounds: Recent insight into molecular and cellular mechanisms. **Archives of Toxicology**, v. 82, n. 8, p. 493–512, 2008.

BIMBERG, D.; GRUNDMANN, M.; LEDENTSOV, N. **Quantum dot heterostructures**John Wiley & Sons, , 1999.

BIMBERG, D.; POHL, U. W. Quantum dots: Promises and accomplishments. **Materials Today**, v. 14, n. 9, p. 388–397, 2011.

BONN, D. et al. Laponite : What Is the Difference between a Gel and a Glass ? n. 14, p. 7534–7536, 1999.

BURAKOV, A. E. et al. Adsorption of heavy metals on conventional and nanostructured materials for wastewater treatment purposes: A review. **Ecotoxicology and Environmental Safety**, v. 148, n. November 2017, p. 702–712, fev. 2018.

CARNEIRO NETO, A. N. et al. Modeling intramolecular energy transfer in lanthanide chelates: A critical review and recent advances. In: Elsevier B.V. **Handbook on the Physics and Chemistry of Rare Earths,** volume 56. 2019. p. 55–162.

CARVALHO, M. S. DE et al. Concentração de metais no rio Doce em Mariana, Minas Gerais, Brasil. **Acta Brasiliensis**, v. 1, n. 3, p. 37, 26 set. 2017.

CHANG, Q. et al. Quench-resistant and stable nanocarbon dot/sheet emitters with tunable solid-state fluorescence via aggregation-induced color switching. **Nanoscale**, v. 11, n. 5, p. 2131–2137, 2019.

CHEN, Y. et al. A Self-Quenching-Resistant Carbon-Dot Powder with Tunable Solid-State Fluorescence and Construction of Dual-Fluorescence Morphologies for White Light-Emission. **Advanced Materials**, v. 28, n. 2, p. 312–318, 16 jan. 2016.

CHOWDHURY, M. Selection Rules For Processes Involving Photon-Molecule Interaction: A Symmetry-Conservation-Based Approach Bypassing Transition Matrix Elements. **Journal of Chemical Education**, v. 73, n. 8, p. 743, 1 ago. 1996.

CONAMA. **Resolução 430/2011**.

DA SILVA, Y. J. A. B. et al. Heavy metal concentrations and ecological risk assessment of the suspended sediments of a multi-contaminated Brazilian watershed. **Acta Scientiarum - Agronomy**, v. 41, n. 1, p. 1–11, 2019.

DAS, S. S. et al. Laponite-based Nanomaterials for Biomedical Applications: A Review. p. 424–443, 2019.

DÉCSINÉ, E. et al. Laponite immobilized TiO2 catalysts for photocatalytic degradation of phenols. **Journal of Photochemistry & Photobiology, A: Chemistry**, v. 387, n. August 2019, p. 112045, 2020.

DEKALIUK, M. O. et al. Fluorescent carbon nanomaterials: "quantum dots" or nanoclusters? **Phys. Chem. Chem. Phys.**, v. 16, n. 30, p. 16075–16084, 2014.

DEVI, P. et al. Recent advances in carbon quantum dot-based sensing of heavy metals in water. **TrAC Trends in Analytical Chemistry**, v. 114, p. 171–195, maio 2019.

DEY, D. et al. Effect of nanoclay laponite and pH on the energy transfer between fluorescent dyes. **Journal of Photochemistry and Photobiology A: Chemistry**, v. 252, p. 174–182, jan. 2013.

DIMOS, K. et al. Top-down and bottom-up approaches to transparent, flexible and luminescent nitrogen-doped carbon nanodot-clay hybrid films. **Nanoscale**, v. 9, n. 29, p. 10256–10262, 2017.

DING, H. et al. Full-Color Light-Emitting Carbon Dots with a Surface-State-Controlled Luminescence Mechanism. **ACS Nano**, v. 10, n. 1, p. 484–491, 26 jan. 2016.

DONG, Y. et al. Carbon-Based Dots Co-doped with Nitrogen and Sulfur for High Quantum Yield and Excitation-Independent Emission. **Angewandte Chemie International Edition**, v. 52, n. 30, p. 7800–7804, 22 jul. 2013.

DUFFUS, J. H. "Heavy metals" a meaningless term? (IUPAC Technical Report). **Pure and Applied Chemistry**, v. 74, n. 5, p. 793–807, 1 jan. 2002.

ELLIS, A. M. Spectroscopic Selection Rules: The Role of Photon States. **Journal of Chemical Education**, v. 76, n. 9, p. 1291, 1 set. 1999.

EPA. **Potential Export of Mercury Compounds from the United States for Conversion to Elemental Mercury**, 2009

FARACO, T. A. et al. Review of Bacterial Nanocellulose as Suitable Substrate for Conformable and Flexible Organic Light-Emitting Diodes. **Polymers**, v. 15, n. 3, p. 1–16, 2023.

FERY-FORGUES, S.; LAVABRE, D. Are fluorescence quantum yields so tricky to measure? A demonstration using familiar stationery products. **Journal of Chemical Education**, v. 76, n. 9, p. 1260–1264, 1 set. 1999.

FRAIJI, L. K.; HAYES, D. M.; WERNER, T. C. Static and dynamic fluorescence quenching experiments for the physical chemistry laboratory. **Journal of Chemical Education**, v. 69, n. 5, p. 424, 1 maio 1992.

GASPAR, D. J.; POLIKARPOV, E. **OLED fundamentals: Materials, devices, and processing of organic light-emitting diodes**. Taylor & Francis group. 2015.

GEFFROY, B.; LE ROY, P.; PRAT, C. Organic light-emitting diode (OLED) technology: Materials, devices and display technologies. **Polymer International**, v. 55, n. 6, p. 572–582, 2006.

GILMOUR, C. C. et al. Sulfate-Reducing Bacterium Desulfovibrio desulfuricans ND132 as a Model for Understanding Bacterial Mercury Methylation. **Applied and Environmental Microbiology**, v. 77, n. 12, p. 3938–3951, 15 jun. 2011.

GONCALVES, A. C. et al. Heavy Metal Contamination in Brazilian Agricultural Soils due to Application of Fertilizers. In: InTech. **Environmental Risk Assessment of Soil Contamination**., 2014.

GUDE, V. et al. Molecular origin of photoluminescence of carbon dots: aggregation-induced orange-red emission. **Physical Chemistry Chemical Physics**, v. 18, n. 40, p. 28274–28280, 2016.

GUERRA, N. et al. Operation and physics of photovoltaic solar cells: an overview. **I+D Tecnológico**, v. 14, n. 2, p. 84–95, 14 dez. 2018.

HELD, G. **Introduction to Light Emitting Diode Technology and Applications**. Auerbach Publications, 2016.

HINTERBERGER, V. et al. Purification and structural elucidation of carbon dots by column chromatography. **Nanoscale**, v. 11, n. 17, p. 8464–8474, 2019.

HONG, Y.-S.; KIM, Y.-M.; LEE, K.-E. Methylmercury Exposure and Health Effects. **Journal of Preventive Medicine & Public Health**, v. 45, n. 6, p. 353–363, 29 nov. 2012.

HORIBA. **Time-resolved fluorescence lifetime measurements**. available in: <https://static.horiba.com/fileadmin/Horiba/Products/Scientific/Molecular_and_Microanalysis/DeltaFlex/TechNote-1b-Time-resolved_fluorescence_lifetime_measurements.pdf>.

HU, M. Z.; ZHU, T. Semiconductor Nanocrystal Quantum Dot Synthesis Approaches Towards Large-Scale Industrial Production for Energy Applications. **Nanoscale Research Letters**, v. 10, n. 1, p. 469, 4 dez. 2015.

HUANG, X.; ZHI, C. **Polymer Nanocomposites**. Cham: Springer International Publishing, 2016.

JATAV, S.; JOSHI, Y. M. Chemical stability of Laponite in aqueous media. **Applied Clay Science**, v. 97–98, p. 72–77, 2014.

JELINEK, R. **Carbon Quantum Dots**. Cham: Springer International Publishing, 2017.

JOE, H. et al. A review on optical fiber sensors for environmental monitoring. **International Journal of Precision Engineering and Manufacturing-Green Technology**, v. 5, n. 1, p. 173–191, 14 jan. 2018.

JOO, J. C. et al. Photocatalytic degradation of trichloroethylene in aqueous phase using nano-ZNO/Laponite composites. **Journal of Hazardous Materials**, v. 263, p. 569–574, dez. 2013.

JOU, J. et al. Investigation of charge-transporting layers for high-efficiency organic light-emitting diode. **Journal of Physics D: Applied Physics**, v. 51, n. 45, p. 454002, 14 nov. 2018.

KASPRZYK, W. et al. Novel efficient fluorophores synthesized from citric acid. **RSC Advances**, v. 5, n. 44, p. 34795–34799, 2015.

KASPRZYK, W. et al. The role of molecular fluorophores in the photoluminescence of carbon dots derived from citric acid: current state-of-the-art and future perspectives. **Nanoscale**, v. 14, n. 39, p. 14368–14384, 2022.

KAZANTZIS, G. Cadmium, osteoporosis and calcium metabolism. **BioMetals**, v. 17, n. 5, p. 493–498, 2004.

KLAASSEN, C.; EATON, D. **The Basic Science of Poisons, 4th ed**, 1991.

KONG, D. et al. Biocompatible and Biodegradable Light-Emitting Materials and Devices. **Advanced Materials Technologies**, v. 7, n. 2, p. 1–17, 18 fev. 2022.

KOZÁK, O. et al. Photoluminescent Carbon Nanostructures. **Chemistry of Materials**, v. 28, n. 12, p. 4085–4128, 28 jun. 2016.

LAKOWICZ, J. R. **Principles of Fluorescence Spectroscopy**. 3. ed. Springer, 2006.

LANGER, M. et al. Progress and challenges in understanding of photoluminescence properties of carbon dots based on theoretical computations. **Applied Materials Today**, v. 22, p. 100924, mar. 2021.

LI, H. et al. Water-Soluble Fluorescent Carbon Quantum Dots and Photocatalyst Design. **Angewandte Chemie International Edition**, v. 49, n. 26, p. 4430–4434, 14 jun. 2010.

LI, L.; DONG, T. Photoluminescence tuning in carbon dots: surface passivation or/and functionalization, heteroatom doping. **Journal of Materials Chemistry C**, v. 6, n. 30, p. 7944–7970, 2018.

LI, M. et al. Nanostructured Sensors for Detection of Heavy Metals: A Review. **ACS Sustainable Chemistry & Engineering**, v. 1, n. 7, p. 713–723, 13 jul. 2013.

LI, P.; LI, S. F. Y. Recent advances in fluorescence probes based on carbon dots for sensing and speciation of heavy metals. **Nanophotonics**, v. 10, n. 2, p. 877–908, 11 dez. 2020.

LIU, E. et al. Highly Emissive Carbon Dots in Solid State and Their Applications in Light-Emitting Devices and Visible Light Communication. **ACS Sustainable Chemistry**

and Engineering, v. 7, n. 10, p. 9301–9308, 2019a.

LIU, M. L. et al. Carbon dots: synthesis, formation mechanism, fluorescence origin and sensing applications. **Green Chemistry**, v. 21, n. 3, p. 449–471, 2019b.

LV, P. et al. In situ 3D bacterial cellulose/nitrogen-doped graphene oxide quantum dot-based membrane fluorescent probes for aggregation-induced detection of iron ions. **Cellulose**, v. 26, n. 10, p. 6073–6086, 2019.

MALTA, O. L. Mechanisms of non-radiative energy transfer involving lanthanide ions revisited. **Journal of Non-Crystalline Solids**, v. 354, n. 42–44, p. 4770–4776, 2008.

MARIA J. RODRIGO; MARIA J. CARDIEL; JOSE M. FRAILE; JOSE A. MAYORAL; LUIS E. PABLO; ELENA GRACIA-MARTINS. Laponite for biomedical applications: An ophthalmological perspective. **Materials Today Bio**, v. 24, p. 100935, 2024.

MASINDI, V.; MUEDI, K. L. Environmental Contamination by Heavy Metals. In: InTech**. Heavy Metals**. 2018.

MEI, J. et al. Aggregation-Induced Emission: Together We Shine, United We Soar! **Chemical Reviews**, v. 115, n. 21, p. 11718–11940, 11 nov. 2015.

MINTZ, K. J.; ZHOU, Y.; LEBLANC, R. M. Recent development of carbon quantum dots regarding their optical properties, photoluminescence mechanism, and core structure. **Nanoscale**, v. 11, n. 11, p. 4634–4652, 2019.

MISHRA, S. et al. Heavy Metal Contamination: An Alarming Threat to Environment and Human Health. In: **Environmental Biotechnology: For Sustainable Future**. Singapore: Springer Singapore, 2019. p. 103–125.

MOHAMMED, L. J.; OMER, K. M. Carbon Dots as New Generation Materials for Nanothermometer: Review. **Nanoscale Research Letters**, v. 15, n. 1, p. 182, 22 dez. 2020.

MOLAEI, M. J. Principles, mechanisms, and application of carbon quantum dots in sensors: a review. **Analytical Methods**, v. 12, n. 10, p. 1266–1287, 2020.

MURAWSKI, C.; GATHER, M. C. Emerging Biomedical Applications of Organic Light-Emitting Diodes. p. 2100269, 17 jul. 2021.

MURPHY, C. J. Peer Reviewed: Optical Sensing with Quantum Dots. **Analytical Chemistry**, v. 74, n. 19, p. 520 A-526 A, out. 2002.

N CARNEIRO NETO, A. et al. A Tutorial Review on the Nonradiative Energy Transfer Rates between Lanthanide Ions. **Chinese Journal of Luminescence**, v. 43, n. 12, p. 1871–1891, 2022.

NAKAMURA, S. Nobel Lecture: Background story of the invention of efficient blue InGaN light emitting diodes. **Reviews of Modern Physics**, v. 87, n. 4, p. 1139–1151, 5 out. 2015.

NIESSNER, H. P. A. G. R. Detection of heavy metals in water by fluorescence spectroscopy : On the way to a suitable sensor system. p. 182–191, 2000.

NOBRE, S. S. et al. Energy transfer and emission quantum yields of organic-inorganic hybrids lacking metal activator centers. **Journal of Physical Chemistry C**, v. 111, n. 8, p. 3275–3284, 2007.

PEROTTI, G. F. et al. Bacterial cellulose–laponite clay nanocomposites. **Polymer**, v. 52, n. 1, p. 157–163, jan. 2011.

PILAVTEPE, M. et al. Macro- and microscale structure formation and aging in different arrested states of Laponite dispersions. **Journal of Rheology**, v. 62, n. 2, p. 593–605, 2018.

RADHAKRISHNAN, K.; SIVANESAN, S.; PANNEERSELVAM, P. Turn-On fluorescence sensor based detection of heavy metal ion using carbon dots@graphitic-carbon nitride nanocomposite probe. **Journal of Photochemistry and Photobiology A: Chemistry**, v. 389, p. 112204, 2020.

RASHEED, T. et al. Fluorescent sensor based models for the detection of environmentally-related toxic heavy metals. **Science of The Total Environment**, v. 615, p. 476–485, fev. 2018.

RAY, S. C. et al. Fluorescent Carbon Nanoparticles: Synthesis, Characterization, and Bioimaging Application. **The Journal of Physical Chemistry C**, v. 113, n. 43, p. 18546–18551, 29 out. 2009.

REN, J.; STAGI, L.; INNOCENZI, P. Fluorescent carbon dots in solid-state: From nanostructures to functional devices. **Progress in Solid State Chemistry**, v. 62, n. xxxx, p. 100295, jun. 2021.

RONDA, C. **Luminescence From theory to aplication**. Wiley-VHC, 2008.

RU, Y.; WATERHOUSE, G. I. N.; LU, S. Aggregation in carbon dots. **Aggregate**, v. 3, n. 6, p. 1–14, 21 dez. 2022.

RUZICKA, B.; ZACCARELLI, E. REVIEW A fresh look at the Laponite phase diagram. p. 1268–1286, 2011.

SCHUBERT, F. E. **Light-emitting Diodes**. 2. ed. Cambridge University Press, 2006.

SHI, X. et al. (EDS.). **Molecular Mechanisms of Metal Toxicity and Carcinogenesis**. Boston, MA: Springer US, 2001.

SILVA, J. M. et al. Inorganic-organic bio-nanocomposite films based on Laponite and Cellulose Nanofibers (CNF). **Applied Clay Science**, v. 168, n. September 2018, p. 428–435, fev. 2019.

SONG, J. et al. Organic Light-Emitting Diodes: Pushing Toward the Limits and Beyond. **Advanced Materials**, v. 32, n. 35, p. 1–17, 2020.

SONG, T. et al. Color-tunable carbon dots via control the degree of self-assembly in solution at different concentration. **Journal of Luminescence**, v. 212, n. December 2018, p. 69–75, 2019.

SONG, Y. et al. Investigation from chemical structure to photoluminescent mechanism: a type of carbon dots from the pyrolysis of citric acid and an amine. **Journal of Materials Chemistry C**, v. 3, n. 23, p. 5976–5984, 2015.

SOUZA, JULIANA, S.; BATISTA, G.; BERNSTEIN, A. Mercúrio na Amazônia : a

bomba relógio bioquímica Toxicologia do mercúrio. **Revista Educação Pública**, p. 1–8, 2014.

SOUZA, A. M. et al. Seasonal study of concentration of heavy metals in waters from lower São Francisco River basin, Brazil. **Brazilian Journal of Biology**, v. 76, n. 4, p. 967–974, 2016.

SOUZA, J. R. DE; BARBOSA, A. C. Contaminação por mercúrio e o caso da Amazônia. **Química Nova na Escola**, v. 12, p. 3–7, 2000.

SOUZA, E. R.; SIGOLI, F. A. Princípios fundamentais e modelos de transferência de energia inter e intramolecular. **Química Nova**, v. 35, n. 9, p. 1841–1847, 2012.

SU, Z. et al. Designed biomass materials for “green” electronics: A review of materials, fabrications, devices, and perspectives. **Progress in Materials Science**, v. 125, n. August 2020, p. 100917, 2022.

SUMAN, K.; JOSHI, Y. M. Microstructure and Soft Glassy Dynamics of an Aqueous Laponite Dispersion. 2018.

SUN, Y.-P. et al. Quantum-Sized Carbon Dots for Bright and Colorful Photoluminescence. **Journal of the American Chemical Society**, v. 128, n. 24, p. 7756–7757, jun. 2006.

TANG, J. et al. Influence of Group Modification at the Edges of Carbon Quantum Dots on Fluorescent Emission. **Nanoscale Research Letters**, v. 14, n. 1, p. 241, 2 dez. 2019.

TANG, L. et al. Deep Ultraviolet Photoluminescence of Water-Soluble Self-Passivated Graphene Quantum Dots. **ACS Nano**, v. 6, n. 6, p. 5102–5110, 26 jun. 2012.

TCHOUNWOU, P. B. et al. Heavy Metal Toxicity and the Environment. In: Springer Basel. **Molecular, Clinical and Environmental Toxicology**. 2012. v. 101p. 133–164.

THOMPSON, D. W.; BUTTERWORTH, J. T. The Nature of Laponite and Its Aqueous Dispersions pH Titration of Laponite Dispersions Analysis of Laponite Dispersion Media and Measurements. **Journal of Colloid and Interface Science**, v. 15, n. I, p. 236–243, 1992.

UDDIN, M. K. A review on the adsorption of heavy metals by clay minerals, with special focus on the past decade. **Chemical Engineering Journal**, v. 308, p. 438–462, jan. 2017.

ULLAH, N. et al. Nanomaterial-based optical chemical sensors for the detection of heavy metals in water: Recent advances and challenges. **TrAC Trends in Analytical Chemistry**, v. 100, p. 155–166, mar. 2018.

VALEUR, B. **Molecular Fluorescence Principles and Application**. Wiley-VHC, 2001.

VALKO, M.; MORRIS, H.; CRONIN, M. Metals, Toxicity and Oxidative Stress. **Current Medicinal Chemistry**, v. 12, n. 10, p. 1161–1208, 1 maio 2005.

WANG, J. et al. High Performance Photoluminescent Carbon Dots for In Vitro and In Vivo Bioimaging: Effect of Nitrogen Doping Ratios. **Langmuir**, v. 31, n. 29, p. 8063–8073, 28 jul. 2015.

WANG, J.; YANG, Y.; LIU, X. Solid-state fluorescent carbon dots: Quenching resistance strategies, high quantum efficiency control, multicolor tuning, and applications. **Materials Advances**, v. 1, n. 9, p. 3122–3142, 2020.

WANG, S. et al. The dual roles of functional groups in the photoluminescence of graphene quantum dots. **Nanoscale**, v. 8, n. 14, p. 7449–7458, 2016.

WU, Z. L.; LIU, Z. X.; YUAN, Y. H. Carbon dots: materials, synthesis, properties and approaches to long-wavelength and multicolor emission. **Journal of Materials Chemistry B**, v. 5, n. 21, p. 3794–3809, 2017.

XIA, C. et al. Evolution and Synthesis of Carbon Dots: From Carbon Dots to Carbonized Polymer Dots. **Advanced Science**, v. 6, n. 23, p. 1901316, 30 dez. 2019.

XU, D.; LIN, Q.; CHANG, H. Recent Advances and Sensing Applications of Carbon Dots. **Small Methods**, v. 4, n. 4, p. 1900387, abr. 2020.

XU, M. et al. A green heterogeneous synthesis of N-doped carbon dots and their photoluminescence applications in solid and aqueous states. **Nanoscale**, v. 6, n. 17, p. 10307–10315, 2014.

XU, W. et al. Recent advancements of solid-state emissive carbon dots: A review. **Coordination Chemistry Reviews**, v. 498, p. 215469, 2024.

XU, X. et al. Electrophoretic Analysis and Purification of Fluorescent Single-Walled Carbon Nanotube Fragments. **Journal of the American Chemical Society**, v. 126, n. 40, p. 12736–12737, out. 2004.

YANG, D.; WANG, J.; LI, H. Photo- and thermo-stable luminescent nanocomposite resulting from hybridization of Eu(III)-β-diketonate complexes with laponite. **Dyes and Pigments**, v. 118, n. Iii, p. 53–57, jul. 2015.

YANG, J. et al. Visual multiple color emission of solid-state carbon dots. **Journal of Materials Chemistry C**, v. 7, n. 25, p. 7806–7811, 2019a.

YANG, Z. et al. Recent advances in quantum dot-based light-emitting devices: Challenges and possible solutions. **Materials Today**, v. 24, n. xx, p. 69–93, abr. 2019b.

YOO, D. et al. Carbon Dots as an Effective Fluorescent Sensing Platform for Metal Ion Detection. **Nanoscale Research Letters**, v. 14, n. 1, 2019.

YU, J. et al. Luminescence Mechanism of Carbon Dots by Tailoring Functional Groups for Sensing Fe3+ Ions. **Nanomaterials**, v. 8, n. 4, p. 233, 12 abr. 2018.

YU, P. et al. Temperature-Dependent Fluorescence in Carbon Dots. **The Journal of Physical Chemistry C**, v. 116, n. 48, p. 25552–25557, 6 dez. 2012.

ZHANG, Y. et al. One-step microwave synthesis of N-doped hydroxyl-functionalized carbon dots with ultra-high fluorescence quantum yields. **Nanoscale**, v. 8, n. 33, p. 15281–15287, 2016.

ZHANG, Y. et al. Solid-State Fluorescent Carbon Dots with Aggregation-Induced Yellow Emission for White Light-Emitting Diodes with High Luminous Efficiencies. **ACS Applied Materials and Interfaces**, v. 11, n. 27, p. 24395–24403, 2019.

ZHAO, L. Z. et al. Recent advances in clay mineral-containing nanocomposite hydrogels. **Soft Matter**, v. 11, n. 48, p. 9229–9246, 2015.

ZHOU, W. L. et al. Laponite-activated AIE supramolecular assembly with modulating multicolor luminescence for logic digital encryption and perfluorinated pollutant detection. **Biosensors and Bioelectronics**, v. 258, n. April, p. 116343, 2024.

ZHOU, Z. et al. Hydrogen Peroxide-Treated Carbon Dot Phosphor with a Bathochromic-Shifted, Aggregation-Enhanced Emission for Light-Emitting Devices and Visible Light Communication. **Advanced Science**, v. 5, n. 8, 2018.

ZHU, S. et al. Highly Photoluminescent Carbon Dots for Multicolor Patterning, Sensors, and Bioimaging. **Angewandte Chemie**, v. 125, n. 14, p. 4045–4049, 2013a.

ZHU, S. et al. Highly Photoluminescent Carbon Dots for Multicolor Patterning, Sensors, and Bioimaging. **Angewandte Chemie International Edition**, v. 52, n. 14, p. 3953–3957, 2 abr. 2013b.

ZHU, S. et al. The photoluminescence mechanism in carbon dots (graphene quantum dots, carbon nanodots, and polymer dots): current state and future perspective. **Nano Research**, v. 8, n. 2, p. 355–381, 19 fev. 2015.

ZU, F. et al. The quenching of the fluorescence of carbon dots: A review on mechanisms and applications. **Microchimica Acta**, v. 184, n. 7, p. 1899–1914, 30 jul. 2017.

Objectives

The aim of this thesis is the investigation of LAPONITE® in the photonic field, specifically as a nanoplatform for the synthesis of CDs, its influence on PL emission properties and the application as PCS for ions Hg^{2+} detection through PL emission quenching. Additionally, this research explores the potential of LAPONITE® reinforcement material for OLEDs substrates. The specific aims can be summarize as:

- Synthesis and characterization (XRD, FTIR, XPS, STEM and MEV) of the nanocomposite **1** based on CDs/LAPONITE®;
- Investigation of the precursor concentration and synthesis pH in the nanocoposite **1** structure;
- Investigation of the nanocomposite's **1** PL emission properties in solid-state and in aqueous medium using room (298 K) and low (13 K) temperature PL spectroscopy (Excitation, emission and emission decay);
- Evaluation of energy transfer process involving in the solid-state nanocomposite **1** using Förster-Dexter model;
- Application of the nanocomposite **1** in aqueous medium as Hg^{2+} detection using PL emission quenching;
- Evaluation of Hg^{2+} quenching mechanisms using Stern-Volmer models;
- Synthesis and characterization (XRD, FTIR, Solid state ^{13}C,^{29}Si – NMR, TGA and tensile strength) of the nanocomposite **2** carboxymethyl cellulose/hyalluronic acid/ LAPONITE®;
- Evaluation of the clay mineral concentration in structure of nanocomposite **2**;
- Application of nanocomposite **2** as OLED substrate and characterization (irradiance, EQE and luminance).

CHAPTER 2

Carbon Dots on LAPONITE® Hybrid Nanocomposites: Solid-State Emission and Inter-aggregate Energy Transfer

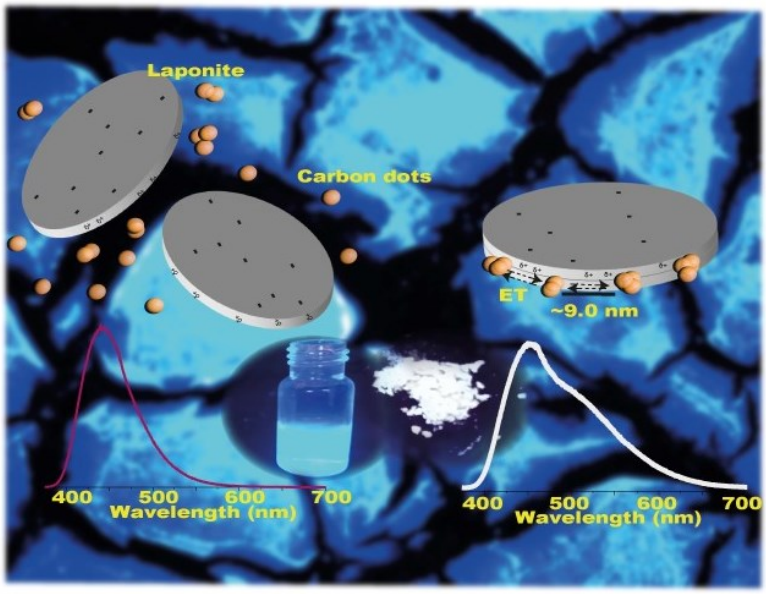

Solid-state and aqueous emission by hybrids nanocomposites based on Carbon Dots/LAPONITE® - energy trasnfer (ET) between aggregates

2. Carbon Dots on LAPONITE® Hybrid Nanocomposites: Solid-State Emission and Inter-aggregate Energy Transfer†

Bruno S. D. Onishi,[a,b] Albano N. Carneiro Neto,[a] Ricardo Bortolleto-Santos,[c] Valmor R. Masterlaro,[d] Luís D. Carlos,[a] Rute A. S. Ferreira,*[a] Sidney J. L. Ribeiro*[b]

Abstract

This study delves into the photoluminescent characteristics of solid-state hybrid carbon dots/LAPONITE® (CDLP). These hybrid materials were synthesized using the hydrothermal method with a precise pH control set at 8.5. The LAPONITE® structure remains intact without structural collapse, and we detected the possible deposition of carbon dots (CDs) aggregates on the clay mineral's edges. The use of different concentrations of citric acid (10-, 6-, 2- and 1-times weight/weight of LAPONITE® mass, maintaining the 1:1 molar ratio with ethylenediamine) during synthesis results in different CDs concentrations in CDLP-A (low precursors concentration) and CDLP-D (high concentration) with an amorphous structure and average size around 2.8-3.0 nm. The CDLP displayed visible photoluminescence emission in aqueous and powder, which the last underwent quenching according to lifetimes and quantum yield measurements. Low-temperature measurements revealed an enhancement of the non-radiative pathways induced by aggregation. Energy transfer modeling based on Förster-Dexter suggests an approximate mean distance of 9.5 nm between clusters of CDs.

Received 12th December 2023, Accepted 3rd March 2024

DOI: 10.1039/d3nr06336d

a. Department of Physics and CICECO – Aveiro Institute of Materials, University of Aveiro, 3810-193 Aveiro, Portugal

b. Institute of Chemistry, São Paulo State University─UNESP, São Paulo, Araraquara, 14800-060, Brazil

c. Postgraduate Program in Environmental Technology, University of Ribeirão Preto─UNAERP, São Paulo, Ribeirão Preto, 14096-900, Brazil

d. São Carlos Institute of Chemistry, University of São Paulo─USP, São Paulo, São Carlos, 13566-590, Brazil

Electronic Supplementary Information (ESI) available. See DOI: https://doi.org/10.1039/d3nr06336d

2.1. Introduction

Carbon dots (CDs) are typically described as carbon nanoparticles consisting of both a carbonaceous amorphous or crystalline core and surface organic functional groups. They exhibit an average size ranging from 1 to 30 nm. Key attributes of CDs encompass tunable photoluminescence emissions within the visible spectrum, biocompatibility, and solubility in aqueous solutions. Since their discovery in 2004 by Scrivens' group,[1] considerable efforts have been devoted to elucidating the underlying photoluminescence mechanism.

CDs are easily synthesized from organic compounds and biomass sources[2–4] using hydrothermal or solvothermal techniques, with their properties heavily influenced by synthesis conditions such as temperature and time of reaction.[5–7] Consequently, there is no universal protocol for determining CDs structure based solely on its precursor, as CDs exhibit unique structures shaped by experimental conditions.

The photoluminescence emission mechanism in CDs remains unclear, with studies attributing it to factors such as quantum confinement,[8–11] surface states introduced by various functional groups,[9–12] the amount of oxygen in the core,[10,11,13] and the presence of luminescent by-products on the surface.[10,11,14,15] Therefore, spectroscopic investigations aimed at elucidating the underlying photoluminescence mechanism are essential.

Another challenge in the field is solid-state photoluminescence emission self-quenching of CDs powders due $\pi - \pi$ stacking and excessive nonradiative energy transfer triggered by aggregation-caused quenching.[16,17] Wang *et al.* [16] and Ren, Stagi and Innocenzi [17] have extensively described strategies to overcome this problem, which in summary, are related to inducing a steric hindrance between CDs dispersion to avoid the aggregation-caused quenching. Among the mentioned examples, the physical dispersion of CDs in solid matrices, such as polymers, is commonly employed due to the excellent dispersity of CDs in various solvents. However, as noted by Wang *et al.,*[16] the photoluminescence emission quenching remains in applications requiring high CDs concentration. An alternative approach to achieve solid-state emission is the *in situ* method using inorganic hosts. They can establish strong interactions, such as hydrogen bonding, complexation, and electrostatic interactions, between the organic surface groups of CDs and the inorganic matrix,[16–19] keeping the nanoparticles dispersed in solid-state.[16] Examples of inorganic hosts include salts like $BaSO_4$,[20] oxides such as ZnO,[21]

mesoporous materials like zeolites[22] and layered materials such as saponite[23] and montmorillonite.[19] The latter example is particularly interesting because its structure is based on interlayer spacing with a nanometric scale, providing a confined space that acts as nanoplatforms for CDs synthesis and offers the steric hindrance required.

LAPONITE® is a synthetic clay mineral with an empirical formula of $Na_{0.7}Si_8Mg_{5.5}Li_{0.3}O_{20}(OH)_4$, belonging to the smectite family, which is a group of layered silicate minerals consisting of alternating tetrahedron-octahedron-tetrahedron (TOT) layers. In this structure, the O layer represents octahedrally arranged Mg-O groups, sandwiched between two T layers containing tetrahedrally organized Si-O groups also known as a 2:1 structure.[24,25] The octahedral center is coordinated by oxygen anions and hydroxyl groups, while the tetrahedral center is predominantly coordinated by oxygen. Isomorphic substitution of Mg^{2+} by Li^{+} occurs in LAPONITE® resulting in negative charges on the surface between the layers, which Na^{+} counterbalances.[24,25] The LAPONITE® layers have nanodisc-shaped morphology with a diameter of ~25 nm and a thickness of ~1 nm. When dispersed in water, they undergo exfoliation where they interact with each other through electrostatic attractive forces between the face and edge, repulsive forces between face-face and edge-edge, and van der Waals interactions.[24]

Yang *et al.*[26] previously demonstrated the utilization of a CD/LAPONITE® hybrid for white light emitting diodes (WLED) applications, achieving tunable photoluminescence emission by varying the proportions of the precursors. Their synthesis method involved solvothermal treatment using citric acid and urea. Furthermore, there was no mention of the possibility of dispersing the samples in an aqueous medium, and the underlying mechanism responsible for the solid-state photoluminescence emission was not thoroughly investigated.

This study used a hydrothermal synthesis method involving citric acid and ethylenediamine, varying the concentrations of the precursors. The synthesized samples are easily dispersed in aqueous solutions. We conducted comprehensive photoluminescence measurements at room temperature (298 K) and low temperature (13 K) to explore the origin of solid-state photoluminescence in CD/LAPONITE®. We introduced a Förster-Dexter-type non-radiative energy transfer model to explore the interactions among CDs aggregates. This model incorporates empirical parameters, including the photoluminescence decay involved in the energy transfer processes (i.e., emissions at 450 and 575 nm), measured at 13 and 298 K. Estimates from the model indicate an average distance of 9.5 nm between CDs aggregations in the CDLP-D sample.

2.2. Experimental

2.2.1. Materials

Citric acid monohydrate was purchased from Synth (Brazil); ethylenediamine was purchased from Vetec (Brazil); synthetic LAPONITE®® RD was kindly supplied by Buntech (Brazil). NaOH was purchased from Sigma Aldrich. All the chemicals were used as received.

2.2.2. Synthesis of CDs

CDs synthesis was performed by the hydrothermal method according to Zhu *et al.*[27] with modifications. Citric acid and ethylenediamine 1:1 molar ratio (5.0049 g and 1,690 μL) were dissolved in 50 mL of ultrapure water within a Teflon liner settled inside a stainless-steel autoclave. This system was heated at 180 °C for 6 h using a muffle furnace (EDG3000), followed by centrifugation at 10,000 rpm (Eppendorf 5804/5804 R) for 15 min after cooling at room temperature. Then, it was filtered using a Nylon membrane filter 0.22 μm (Unifil) and purified by dialysis using 3.5 kDa (MWCO) dialysis membranes (Pur-A-Lyser^{TM}), each 10 mL of the suspension, against 2 L of de-ionized water for 96 h with three water replacements each day. Finally, the yellowish suspension was freeze-dried using a lyophilizer (Liotop) to obtain the powder. The sample was nominated as CD.

2.2.3. Synthesis of CD-LAPONITE® Hybrids

To synthesize the hybrids samples, an *in situ* approach was employed within the CD reaction medium. 1% (weight/volume = w/v) of LAPONITE® was suspended in 50 mL of ultrapure water under vigorous stirring and 10 minutes of sonication to achieve complete dispersion of the synthetic clay mineral. The resulting gelatinous and transparent suspension was maintained under stirring, and citric acid and ethylenediamine were added. The pH was then adjusted to 8.5 with 0.1 M NaOH, and the mixture was subjected to the same hydrothermal conditions as CD. After the synthesis period, the gelatinous yellowish suspension was centrifuged at 10,000 rpm for 15 minutes, washed with ultrapure water and ethanol p.a. several times, and freeze-dried to obtain a yellowish powder. The same procedure was repeated without the addition of CD precursors, and the resulting sample was named Lap. The citric acid concentrations were assorted by 10, 6, 2

and 1 times (weight/weight = w/w) of LAPONITE® mass, maintaining the 1:1 molar ratio between citric acid and ethylenediamine, identified as CDLP-A (0.5074 g citric acid and 168 µL ethylenediamine), CDLP-B (1.0214 g citric acid and 336 µL ethylenediamine), CDLP-C (2.9988 g citric acid and 504 µL ethylenediamine), and CDLP-D (5.0049 g citric acid and 1690 µL ethylenediamine), respectively.

2.2.4. Characterization Techniques

CD and hybrid structures samples were characterized by Powder X-ray diffraction (PXRD), Fourier transformed infrared (FTIR), and X-ray photoelectron spectroscopy (XPS). Optical microscopy, field emission gun–scanning electron microscope (FEG-SEM), scanning electron microscope (SEM) coupled with Energy-dispersive X-ray (EDX) spectrometer and scanning transmission electron microscope (STEM) were used for the morphology characterization. The optical characterization was performed by absorption, in the ultraviolet (UV) and visible (Vis) spectral regions, and photoluminescence spectroscopy. The samples also were characterized by elemental analysis (CHN) and thermogravimetric analysis (TGA)

PXRD was performed using a diffractometer / Rigaku SmartLab SE operating at 40 kV and 20 mA. Scans were performed in the 2θ range between 4.00° and 70.00° with a scan step of 0.02° and a Cu-Kα radiation source (1.54186 Å). The samples were placed in the cavity of the glass sample holder (plate, 25 mm in diameter, and 1 mm deep).

The FTIR analyses were performed using the NICOLET IS5 instrument, equipped with the iD1 Transmission module from Thermo Scientific. The spectra were obtained by scanning in the range of 4,000-410 cm^{-1}, with a background of 32 scans. The sample analysis was conducted with 32 scans and a resolution of 2 cm^{-1}. To prepare the samples for Merck spectroscopy, they were diluted in KBr and pressed into pellets for 1 minute under a pressure of 5 tons.

The chemical surface analysis for the CD, CDLP-A, CDLP-D and Lap samples was performed by XPS using a conventional XPS spectrometer ScientaOmicron ESCA+ with a high-performance hemispheric analyzer (EAC2000) with monochromatic Al Kα (hν = 1486.6 eV) radiation as the excitation source. During the analysis, the operating pressure in the ultra- high vacuum chamber (UHV) was around 10 − 9 Pa. The XPS high-resolution spectra were recorded at a constant pass energy of 20 eV with a 0.05 eV per step. A charge neutralizer (CN10) was used to exclude the surface charging effects. The obtained spectra

were corrected assuming 284.8 eV for adventitious carbon and the analysis of the XPS spectra was realized by using the CASA XPS software.

Optical microscopy images were collected by a digital microscope Leica DFC310 FX for fast acquisition of fluorescence images equipped with a mercury-vapor HBO 50 W lamp (ebq 50 ac) a UV excitation filter (340 - 380 nm) and a suppression filter at 425 nm.

The FEG-SEM images were obtained in a FEG-SEM JSM6701F / JEOL microscope at 2 kV. The samples were suspended in ultrapure water and drop-casted as thin layers on single-crystal silicon substrates.

The STEM images were acquired with a STEM Hitachi HD2700 microscope using high-resolution and dark-field Z contrast mode, with an acceleration voltage of 200 kV. The samples were suspended in ethanol and drop-casted on C400Cu100 carbon film grid.

The EDX-mapping was obtained using an SEM- JEOL microscope, model JSM 6510) equipped with an EDX spectrometer (NSS Thermo Scientific). The samples were dispersed on a aluminum plate affixed to the surface of a metallic disk (stub) and analyzed.

CHN were acquired using a PerkinElmer CHNS/O 2400 Series II combustion analyzer.

TGA (TGA-Q500/TA Instruments, United States) was performed with 8.0 mg of sample heated from 30 to 700 °C at 10 °C min^{-1} using N_2 flux of 60.0 mL min^{-1}.

The room temperature photoluminescence spectra were carried out on a Horiba-Jobin Yvon Fluorolog - 3 FL3 - 22 spectrofluorometer equipped with a Hamamatsu R928P photomultiplier. A continuous xenon lamp FL-1039A/40A 450 W was used for the excitation and the emission spectra. The low-temperature photoluminescence was performed in the same instrument using a helium-closed cycle cryostat coupled to a vacuum system (4 x 10^{-4} Pa) and an autotuning temperature controller (Lakeshore 331, Lakeshore). The temperature was measured with a silicon diode cryogenic sensor (DT-470-SD, Lakeshore) with an accuracy of ± 0.5 K (12 – 30 K). For the photoluminescence decay a pulsed diode light source NanoLED-390 (Horiba-Jobin Yvon) with a wavelength of 388 nm and pulse duration of 1.2 ns was employed.

The photoluminescence quantum yield (ϕ) values were determined at 298 K using a system (C9920-02, Hamamatsu). consisted of a 150 W xenon lamp coupled to a monochromator for precise wavelength discrimination. An integrating sphere was employed as the sample chamber, and a multichannel analyzer was used for signal detection. The measurement method exhibited high accuracy, with a precision of up to 10%.

2.3. Results and Discussion

2.3.1. Structural characterization

The PXRD technique is a valuable tool for confirming the hybrid formation by analyzing the diffraction patterns of the LAPONITE®, with the (001) plane at $2\theta = 6.92°$ serving as a reference. This is because the (001) plane reflects the interlayer spacing (*d*), which increases upon the interaction with molecules or nanoparticles.[28] As can be seen in Figure 2.1a, all samples exhibit a shift of the (001) peak towards lower angles compared to Lap, which has an interlayer spacing (*d*) of 12.69 ± 0.07 Å as calculated using Bragg's Law. Peraro *et al.*[29] found a value of *d* = 12.87 Å as well as Li *et al.*[30] and Papagiannopoulos *et al.*[31] with a value of *d* = 12.8 Å in both cases. As can be seen in the data presented in Table 2.S1, all synthesized hybrids showed higher *d* values, including CDLP-A with *d* = 13.08 ± 0.08 Å, and CDLP-D with *d* = 13.24 ± 0.08 Å (Figure 2.1b), used as representative models for subsequent studies. According to the results, CDs formation perturbs the interlayer spacing of LAPONITE®, while maintaining structural integrity, even at high precursor concentrations. This is supported by the similarity with the pristine LAPONITE®'s (Figure 2.S1) crystalline peaks at 19.56°, 28.12°, 35.08°, 53.46° and 60.88° ((100), (005), (110), (211) and (300) attributed according to PDF-9-31 of Hectorite-16A), also in agreement with Daniel *et al.*[32].

Yang et al. [26] observed a significant enhancement of interlayer spacing (d) upon CDs synthesized *in situ* with LAPONITE® by solvothermal method. However, in the case of the hydrothermal method, as presented herein, the low shift of the $2\theta = 6.92°$ in the hybrid samples indicated that the formation of CDs hardly occurs on interlayer spacing.

$$\begin{aligned} &Na_{0.7}Si_8Mg_{5.5}Li_{0.3}O_{20}(OH)_{4(s)} + 12\ H^+_{(aq)} + 8\ H_2O_{(l)} \rightarrow \\ &0.7\ Na^+_{(aq)} + 8\ Si(OH)_{4(s)} + 5.5\ Mg^{2+}_{(aq)} + 0.3\ Li^+_{(aq)} \end{aligned} \quad (2.1)$$

The literature highlights the chemical stability of LAPONITE®, which is dependent on factors such as the pH of the medium, LAPONITE® and Na^+ concentrations.[33–35] It

has been reported that partial dissolution of the clay mineral occurs when the pH falls below 10, as indicated by the chemical reaction below (Equation 2.1).[33]

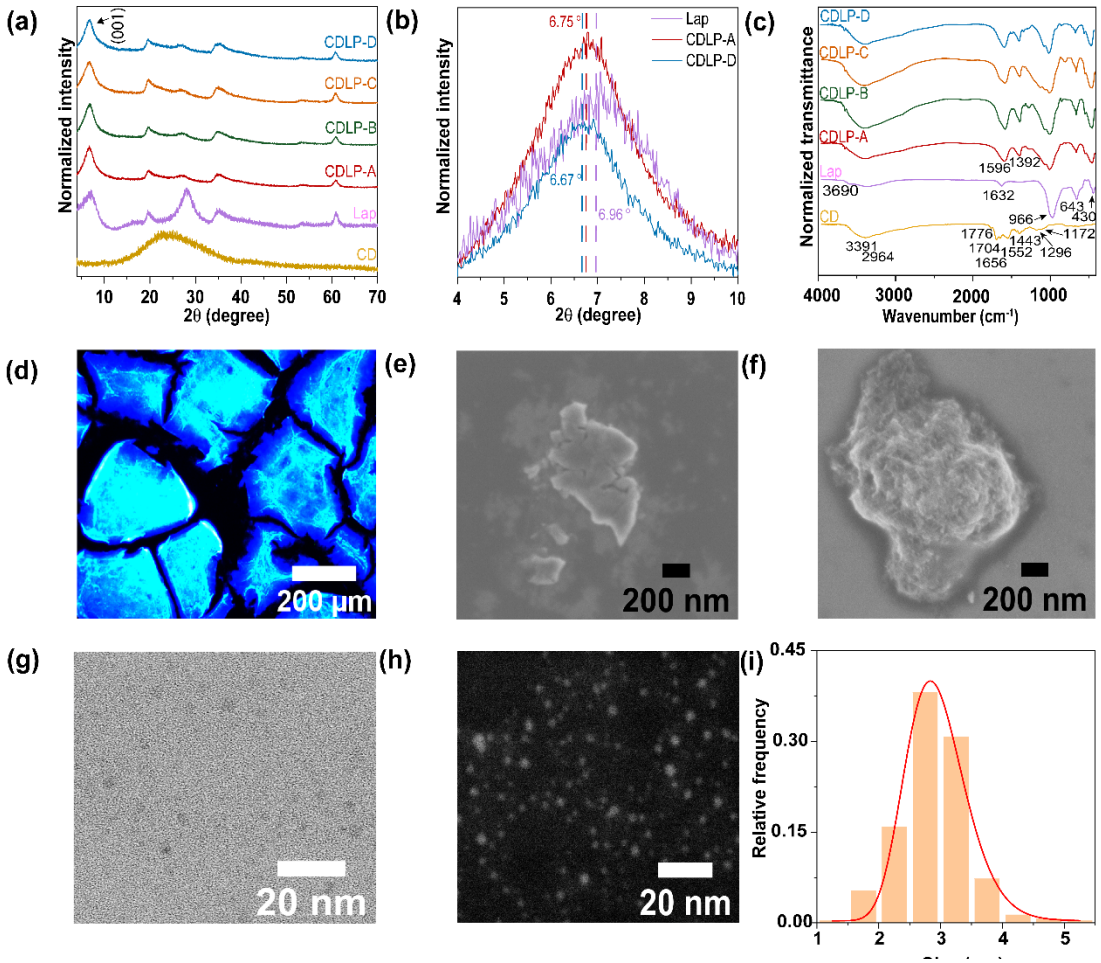

Figure 2. 1. PXRD patterns of CDLP samples, Lap and CD (a) and comparison of (001) plane reflection of Lap, CDLP-A and CDLP-D (b); FTIR spectrum in the region of 4000 to 410 cm−1 of Lap, CD and hybrids CDLP samples (c); Microscopic image of CDLP-A water suspension captured with an Optical microscope equipped with UV excitation filter (340-380 nm) and a suppression filter at 425 nm (d); FEG-SEM images of Lap and CDLP-A water suspension (e) and (f) respectively; STEM images of in high-resolution mode CDLP-A (g) and dark-field Z contrast mode (h) with size distribution in (i); the solid represents a log-normal best fit.

Thomson and Butterworth [33] observed no release of Mg^{2+} and silicates at pH 10 in concentrations of 10.0 $g{\cdot}L^{-1}$, confirming its stability under these conditions. However, Jatav and Joshi [34] noted the presence of Mg^{2+} in the medium, even at pH levels above 10, when using 1% (w/w) LAPONITE®, emphasizing the role of Na^{+} concentration in preventing LAPONITE® dissolution, particularly at a concentration of 7.2 mM NaCl. Pilavtepe *et al.*[35] described that LAPONITE® dissolution occurs when the pH falls below 8.5. In the case of hybrid synthesis, it is important to consider the pH of the pre-synthesis in the synthesis of CDLP to avoid the dissolution of LAPONITE® due to the low pH (~5.0) of the CD precursors after solubilization. When the pH is not adjusted, the high

concentration of H^+ from citric acid triggers the dissolution of LAPONITE® and it leads to structural collapse of the lamellar pattern, as evidenced by the PXRD pattern in Figure 2.S1. On the contrary, with pH adjustment to 8.5, the formation of a gel with characteristic "edge-edge" or "face-face" interactions[35] of LAPONITE® was observed with structural integrity, as observed by PXRD results.

FTIR was employed on the powder samples to investigate the functional groups formed in the synthesized hybrids and CD. The spectra of the hybrids display bands associated with LAPONITE®, as illustrated in Figure 2.1c. This observation reinforces the PXRD results, indicating the absence of structural collapse. In addition, the concentration did not influence the formation of functional groups. The main bands are displayed in Table 2.S2 with their respective assignments. Compared with CD, the coincident vibration bands in the hybrid samples appear as shoulders at 1,704 cm^{-1} corresponding to ν(C=O) stretching of amide[36,37]; at 1,552 cm^{-1}, indicative of ν(C=C) stretching;[36,37] at 1,443 cm^{-1}, associated with δ(CH) angular deformation[36,37]; at 1,296 cm^{-1}, related to δ(COH) angular deformation[36,37]; and at 1,177 cm^{-1}, corresponding to ν(C–O) stretching[36,37]. Bands at 1,776 and 1,656 cm^{-1} also appear in the CD FTIR spectrum, corresponding to the ν(C=O) stretching of carbonyl and angular deformation of amide δ(NH), respectively.[36,37] In the hybrid samples, prominent vibrations of asymmetric and symmetric carboxylates[38–40] are observed at 1,596 cm^{-1} and 1,392 cm^{-1}, respectively, favored by the deprotonation of citric acid. Furthermore, there is a shift to higher wavenumbers of the ν(Si–O–Si) band at 966 cm^{-1}, as well as the δ(MgO) and 430 cm^{-1} bands at 1,004 cm^{-1} and 450 cm^{-1}, respectively, in the hybrid samples, which may be attributed to stress in the crystalline lattice or hydrogen bonding interactions with carboxylic acid groups of the CDs.

Microscopic images of CDLP-A sample water suspension were captured, as shown in Figure 2.1d, revealing the organization of LAPONITE® aggregates in the form of flakes and the blue emission from CDs formed underneath the clay mineral, indicating successful hybrid formation. FEG-SEM images show that CDLP-A has a rough surface (Figure 2.1f) compared to smooth-surfaced Lap (Figure 2.1e) with well-defined edges and a contour around the hybrid, suggesting the deposition of CDs aggregates on the clay mineral's edges or clustered around the clay mineral. By EDX mapping, it is possible to verify the carbon from CDs around and over the surface of LAPONITE® aggregates (identified as mainly by Si and Mg content) in CDLP-A and CDLP-D samples by the contrast with the aluminum substrate (Figure 2.S3). Since the synthesis pH was adjusted

to 8.5, deprotonated carboxylate species from citric acid would predominate in the reaction medium, favoring interactions with MgOH groups on the LAPONITE®'s edge, which is positively charged at 8.5 pH. Therefore, it is possible that the formation of CDs occurred between the edges of LAPONITE®. The CDs formed in CDLP-A are amorphous and have an average size of 3.0 ± 0.5 nm, as shown in STEM images in Figures 2.1g and 1h. For the CDLP-D sample, the CDs have an average size of 2.8 ± 0.5 nm and exhibit an amorphous characteristic (Figure 2.S2a). In comparison to the CD sample with an average size of 15.8 ± 2.3 nm (Figure 2.S2d), the CDs formed underneath LAPONITE® exhibited a much smaller average size, indicating that the nanoscale clay mineral can serve as nanoplatforms for CDs.

The samples were subjected to XPS analysis to evaluate the functional groups on the surface of the hybrids, as shown in Figure 2.2. The XPS survey spectra, shown in Figure 2.2a, display clear signals of C 1s at 285 eV, N 1s at 400 eV, and O 1s at 531 eV in the CDLP-A and CDLP-D samples, as well as Si 2p at 102 eV and Mg 2p at 50 eV,[41] originating from LAPONITE®. The atomic percentages shown in Table 2.1 for C were consistent with the increased concentration of citric acid; however, fewer functional groups containing N are formed in CDLP-D compared to CDLP-A (3%) and CD (8%). It was also possible to investigate the chemical environment of each element by the adjusted components, and since the component profiles were similar for both samples (Figures 2. 2b–2f) only the CDLP-A sample is presented. For C 1s (Figure 2.2d), the energies were associated with the C–C sp^2 bond/C-H sp^3 bond, with the lowest energy of 284.8 eV, followed by nitrogenated C–N and oxygenated groups C=O, N–C=O in 286.2 and 288.1 eV respectively, as well as acetate moiety O–C=O in 289.1 eV.[41] Figure 2.2b reveals the components adjusted to the O 1s, attributed to O bonded to Mg and Si at 531.8 eV and O–C at 532.8 eV.[41] The deconvoluted nitrogen N 1s spectrum into two components (Figure 2. 2c) revealed N–(C=O)– bonds at 399.7 eV and protonated amines at 401.6 eV.[41]

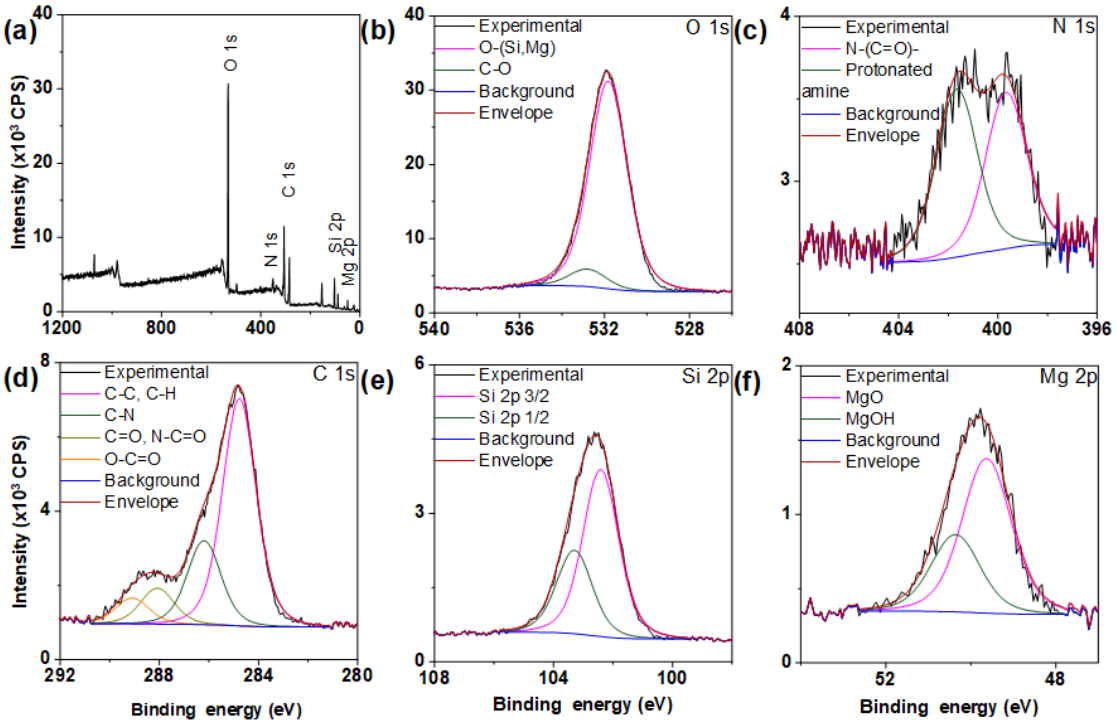

Figure 2.2. XPS survey spectrum of CDLP-A (a); high-resolution XPS spectrum of O 1s (b), N 1s (c), C 1s (d), Si 2p (e) and Mg 2p (f) of CDLP-A sample.

Based on the PXRD results, the samples synthesized at pH = 8.5 remained stable after the hybrids *in situ* synthesis. In addition, according to the PXRD results and microscopy imagens, the CDs could be deposited beneath the surface of the edges of LAPONITE® layers or clustered around the clay mineral. Although, based on these results, it is difficult to distinguish whether the CDs is deposited at the edges, clustered around the clay mineral or even concentrated on one side. The structure of the CDs synthesized under LAPONITE® exhibited distinct features compared to the CD sample, with carboxylate groups being predominant and interacting through hydrogen bonding with the tetrahedra of Si and octahedra of Mg in LAPONITE® observed by FTIR shifting. According to Yang *et al.*,[42] the presence of $Mg(OH)_2$ groups can protect the carboxyl groups during the CDs synthesis through chelation, which is supported by our FTIR and XPS results, showing that this moiety remains on the surface of the CDs. Thus, because of this interaction with the LAPONITE® edge's, composed with magnesium coordinated octahedrally to oxygen and hydroxyl groups, and the carboxylate groups from CDs formed, we speculate based on the microscopy images, PXRD and the FTIR shifting, that the CDs are preferentially deposited at the edge of LAPONITE®. Furthermore, in the synthesis of the CDLP hybrid, nitrogenated groups were formed in smaller quantities on the surface than CD. The reason for this occurrence is not entirely clear, but a possible explanation is that at

pH 5.0, under the pre-synthesis conditions of CD, both amines are deprotonated,[43] facilitating the reaction with citric acid carboxylates to form CDs. However, at pH 8.5, only one amine remains deprotonated,[43] and it can exchange with Na^+ to stabilize the interlamellar charges,[44] while the carboxylate groups stabilize the edges, hindering the formation of nitrogenated groups on the surface of the hybrid.

Table 2.1 - Surface composition of CDLP-A, CDLP-D, Lap and CD samples obtained from high-resolution XPS spectrum in atomic percentage. High-resolution spectrum within ±5% of uncertainty.

Samples	%O 1s	%C 1s	%N 1s	%Si 2p	%Mg 2p	%Na 1s
CDLP-A	37	30	3	18	11	1
CDLP-D	35	50	1	5	4	5
Lap	30	27	0	19	13	0
CD	19	70	8	2	0	0

2.3.2. Photoluminescence Properties

The presence of LAPONITE® in the synthesized hybrids induced structural changes and influenced their optical properties. Optical characterizations, including UV-visible absorption and photoluminescence, were conducted to investigate luminescence processes and establish the emission mechanism. The absorption measurements in UV-visible range using 1.0 $mg{\cdot}mL^{-1}$ water suspension of the samples, revealed absorption bands centered at 243, 338, and 450 nm, corresponding to the $\pi \rightarrow \pi^*$ electronic transition of C=C groups in the core and $n \rightarrow \pi^*$ C=O and C=N groups on the surface respectively (Figure 2.S7).[14,45,46] However, the absorption band at 450 nm was not observed in the hybrids, likely due to the low content of nitrogen groups as confirmed by XPS analysis.

The CD samples demonstrated visible photoluminescence emission in water (Figure 2.S8) suspension but experienced self-quenching in solid-state powder form ($\phi_{360} < 0.01\%$), a common occurrence in carbon nanoparticles attributed to π-π stacking.[16,47,48] In contrast, the CDLP hybrids exhibited visible photoluminescence emission in both aqueous suspension and powder form, with incomplete quenching observed in the latter, as evidenced by quantum yield measurements displayed in Table 2. Additionally, it was possible to observe qualitatively the samples' emission when irradiated with UV lamp of 365 nm (Figure 2.S11). In solid-state form, both CDLP hybrids exhibited a red shift of 444 nm band to 450 nm compared to the suspension (Figures 2.3a and 3c) and underwent

quenching in the powder form, as suggested by the decrease of ϕ_{360} value presented in Table 2.2. This quenching phenomenon can be tentatively attributed to a strong non-radiative channel in the solid state, as evidenced by the decrease in lifetime monitored at 450 nm emission at 298 K (τ_{450}^{298}). Furthermore, the band centered at 517 nm, which becomes more prominent with the quenching of the 450 nm emission, undergoes a red shift with increasing excitation wavelength, suggesting a wavelength-dependent emission behavior in both samples. Wavelength-dependent excitation is typically associated with the presence of different sizes of CDs,[8–11] surface states introduced by various functional groups,[9–12] the amount of oxygen in the core,[10,11,13] and luminescent by-products on the surface.[10,11,14,15] On the other hand, the 444 nm band did not red shift in the water suspension with increasing excitation wavelength, indicating a wavelength-independent emission behavior.

Hence, it becomes evident that multiple emitter centers are contributing to the emission within the samples. Notably, one of these centers experiences quenching in the solid state, while another remains unaffected. This distinction is apparent when comparing the quantum yield values at 500 nm in suspension and solid samples (ϕ_{500} values in Table 2.2), which remain consistent with long-wavelength excitation in both samples. Structural and morphological characterization confirms that the CDs synthesized on LAPONITE® tend to form carboxylate groups and exhibit a homogeneous size distribution, promoting the emission of surface states associated with low energy levels corresponding to the unaffected bands. The higher energy states, associated with the quenched emission, can be ascribed to the $\pi \rightarrow \pi^*$ transition within the carbon dot core (intrinsic states – IS) or to fluorophores, such as citric acid derivatives like IPCA (5-oxo-1,2,3,5-tetrahydroimidazo[1,2-a]pyridine-7-carboxylic), present on the surface.[49–51] This hypothesis gets support from the observed emission decay when monitoring the emission at 450 nm (Figures 2.3b and 3d), which follows well-fitted curves under a monoexponential model.

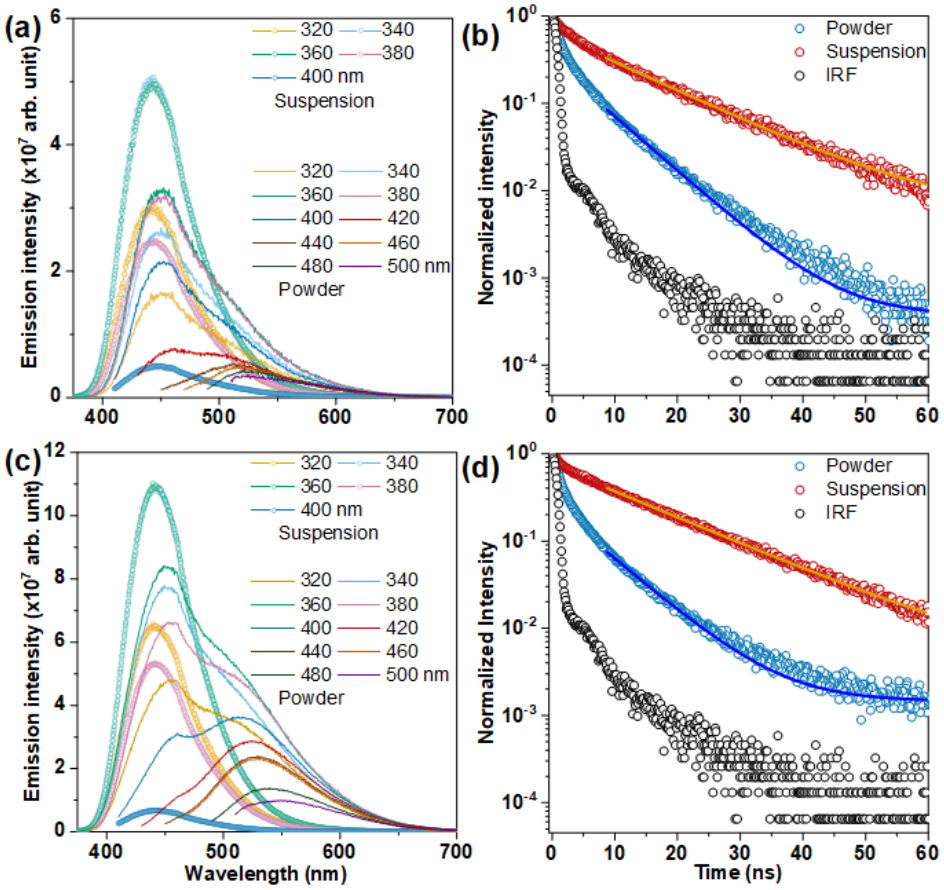

Figure 2.3. Room temperature photoluminescence emission spectra of CDLP-A (a) and CDLP-D (c) in both powder and water suspension. Emission decay for CDLP-A (b) and CDLP-D (d) samples in powder (blue) and suspension (red), using a 388 nm nanoLED for excitation and monitoring emission at 450 nm. IRF is the instrumental response function.

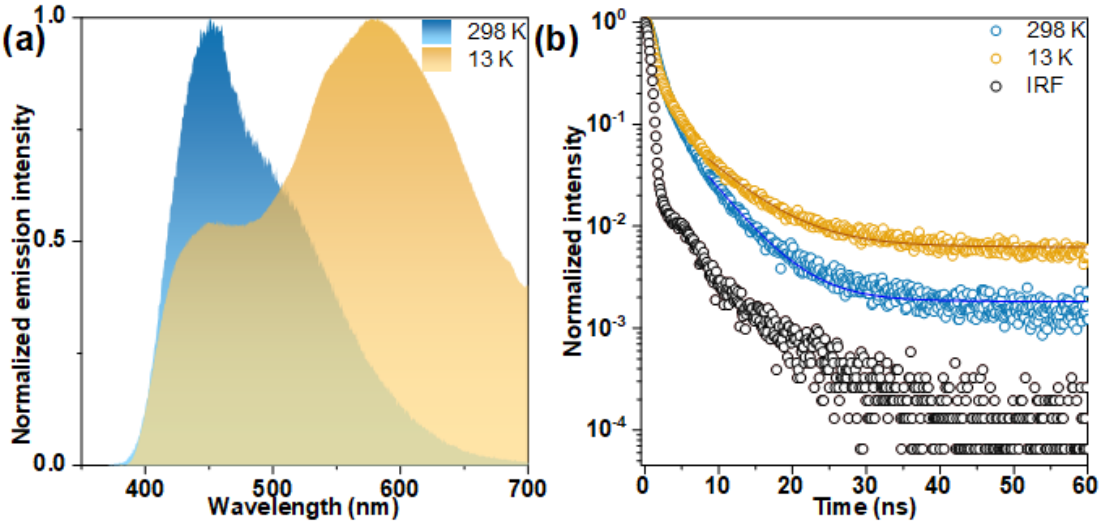

Figure 2.4. (a) Comparison of the room and low temperature emission spectra of CDLP-D (excited at 360 nm). (b); Room and low temperature decay curves of CDLP-D monitored at 575 nm and excited at 388 nm using a nano-LED. IRF is the instrumental response function.

A more thorough investigation was carried out using low-temperature photoluminescence measurements, as the non-radiative deactivation processes could be minimized, allowing for the examination of radiative contributions. The low temperature (13 K) emission spectrum presented in Figure 2.4a and Figure 2.S12 reveals a relative enhancement of the emission band centered at 575 nm in both samples, with a relative intensity ratio of I_{575}/I_{450} = 0.4 and 1.9 for CDLP-A and CDLP-D, respectively. This enhancement is much lower at room temperature, with intensity ratios of I_{575}/I_{450} = 0.1 and 0.2 for CDLP-A and CDLP-D, respectively.

Given that the main difference between samples lies in the precursor concentrations (citric acid and ethylenediamine) and that CDLP-D exhibits a higher amount of C according to XPS analysis, it is expected that a higher concentration of CDs forms on the LAPONITE® surface, potentially leading to aggregation. Although is difficult to estimate the amount of CDs on the hybrids, in addition to XPS analysis, elemental analysis CHN resulted in a 9.0% (±0.2) of carbon for CDLP-D and 8.0% (±0.2) for CDLP-A. The nitrogen value also was superior as can be seen in Table 2.S3. As demonstrated by Chang *et al.*,[52] , the content of CDs can be indirectly estimate by CDs decomposition obtained by the weight loss of the decomposition event of CDs framework, between 280 °C and 330 °C. The samples presented the weight loss of 88% for CDLP-D and 75% for CDLP-A (Figure 2.S19), indicating the higher amount of CDs in CDLP-D sample. This concept is in line with the findings of Chang *et al.*,[52] where the aggregation-induced emission (AIE) phenomenon in a hybrid consisting of carbon nanoflakes and carbon dots was reported. This AIE was attributed to Förster resonance energy transfer (FRET) occurring between CDs, with less-aggregated CDs in suspension showing emission primarily around 450 nm. Chen *et al.* also observed the AIE phenomenon [47] where CDs with long PVA chains were synthesized, preventing self-quenching in the solid state and attributing the red-shifted emission energy transfer processes.

In the next section, we will develop a model to estimate the average distance between CDs aggregates based on a Förster-Dexter-type energy transfer process between them, building upon the insights gained from the AIE phenomena.

Table 2.2 - Lifetime (τ) and quantum yield ($\phi_{\lambda exc}$) of CDLP-A and CDLP-D suspension and powder obtained by fitting the room (298 K) and low (13 K) temperature emission decay curves excited at 388 nm and recorded at 450 and 575 nm. The model used was $y = y_0 + \sum_n A_n \exp(-(t_n - x_0)/\tau_n)$, where *y* is the PL intensity, y_0 is a constant, A_n the amplitude of the *n* component of the decay, t_n is the experimental decay data, and x_0 = 8.7 ns is obtained by the instrument response function. The best fitting was achieved by applying one component (Figure 2. S14 and S15).

	CDLP-A		
	$\boldsymbol{\tau_{450}^{298}}$ (ns)		
Suspension	13.0±0.1		
Powder	6.9±0.1		
	$\boldsymbol{\phi_{360}}$	$\boldsymbol{\phi_{400}}$	$\boldsymbol{\phi_{500}}$
Suspension	0.26±0.03	0.09±0.01	0.06±0.01
Powder	0.09±0.01	0.07±0.01	0.06±0.01
	CDLP-D		
	$\boldsymbol{\tau_{450}^{298}}$ (ns)	$\boldsymbol{\tau_{575}^{298}}$ (ns)	$\boldsymbol{\tau_{575}^{13}}$ (ns)
Suspension	14.4±0.1	-	-
Powder	7.1±0.1	4.8 ± 0.1	6.2±0.1
	$\boldsymbol{\phi_{360}}$	$\boldsymbol{\phi_{400}}$	$\boldsymbol{\phi_{500}}$
Suspension	0.22±0.02	0.04±0.01	0.01±0.01
Powder	0.02±0.01	0.02±0.01	0.02±0.01

2.3.3. Energy Transfer Between CDs Aggregates

Zhou *et al.*[53] examined how the aggregation effect of CDs may induce surface states that can interact with the intrinsic electronic states of the CDs (when they are not aggregated), potentially leading to different energy recombination processes. In our case, these processes can be illustrated in a Jablonski-type energy level diagram (Figure 2.5b) for the CDLP-D, where the coupled surface states (CSS), red-shifted, originate from the presence of inhomogeneous surface-confined charges [54] in CDs clusters. As assigned in the last section, the IS corresponds to the band with a maximum at 450 nm, and the emerging band at 575 nm to the CSS (Figures 2.4a and 5b).

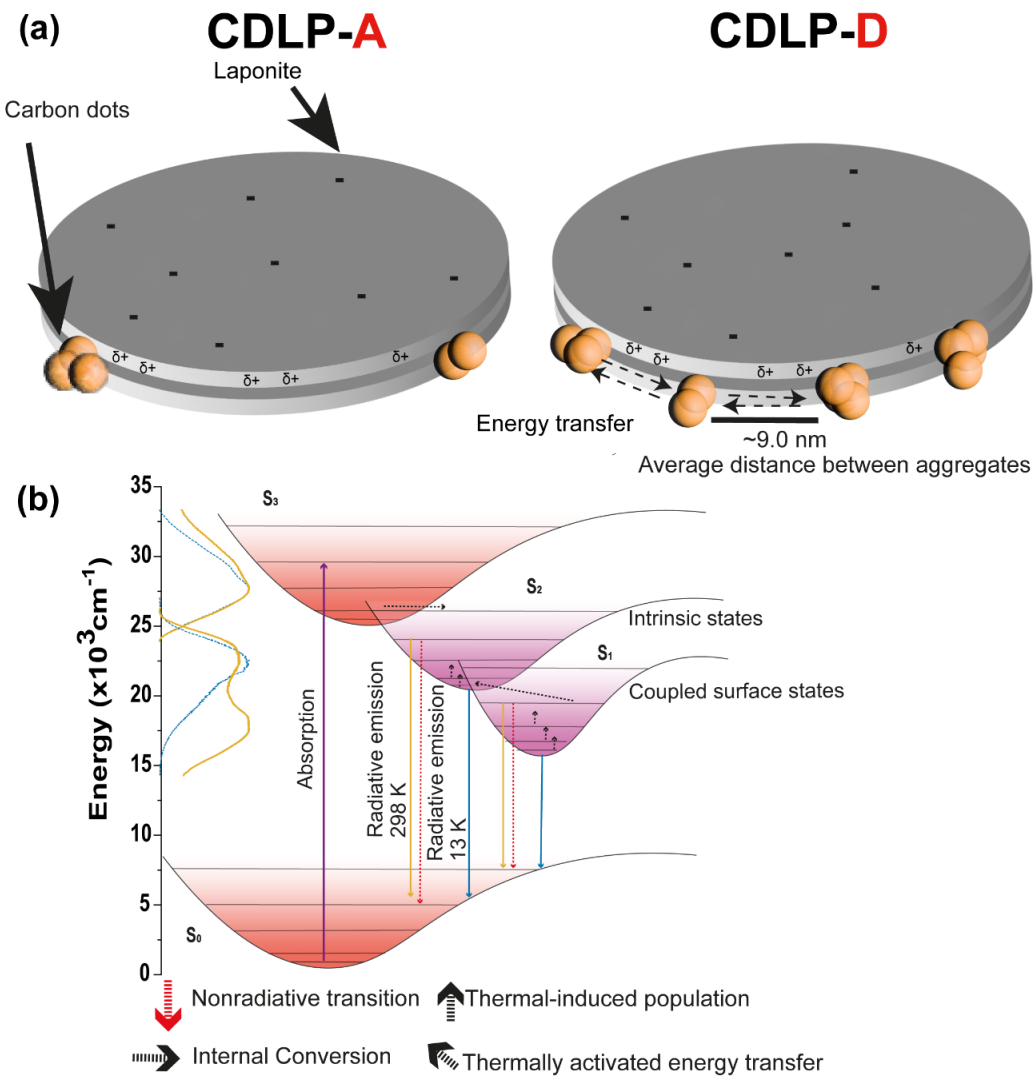

Figure 2.5. (a) Schematic representation of energy transfer process between CDs aggregates on Laponite and (b) Jablonski-type energy diagram proposed using the room temperature and low-temperature photoluminescence spectra of powder CDLP-D.

A comparison of lifetime measurements at 13 and 298 K for the CSS band suggests the possibility of a thermally activated non-radiative CSS-to-IS energy transfer channel. This inference is supported by the significant decrease in lifetime, from 6.2 ± 0.1 to 4.8 ± 0.1 ns (Figure 2.4b), and the disappearance of the CSS emission at room temperature (Figure 2.4a). Thus, this observation indicates that part of the energy in the CSS is dissipated to the surrounding medium and may be absorbed by the IS of a neighboring CDs aggregation. The IS band also undergo to a decrease in lifetime, from 10.0 ± 0.1 to 7.0 ± 0.1 ns (Figure 2.S13). This can be related to thermal quenching. In addition, the significant decrease of I_{575}/I_{450} at room temperature, indicate that the IS band remains relatively stable with temperature, suggesting that it is being populated to compensate for other quenching processes, such as internal conversion and intersystem crossing. Thus,

the IS serves as an acceptor state in the energy transfer process between CD aggregates while the CSS is a donor, which should raise its high Franck-Condor states to start being in resonance condition to transfer energy (Figure 2.5b). Thus, once the lifetimes at 13 K minimize non-radiative losses, including energy transfer, the energy transfer rate can be estimated using the following equation:

$$W \approx \frac{1}{\tau_{575}^{298}} - \frac{1}{\tau_{575}^{13}} \tag{2.2}$$

where τ_{575}^{298} = 4.8 ns and τ_{575}^{13} = 6.2 ns, as measured from the decay curves in Figure 2.4b and presented in Table 2.2. The energy transfer rate obtained ($W = 4.7 \times 10^7$ s^{-1}) is consistent with energy transfer rates between spin-allowed transitions from the donor and acceptor for longer distances.[55–58] For example, Wollny *et al.*[55] estimated an FRET rate of around 7.5×10^{11} s^{-1} in 4,4-difluoro-4-bora-3a,4a-diaza-s-indacene (donor) and pentacene (acceptor) dimers with an FRET distance of around 1.3 nm. If this distance is increased by a factor of 5 (6.5 nm), the FRET rate decreases by a factor of $(1/5)^6$, to the order of 5.0×10^7 s^{-1}, which agrees with the value obtained from Equation 2.2.

Equation 2.2 assumes that the structure and composition remain constant for both temperatures, and the difference in the rate is attributed to the rate at which the donor loses energy to the acceptor. This formulation is equivalent to the case of energy transfer between lanthanide ions, where the lifetimes of the donor are measured in the absence and presence of the acceptor, and the differences between rates is attributed to non-radiative energy transfer.[59–61]

Alternatively, once the transitions are spin-allowed the energy transfer rate due to the dipole-dipole mechanism (W_{d-d}) can be given by a Förster–Dexter expression:[62]

$$W_{d-d} = \frac{2\pi}{\hbar}\frac{S_D S_A}{G_D G_A R^6} F \tag{2.3}$$

where $\hbar$ is the reduced Planck's constant, S_D and S_A are the dipole strength of the donor and acceptor transitions while G_D and G_A are its respective degeneracies. From the short lifetimes they present, it is reasonable to assume that both transitions (centered at 450 and

575 nm) have a singlet-like character, thus, $G_D = G_A = 1$. R is the donor-acceptor distance.

The F factor was initially developed to determine the contributions of the density of states in the energy transfer process between molecules and metallic nanoparticles.[63] Later, it was refined to include considerations of vibrational state overlaps and temperature effects through a Boltzmann distribution for initial and final electronic states.[64,65] The F can be estimated through:[62,66]

$$F = \frac{\Upsilon}{(\gamma_D^2 + \gamma_A^2)^{1/2}} \times e^{-(\Delta/\gamma_D)^2 \Gamma} \tag{2.4}$$

where

$$\Gamma = \left[1 - \frac{1}{1 + (\gamma_D/\gamma_A)^2}\right] ln\, 2, \qquad \Upsilon = \left(\frac{ln\, 2}{\pi}\right)^{1/2} \frac{1}{c \cdot h} \tag{2.5}$$

with γ_{D} and γ_{A} being the bandwidths at half-height (in $\mathrm{cm^{-1}}$) of the donor and acceptor, respectively. c and h are the speed of the light and the Planck constant. Δ (in $\mathrm{cm^{-1}}$) being the energy difference (mismatch) between the donor and acceptor states, $\Delta = \sigma_{\mathrm{D}} - \sigma_{\mathrm{A}}$, and $\Upsilon = 2.3646184 \times 10^{15}\ \mathrm{cm^{-1} \cdot erg^{-1}}$.[66] This formulation considers the creation and annihilation of phonons when there is an energy mismatch between donor and acceptor states.[64]

Applying appropriate Jacobian transformations[67] to the data in Figure 2.4a and deconvoluting it into two bands, we can determine the barycenters of the donor (σ_D = 17,873 $\mathrm{cm^{-1}}$) and acceptor (σ_A = 23,112 $\mathrm{cm^{-1}}$) transitions in wavenumber units, along with their respective bandwidths at half-height (γ_D = 5,194 $\mathrm{cm^{-1}}$ and γ_A = 3,232 $\mathrm{cm^{-1}}$). This yields a value of $F = 1.597 \times 10^{12}\ \mathrm{erg^{-1}}$.

The dipole strengths for both donor (CSS) and acceptor (IS) transitions can be estimated from the observed lifetimes (τ) by:[62,68]

$$S = \frac{3\hbar}{32\pi^3\sigma^3\tau} \tag{2.6}$$

where σ (in $\mathrm{cm^{-1}}$) is the barycenter of the transition, as depicted in Figure 2.S17. In this way, Equation 3 can be rewritten as:

$$W_{d-d} = \frac{9\hbar}{512\pi^5} \frac{F}{\sigma_D^3 \sigma_A^3 \tau_D \tau_A R^6} \tag{2.7}$$

Once both transitions are spin-allowed (transitions from excited singlet states), the total energy transfer can be calculated as the sum of the dipole-dipole and exchange interactions, represented as $W = W_{d-d} + W_{ex}$. However, the exchange mechanism (W_{ex}) is proportional to the overlap between the electronic densities of the donor and acceptor,[69] which decay exponentially with the distance between donor and acceptor. Thus, it is expected that W_{ex} be negligible due to the large distances between CDs aggregates (> 1 nm). Therefore, the W_{d-d} mechanism dominates the energy transfer process between aggregates and can be orders of magnitude higher than the exchange mechanism. Consequently, the experimental rate obtained from Equation 2 can be compared with Equation 2.7, leading to the following relationship for the average distance between aggregates of CDs:

$$\bar{R} = \left[\frac{9\hbar}{512\pi^5 \cdot {\sigma_D}^3 \cdot {\sigma_A}^3} \left[\frac{\tau_D^{13}}{\tau_A^{298}(\tau_D^{13} - \tau_D^{298})} \right] F \right]^{\frac{1}{6}} \tag{2.8}$$

where the average distance $\bar{R}$ is given in units of cm.. As a result, when the values of σ_D = 18,867 cm^{-1}, σ_A = 23,135 cm^{-1}, F = 1.597×10^{12} erg^{-1}, and lifetime values in Table 2.2 (τ_A^{298} = 7.1×10^{-9} s, τ_D^{13} = 6.2×10^{-9} s, τ_D^{298} = 4.8×10^{-9} s) are applied, an average value of $\bar{R} \approx$ 9.6 nm is obtained for CDLP-D.

In very diluted systems with CDs, there is no energy transfer (W = 0) between aggregates because they are highly dispersed. This means that the donor lifetimes will not change due to the energy transfer process, and $\tau_D^{13} - \tau_D^{298}$ in Equation 8 tends to zero, indicating that the average distance between CDs aggregates tends toward infinity.

Based on Equations 2.7 and 2.8, the energy transfer rates as a function of the distance between aggregates can be estimated, as illustrated in Figure 2.S18. The model also provides a rough prediction of the limit for the shortest distance between them, which is around 7.4 nm. This distance makes sense since each CDs has a diameter of approximately ~2.8 nm, and an aggregate may have a diameter of around ~6 nm. This leaves a minimal space between the surfaces of different aggregates of around 1.4 nm. If the distance is shorter than this, two small aggregates may concatenate as one, which may occur when the concentration of CDs increases.

2.4. Conclusions

CDs were successfully synthesized *in situ* on LAPONITE® using the hydrothermal method, with pH control playing a crucial role in preserving the structural stability of LAPONITE®. Morphological analysis revealed the typical amorphous nature of the CDs deposited on edges of the LAPONITE®. Carboxylate groups were predominantly formed on the surface of the CDs, allowing for interactions with the Mg octahedra in the LAPONITE®. The photoluminescence emissions of the nanocomposite in aqueous suspensions and the solid-state exhibited a quenching effect on the 444 nm emission in the powdered samples, while the long-wavelength emission remained unaffected.

The low-temperature photoluminescence measurements suggest that the long-wavelength emission could result from radiative recombination of coupled surface states induced by aggregation, as evidenced by the enhancement of the 575 nm emission band with higher precursor concentration. However, at room temperature, thermally activated energy transfer occurs between these aggregates. To quantitatively assess this, an energy transfer model was introduced to estimate the average distance ($\bar{R}$) between CDs aggregates. The results showed that for the more concentrated sample (CDLP-D), $\bar{R} \approx 9.6$ nm. This model is based on the Förster-Dexter theory, with the dipole-dipole mechanism as the primary interaction.

The use of LAPONITE® was crucial to avoid the complete aggregation-induced quenching of carbon dots in the solid state. Future investigations to enhance the quantum yield values need to be performed to advance in the solid-state emission studies of carbon dots.

Author Contributions

Bruno S. D. Onishi: conceptualization, data curation, formal analysis, investigation, methodology, visualization, writing – original draft, and writing - review & editing. Albano N. Carneiro Neto: conceptualization, data curation, formal analysis, software, methodology, visualization, writing – original draft and writing -review & editing. Ricardo Bortolleto-Santos: formal analysis and writing -review & editing. Valmor R. Masterlaro: formal analysis and writing -review & editing. Luís D. Carlos: Funding acquisition, resources, supervision, validation and writing -review & editing. Rute A. S.

Ferreira: Funding acquisition, resources, supervision, validation and writing -review & editing. Sidney J. L. Ribeiro: Funding acquisition, resources, supervision, validation, project administration and writing -review & editing.

Conflicts of interest

There are no conflicts to declare.

Acknowledgements

This work was developed within the scope of the projects CICECO - Aveiro Institute of Materials, UIDB/50011/2020, UIDP/50011/2020, and LA/P/0006/2020, the Shape of Water (PTDC/NAN-PRO/3881/ 2020) financed by national funds through the FCT/MCTES (PIDDAC) and CAPES (Finance Code 001) provide the scholarship.

References

1 X. Xu, R. Ray, Y. Gu, H. J. Ploehn, L. Gearheart, K. Raker and W. A. Scrivens, *J. Am. Chem. Soc.*, 2004, **126**, 12736–12737.

2 Q. Zeng, T. Feng, S. Tao, S. Zhu and B. Yang, *Light Sci. Appl.*, 2021, **10**, 142.

3 S. Wang, W. Sun, D. S. Yang and F. Yang, *Beilstein J. Nanotechnol.*, 2020, **11**, 606–619.

4 N. K. Khairol Anuar, H. L. Tan, Y. P. Lim, M. S. So'aib and N. F. Abu Bakar, *Front. Energy Res.*, 2021, **9**, 1–22.

5 J. Ren, L. Malfatti and P. Innocenzi, *C*, 2020, **7**, 2.

6 C. He, P. Xu, X. Zhang and W. Long, *Carbon N. Y.*, 2022, **186**, 91–127.

7 F. Rigodanza, M. Burian, F. Arcudi, L. Đorđević, H. Amenitsch and M. Prato, *Nat. Commun.*, 2021, **12**, 2640.

8 H. Li, X. He, Z. Kang, H. Huang, Y. Liu, J. Liu, S. Lian, C. H. A. Tsang, X. Yang and S.-T. Lee, *Angew. Chemie Int. Ed.*, 2010, **49**, 4430–4434.

9 S. Zhu, Y. Song, X. Zhao, J. Shao, J. Zhang and B. Yang, *Nano Res.*, 2015, **8**, 355–381.

10 M. L. Liu, B. Bin Chen, C. M. Li and C. Z. Huang, *Green Chem.*, 2019, **21**, 449–471.

11 M. Langer, M. Paloncýová, M. Medveď, M. Pykal, D. Nachtigallová, B. Shi, A. J. A. Aquino, H. Lischka and M. Otyepka, *Appl. Mater. Today*, 2021, **22**, 100924.

12 L. Pan, S. Sun, A. Zhang, K. Jiang, L. Zhang, C. Dong, Q. Huang, A. Wu and H. Lin, *Adv. Mater.*, 2015, **27**, 7782–7787.

13 H. Ding, S. B. Yu, J. S. Wei and H. M. Xiong, *ACS Nano*, 2016, **10**, 484–491.

14 M. Otten, M. Hildebrandt, R. Kühnemuth and M. Karg, *Langmuir*, 2022, **38**, 6148–6157.

15 Y. Xiong, J. Schneider, E. V. Ushakova and A. L. Rogach, *Nano Today*, 2018, **23**, 124–139.

16 J. Wang, Y. Yang and X. Liu, *Mater. Adv.*, 2020, **1**, 3122–3142.

17 J. Ren, L. Stagi and P. Innocenzi, *Prog. Solid State Chem.*, 2021, **62**, 100295.

18 J. Li, Y. Wu and X. Gong, *Chem. Sci.*, 2023, **14**, 3705–3729.

19 Y. Zhai, F. Shen, X. Zhang, P. Jing, D. Li, X. Yang, D. Zhou, X. Xu and S. Qu, *J. Colloid Interface Sci.*, 2019, **554**, 344–352.

20 D. Zhou, Y. Zhai, S. Qu, D. Li, P. Jing, W. Ji, D. Shen and A. L. Rogach, *Small*, 2017, **13**, 1602055.

21 K. Suzuki, H. Miyamura and J. Balachandran, *J. Asian Ceram. Soc.*, 2021, **9**, 1473–1480.

22 S. Zong, B. Wang, X. Yin, W. Ma, J. Zhang and J. Li, *Nano Res.*, 2022, **15**, 9454–9460.

23 J. Uchida, Y. Takahashi, T. Katsurao and H. Sakabe, *RSC Adv.*, 2022, **12**, 8283–8289.

24 T. B. Becher, C. B. Braga, D. L. Bertuzzi, M. D. Ramos, A. Hassan, F. N. Crespilho and C. Ornelas, *Soft Matter*, 2019, **15**, 1278–1289.

25 L. Z. Zhao, C. H. Zhou, J. Wang, D. S. Tong, W. H. Yu and H. Wang, *Soft Matter*, 2015, **11**, 9229–9246.

26 J. Yang, Y. Liu, J. Wang, S. Wang, X. Zhou and H. Li, *J. Mater. Chem. C*, 2019, **7**, 7806–7811.

27 S. Zhu, Q. Meng, L. Wang, J. Zhang, Y. Song, H. Jin, K. Zhang, H. Sun, H. Wang and B. Yang, *Angew. Chemie*, 2013, **125**, 4045–4049.

28 V. R. R. Cunha, F. C. D. A. Lima, V. Y. Sakai, L. M. C. Véras, J. R. S. A. Leite, H. M. Petrilli and V. R. L. Constantino, *RSC Adv.*, 2017, **7**, 27290–27298.

29 G. R. Peraro, E. H. Donzelli, P. F. Oliveira, D. C. Tavares, C. H. Gomes Martins, E. F. Molina and E. H. de Faria, *Appl. Clay Sci.*, 2020, **195**, 105733.

30 J. Li, J. Cui, Z. Yang, H. Qiu, Z. Tang and J. Yang, *New Carbon Mater.*, 2018, **33**, 19–25.

31 A. Papagiannopoulos, S. P. Nikolakis, A. Pamvouxoglou and E. Koutsopoulou, *Int. J. Biol. Macromol.*, 2023, **225**, 565–573.

32 L. M. Daniel, R. L. Frost and H. Y. Zhu, *J. Colloid Interface Sci.*, 2008, **321**, 302–309.

33 D. W. Thompson and J. T. Butterworth, *J. Colloid Interface Sci.*, 1992, **15**, 236–243.

34 S. Jatav and Y. M. Joshi, *Appl. Clay Sci.*, 2014, **97**–**98**, 72–77.

35 M. Pilavtepe, S. M. Recktenwald, R. Schuhmann, K. Emmerich and N. Willenbacher, *J. Rheol. (N. Y. N. Y).*, 2018, **62**, 593–605.

36 D. L. Pavia, G. M. Lampman and G. S. Kriz, in *Introduction to spectroscopy*, Thomson Learning, 100 Barr Harbor Drive, PO Box C700, West Conshohocken, PA 19428-2959, 3th edn., 2009, pp. 13–101.

37 R. M. Silverstein, F. X. Webster and D. J. Kiemle, in *Spectrometric identification of organic compounds*, John Wiley & Sons, 7th edn.

38 M. Kakihana, T. Nagumo, M. Okamoto and H. Kakihana, *J. Phys. Chem.*, 1987, **91**, 6128–6136.

39 J. Zhang, F. Zhang, L. Ren, D. G. Evans and X. Duan, *Mater. Chem. Phys.*, 2004, **85**, 207–214.

40 L. I. Fockaert, T. Würger, R. Unbehau, B. Boelen, R. H. Meißner, S. V. Lamaka, M. L. Zheludkevich, H. Terryn and J. M. C. Mol, *Electrochim. Acta*, 2020, **345**, 136166.

41 J. F. Moulder, W. F. Stickle, P. E. Sobol and D. K. Bomben, *Handbook of X-Ray Photoelectron spectroscopy*, Perkin-Elmer Corporation, 1992.

42 X. Yang, S. Hou, T. Chu, J. Han, R. Li, Y. Guo, Y. Gong, H. Li and Z. Wan, *Ind. Crops Prod.*, 2021, **167**, 113507.

43 N. Cai and P. Larese-Casanova, *J. Environ. Chem. Eng.*, 2016, **4**, 2941–2951.

44 G. Lagaly, M. Ogawa and I. Dékány, in *Developments in Clay Science, vol. 1*, eds. F. Bergaya, B. K. G. Theng and G. Lagaly, Elsevier, Amsterdam, 2006, pp. 309–377.

45 P. Wu, W. Li, Q. Wu, Y. Liu and S. Liu, *RSC Adv.*, 2017, **7**, 44144–44153.

46 X. Chen, Z. Song, S. Li, N. Tat Thang, X. Gao, X. Gong and M. Guo, *Green Chem.*, 2020, **22**, 3296–3308.

47 Y. Chen, M. Zheng, Y. Xiao, H. Dong, H. Zhang, J. Zhuang, H. Hu, B. Lei and Y. Liu, *Adv. Mater.*, 2016, **28**, 312–318.

48 C. Kang, S. Tao, F. Yang and B. Yang, *Aggregate*, 2022, **3**, 1–18.

49 Y. Song, S. Zhu, S. Zhang, Y. Fu, L. Wang, X. Zhao and B. Yang, *J. Mater. Chem. C*, 2015, **3**, 5976–5984.

50 W. Kasprzyk, S. Bednarz, P. Żmudzki, M. Galica and D. Bogdał, *RSC Adv.*, 2015, **5**, 34795–34799.

51 W. Kasprzyk, T. Świergosz, P. P. Romańczyk, J. Feldmann and J. K. Stolarczyk, *Nanoscale*, 2022, **14**, 14368–14384.

52 Q. Chang, Y. Ding, S. Cheng, W. Shen, Z. Zhou, Y. Yin, T. Sun, C. Ban, Z. Deng, J. Liu, F. Xiu and W. Huang, *Nanoscale*, 2019, **11**, 2131–2137.

53 Z. Zhou, P. Tian, X. Liu, S. Mei, D. Zhou, D. Li, P. Jing, W. Zhang, R. Guo, S. Qu and A. L. Rogach, *Adv. Sci.*, 2018, **5**, 1800369.

54 D. Li, D. Han, S.-N. Qu, L. Liu, P.-T. Jing, D. Zhou, W.-Y. Ji, X.-Y. Wang, T.-F. Zhang and D.-Z. Shen, *Light Sci. Appl.*, 2016, **5**, e16120–e16120.

55 A. Wollny, G. Lavarda, I. Papadopoulos, I. López-Duarte, H. Gotfredsen, Y. Hou, R. R. Tykwinski, T. Torres and D. M. Guldi, *Adv. Opt. Mater.*, 2023, **11**, 2300500.

56 A. P. Litvin, E. V. Ushakova, P. S. Parfenov, A. V. Fedorov and A. V. Baranov, *J. Phys. Chem. C*, 2014, **118**, 6531–6535.

57 M. Corricelli, F. Enrichi, D. Altamura, L. De Caro, C. Giannini, A. Falqui, A. Agostiano, M. L. Curri and M. Striccoli, *J. Phys. Chem. C*, 2012, **116**, 6143–6152.

58 S. W. Clark, J. M. Harbold and F. W. Wise, *J. Phys. Chem. C*, 2007, **111**, 7302–7305.

59 R. Reisfeld and Y. Kalisky, *Chem. Phys. Lett.*, 1981, **80**, 178–183.

60 D. Jaque, O. Ramirez, E. Bausá, G. Solé, E. Cavalli, A. Speghini and M. Bettinelli, *Phys. Rev. B - Condens. Matter Mater. Phys.*, 2003, **68**, 1–9.

61 A. N. Carneiro Neto, R. T. Moura, A. Shyichuk, V. Paterlini, F. Piccinelli, M. Bettinelli and O. L. Malta, *J. Phys. Chem. C*, 2020, **10**, 10105–10116.

62 S. S. Nobre, P. P. Lima, L. Mafra, R. A. Sá Ferreira, R. O. Freire, L. Fu, U. Pischel, V. Z. De Bermudez, O. L. Malta and L. D. Carlos, *J. Phys. Chem. C*, 2007, **111**, 3275–3284.

63 O. L. Malta, *Phys. Lett. A*, 1986, **114**, 195–197.

64 A. N. Carneiro Neto, E. E. S. Teotonio, G. F. de Sá, H. F. Brito, J. Legendziewicz, L. D. Carlos, M. C. F. C. Felinto, P. Gawryszewska, R. T. Moura Jr., R. L. Longo, W. M. Faustino and O. L. Malta, in *Handbook on the Physics and Chemistry of Rare Earths, volume 56*, eds. J.-C. G. Bünzli and V. K. Pecharsky, Elsevier, 2019, pp. 55–162.

65 O. L. Malta, *J. Non. Cryst. Solids*, 2008, **354**, 4770–4776.

66 A. N. Carneiro Neto, R. T. Moura Jr., J. A. A. Coelho, M. E. Silva-Junior, J. L. Costa, O. L. Malta and R. L. Longo, *Chinese J. Lumin.*, 2022, **43**, 20.

67 J. Mooney and P. Kambhampati, *J. Phys. Chem. Lett.*, 2013, **4**, 3316–3318.

68 R. C. Hilborn, *Am. J. Phys.*, 1982, **50**, 982–986.

69 D. L. Dexter, *J. Chem. Phys.*, 1953, **21**, 836–850.

Supplementary material

Carbon Dots on LAPONITE® Hybrid Nanocomposites: Solid-state emission and Inter-aggregate Energy Transfer

Bruno S. D. Onishi,[1,2] Albano N. Carneiro Neto,[1] Ricardo Bortolleto-Santos,[3] Valmor R. Masterlaro,[4] Luís D. Carlos,[1] Rute A. S. Ferreira,[1,*] Sidney J. L. Ribeiro[2,*]

[1] Department of Physics and CICECO – Aveiro Institute of Materials, University of Aveiro, 3810-193 Aveiro, Portugal

[2] Institute of Chemistry, São Paulo State University─UNESP, São Paulo, Araraquara, 14800-060, Brazil

[3]Postgraduate Program in Environmental Technology, University of Ribeirão Preto─UNAERP, São Paulo, Ribeirão Preto, 14096-900, Brazil

[4]São Carlos Institute of Chemistry, University of São Paulo─USP, São Paulo, São Carlos, 13566-590, Brazil.

* Corresponding authors: rferreira@ua.pt (Rute A. S. Ferreira); sidney.jl.ribeiro@unesp.br (Sidney J. L. Ribeiro)

Table 2.S1 - Data of angle 2θ diffracted planes and interlayer distance (d) calculated by Bragg's Law.

Samples	2θ (degree)	d (Å)
CDLP-A	6.75	13.08 ± 0.08
CDLP-B	6.70	13.18 ± 0.08
CDLP-C	6.70	13.18 ± 0.08
CDLP-D	6.67	13.18 ± 0.08
Lap	6.96	12.69 ± 0.07
Pristine Laponite	6.92	12.76 ± 0.07

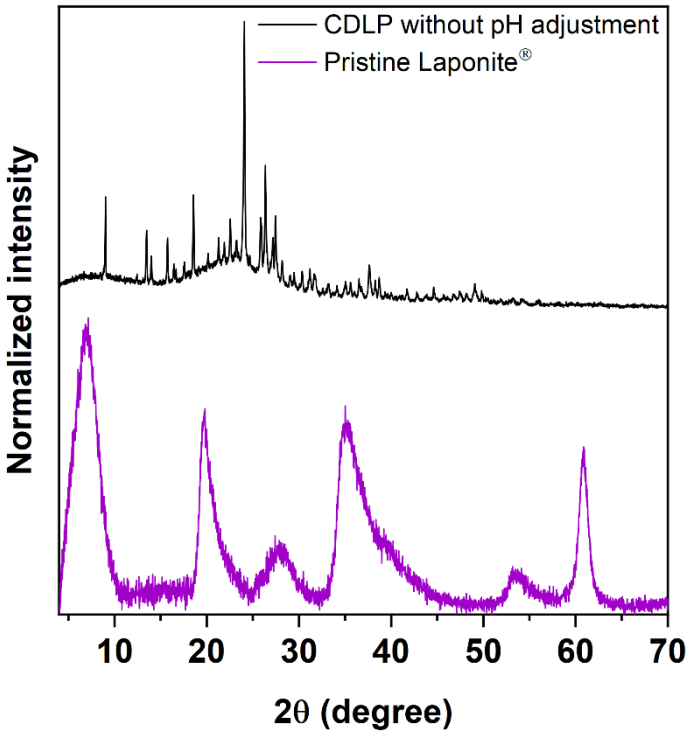

Figure 2.S1. Powder X-Ray Diffraction (PXRD) patterns of CDLP without pH adjustment (pH = 5) and pristine Laponite.

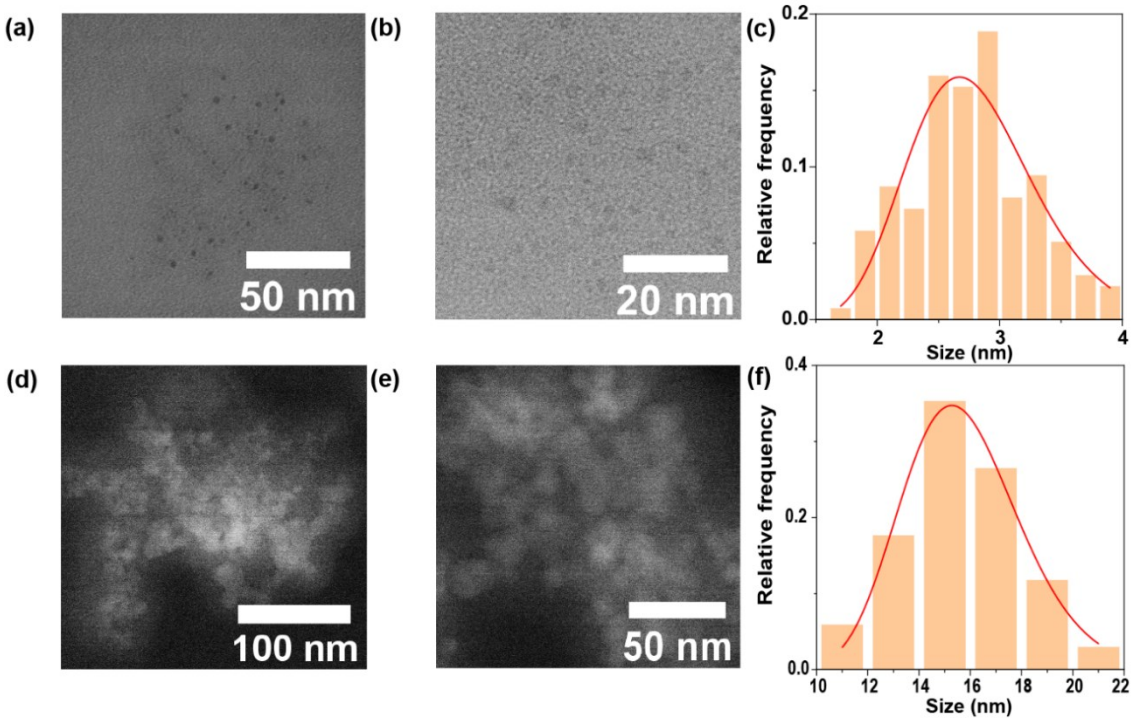

Figure 2.S2. Scanning Transmission Electron Microscopy (STEM) (a) images of CDLP-D (b) with size distribution in (c); STEM images of CD (d) and (e) with size distribution in (f). The histogram of nanoparticle's size distribution was generated by counting at least 150 nanoparticles from several images obtained. The red solid line represents the fitted log-normal distribution, providing an average particle size of 2.8 $\pm$ 0.5 nm for CDLP-D and 15.8 $\pm$ 2.3 nm.

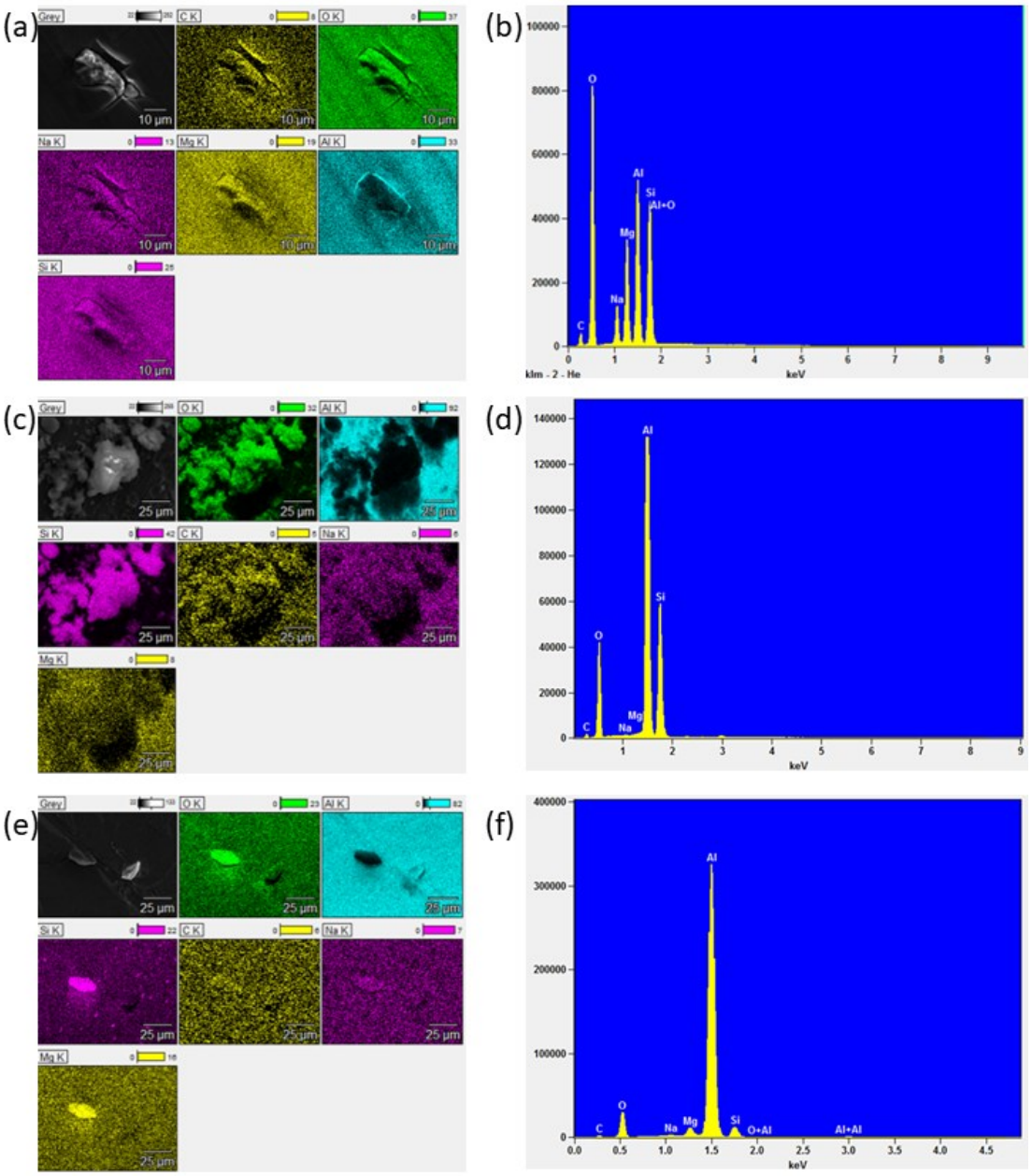

Figure 2.S3. EDX mapping using SEM microscope coupled with EDX spectrometer for CDLP-A (a), CDLP-D (c) and Lap (e); with the respective EDX spectrum (b), (d) and (f). The alluminum content is from the substrate used.

Table 2.S2 - FTIR band assignments for the bonds vibrations of the samples in the region of 4000 - 410 cm-1; υ represents stretching, and δ deformation

Wavenumber (cm^{-1})	**Assignment**	**Refs**
3690	υ(Mg_3OH)	[37]
3720 – 3000	υ(OH)/ υ(NH)	[38,39]
2934	υ(CH)	[38,39]
1774	υ(C=O) – conjugation with oxygen	[38,39]
1704	υ(C=O) – amide	[38,39]
1656	δ(NH)	[38,39]
1632	δ(OH) – adsorbed water	[38,39]
1596	υ(COO) – carboxylate asymmetric	[40–42]
1552	υ(C=C)/ υ(C=N) – aromatic ring	[38,39]
1440	δ(CH)	[38,39]
1392	υ(COO) – carboxylate symmetric/ δ(C–N)	[40–42]
1296	δ(COH)	[38,39]
1172	υ(CO)	[38,39]
966	υ(SiO)	[37]
643	δ(MgO)	[37]
430	δ(Si–O–Si)	[37]

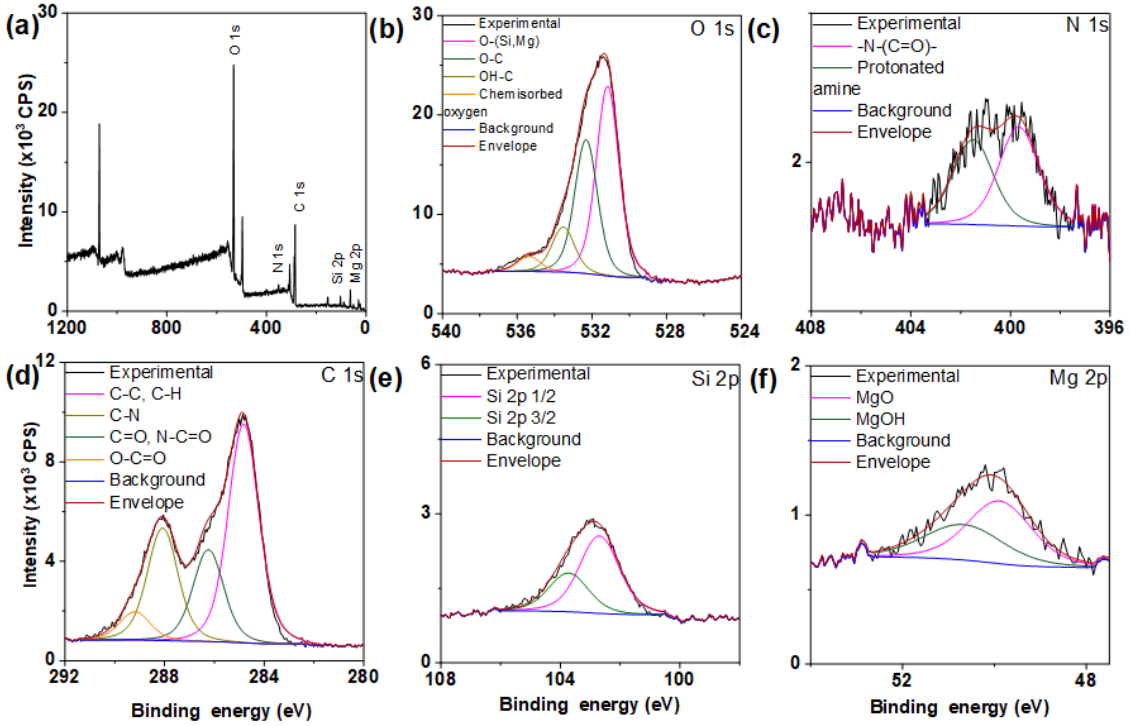

Figure 2.S4. X-Ray Photoelectron Spectroscopy survey spectrum of CDLP-D (a); high-resolution XPS spectrum of O 1s (b), N 1s (c), C 1s (d), Si 2p (e) and Mg 2p (f) of CDLP-D sample.

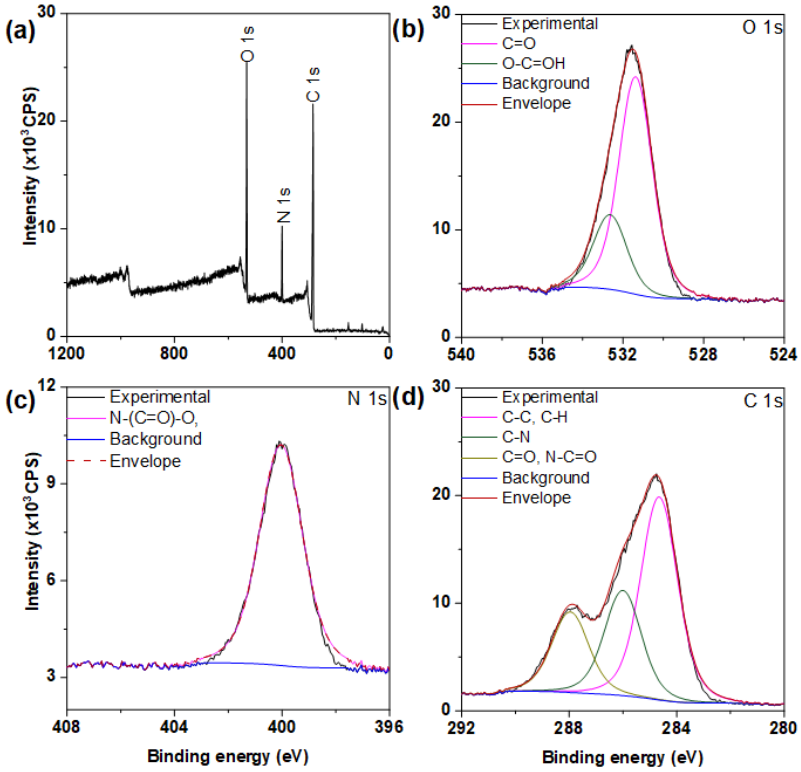

Figure 2.S5. XPS survey spectrum of CD (a); high-resolution XPS spectrum of O 1s (b), N 1s (c) and C 1s (d) of CD sample.

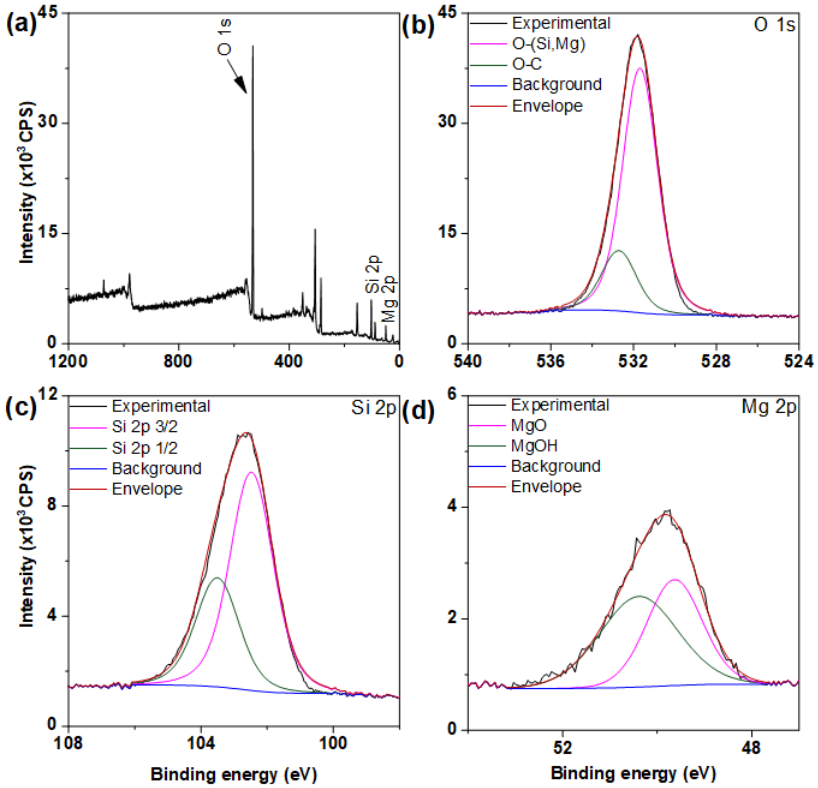

Figure 2.S6. XPS survey spectrum of Lap (a); high-resolution XPS spectrum of O 1s (b), Si 2p (c) and Mg 2p (d) of Lap sample.

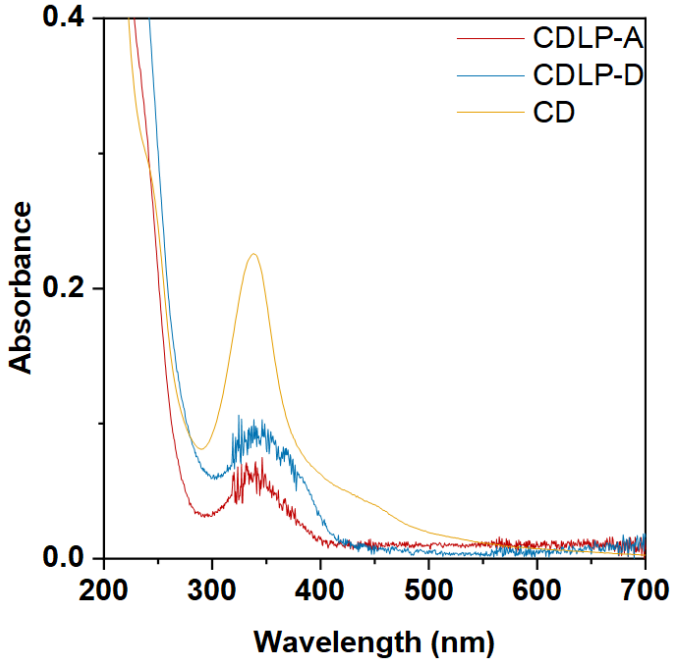

Figure 2.S7. UV-Vis spectrum in the 200 – 800 nm range of 1.0 mg·mL−1 water suspension of CD, CDLP-A, and CDLP-D samples.

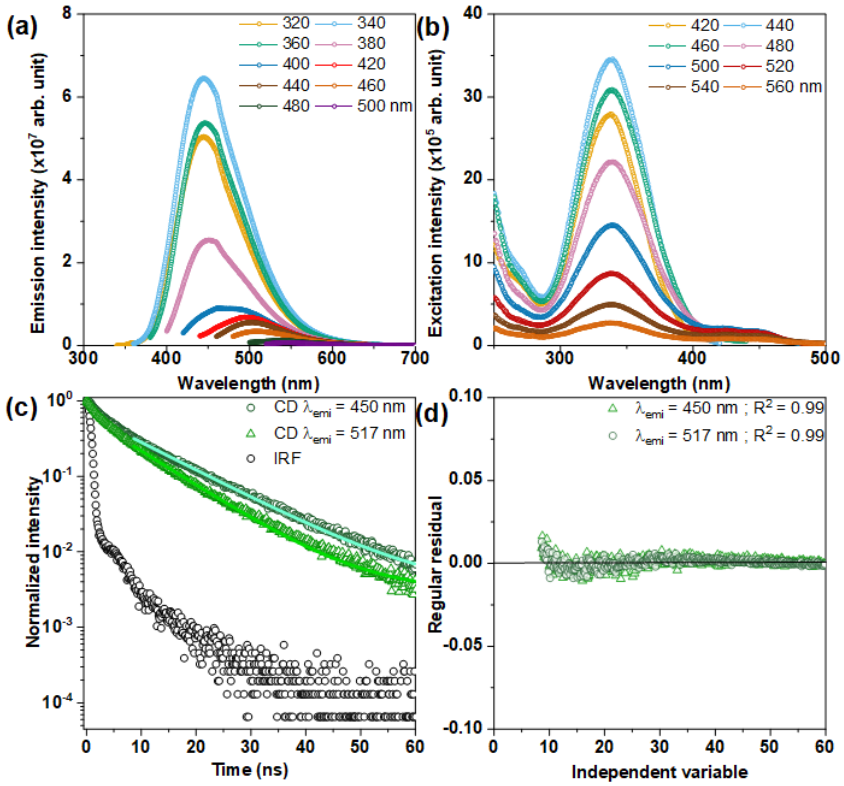

Figure 2.S8. Room temperature (298 K) (a) emission and (b) excitation spectra of CD in water suspension. (c) Room temperature emission decay of CD suspension using a 388 nm nano-LED monitoring emission at 450 and 517 nm. (d) Residual plots of the monoexponential fitting on the decay curves presented in (c). For suspension, the quantum yield (ϕ) at excitation wavelengths of 360, 400, and 500 was 0.06 ± 0.01, 0.03 ± 0.01 and 0.01 ± 0.01 respectively; for solid sample in all excitation wavelengths, the ϕ was below 0.01. The lifetime obtained by monoexponential fitting in the emission decay curve for suspension was 12.0 ± 1.2 and 9.4 ± 0.9 ns for 450 and 517 nm wavelength emission, respectively.

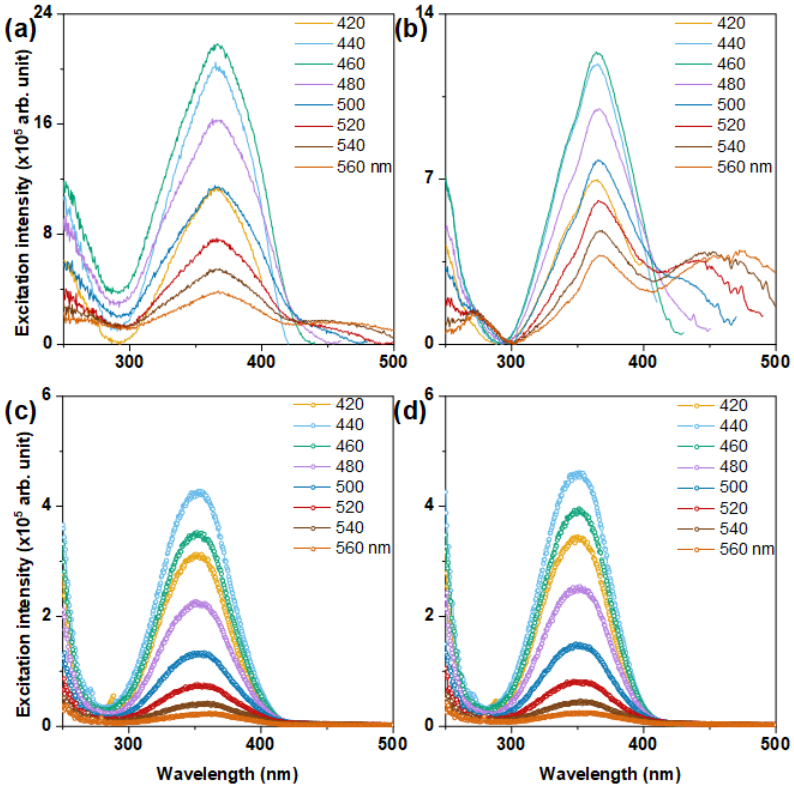

Figure 2.S9. Room temperature excitation spectra of CDLP-A in (a) powder and (c) water suspension and CDLP-D in (b) powder and (d) water suspension, respectively.

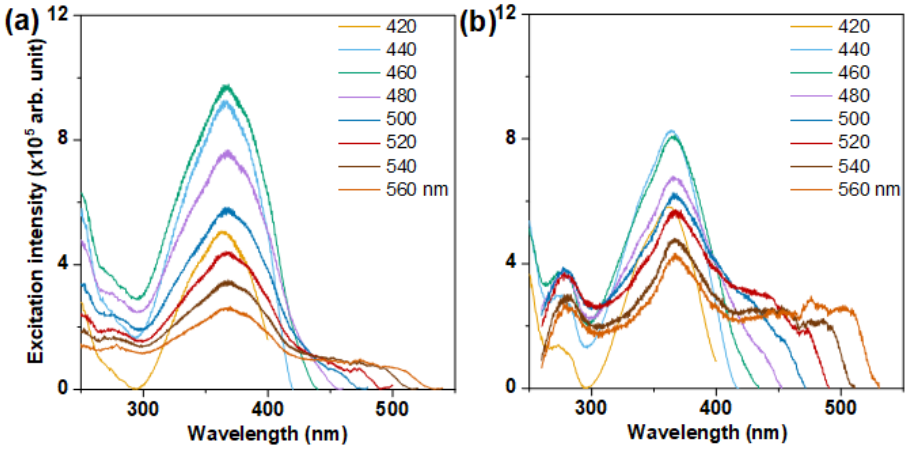

Figure 2.S10. Low temperature (13 K) excitation spectrum of (a) CDLP-A and (b) CDLP-D.

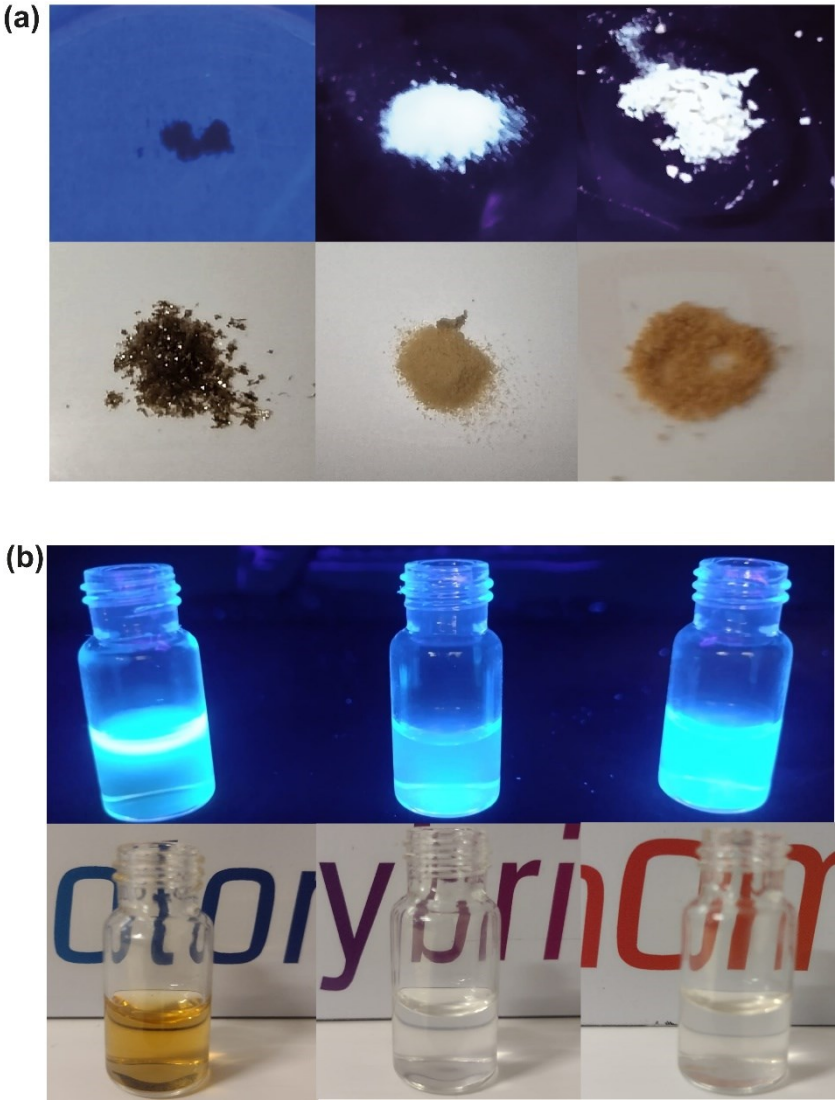

Figure 2.S11. Photographs of powder (a) and water suspension (b) samples, with UV lamp (λ_exc = 365 nm) above and room light below. From left to right: CD, CDLP-A and CDLP-D.

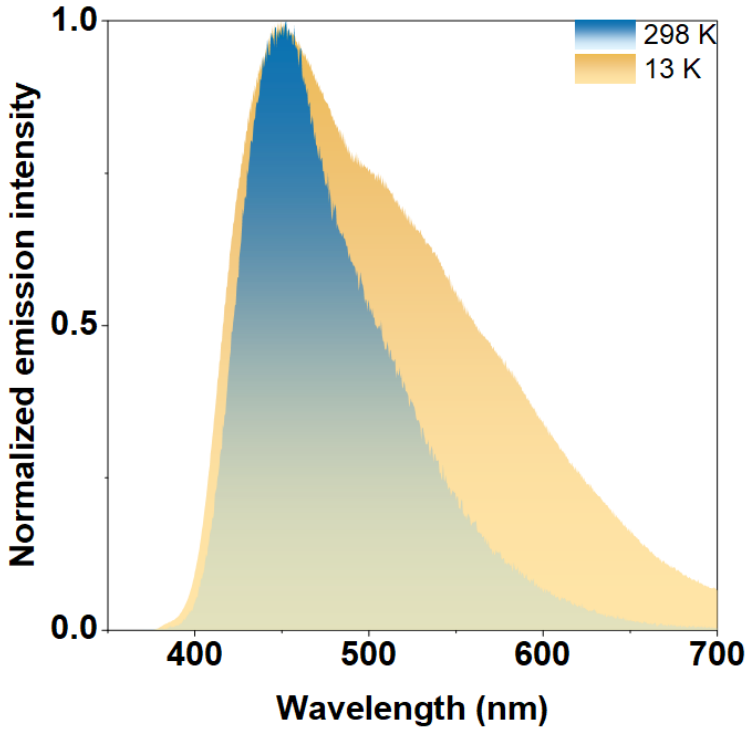

Figure 2.S12. Room and low temperature emission comparison of CDLP-A.

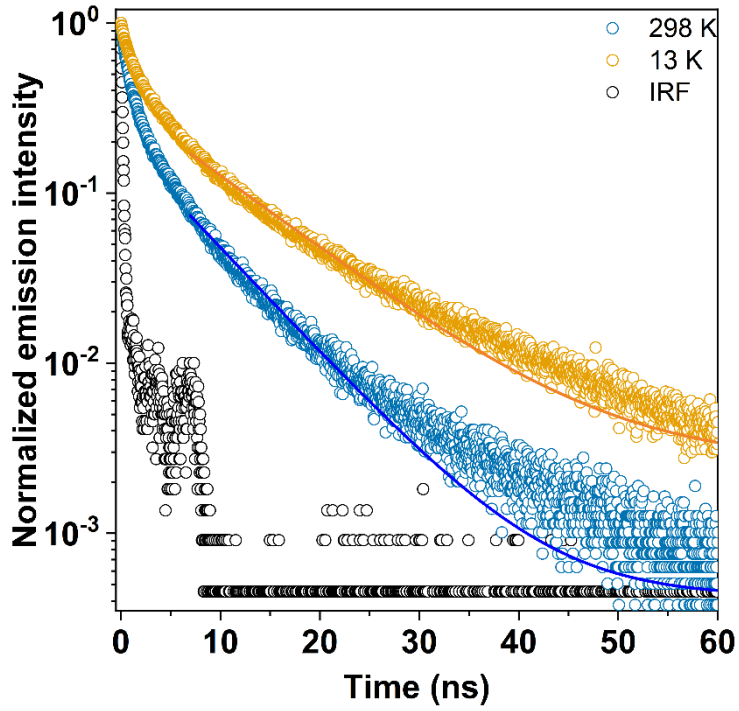

Figure 2.S13. Room and low temperature decay curves of CDLP-D monitored at 450 nm and excited at 375 nm using a nano-LED. IRF is the instrumental response function. The model used was $y = y_0 + \sum_n A_n \exp\left(-(t_n - x_0)/\tau_n\right)$, where y is the PL intensity, y_0 is a constant, A_n the amplitude of the n component of the decay, t_n is the experimental decay data, and x_0 = 6.96 ns is obtained by the instrument response function. The best fitting was achieved by applying one component. Lifetime obtained at 298 K was $\tau_{450}^{298} = 7.0 \pm 0.1$ ns and at 13 K was $\tau_{450}^{13} = 10.0 \pm 0.1$ ns.

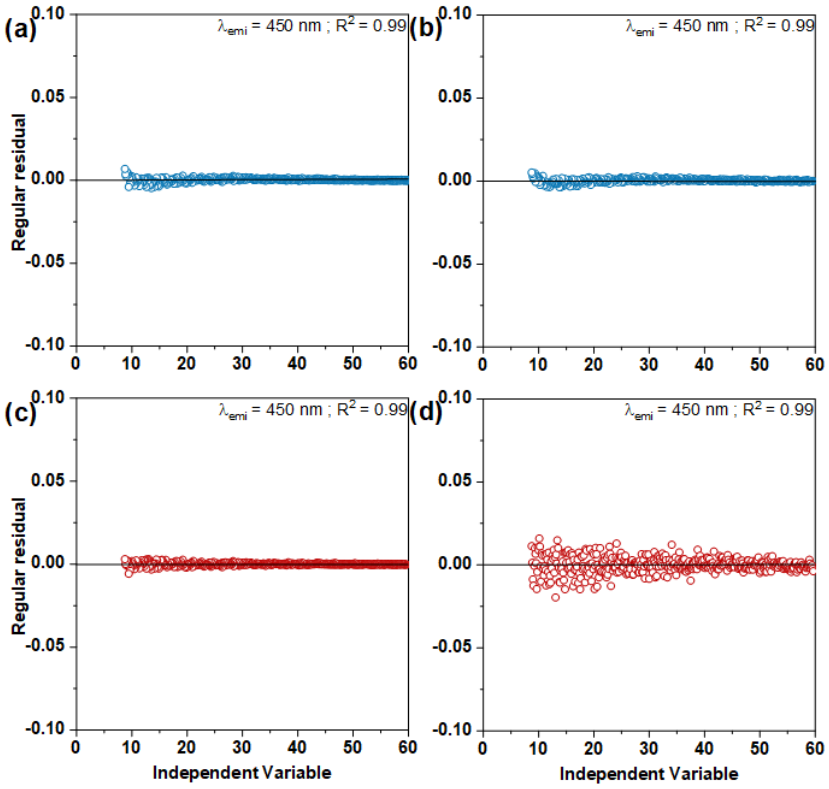

Figure 2.S14. Residual plots of the monoexponential fits of the room temperature emission decay curves at 450 nm of CDLP-A (a) powder and (c) suspension and CDLP-D (b) powder and (d) suspension. A 388 nm nano-LED was used as the excitation source.

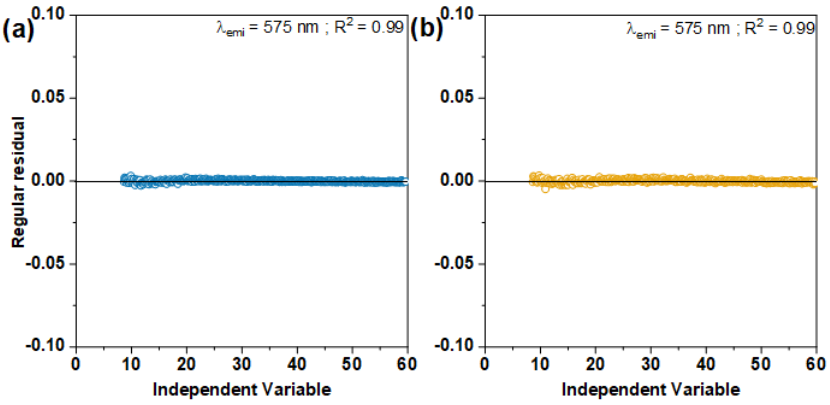

Figure 2.S15. Residual plots of the monoexponential fits of the (a) room and (b) low temperature emission decay curves at 575 nm of CDLP-D. A 388 nm nano-LED was used as the excitation source.

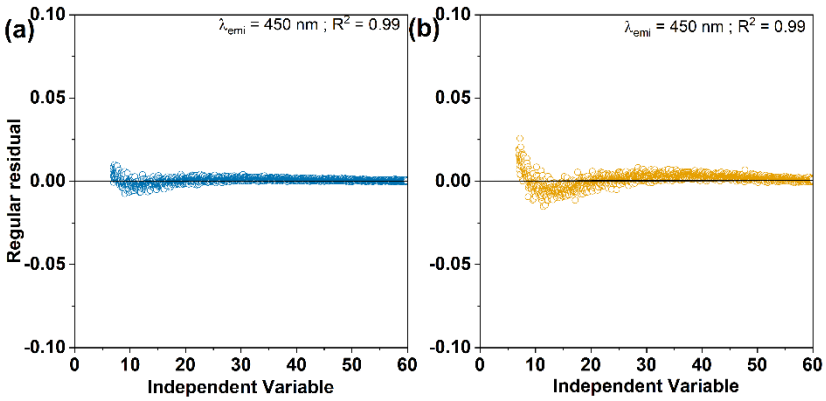

Figure 2.S16. Residual plots of the monoexponential fits of the (a) room and (b) low temperature emission decay curves at 450 nm of CDLP-D. A 375 nm nano-LED was used as the excitation source.

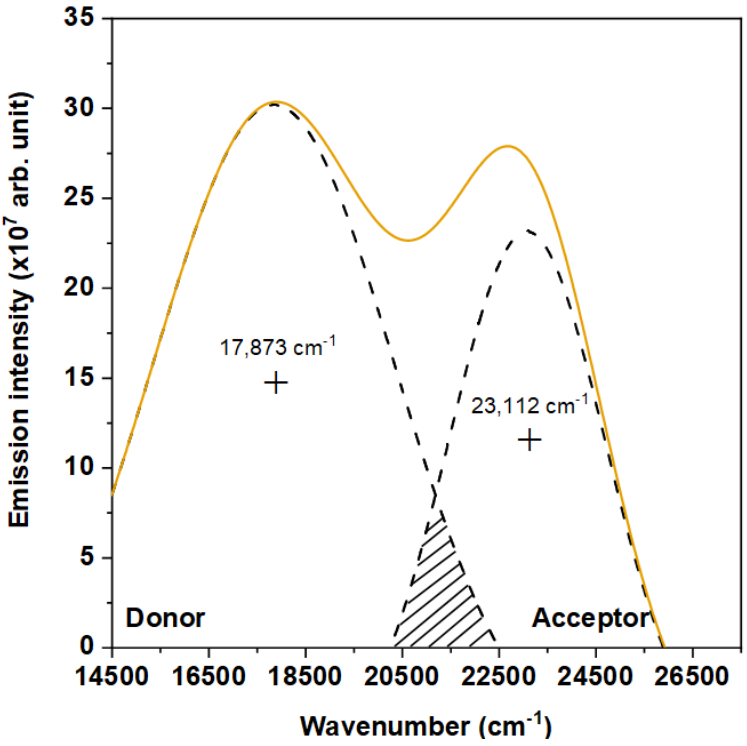

Figure 2.S17. Deconvolution of CDLP-D emission band with respective barycenter. σ_D = 17,873 cm^{-1} with γ_D = 5,194 cm^{-1} and σ_A = 23,112 cm^{-1} with γ_A = 3,232 cm^{-1}.

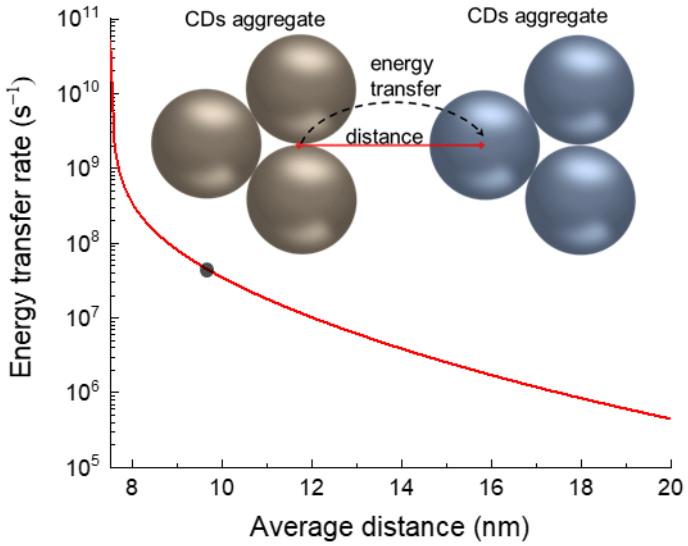

Figure 2.S18. Estimated energy transfer rate between CDs aggregates as a function of their average distance. The black point corresponds to the experimental rate $W = 4.7\times10^{7}$ s^{-1} attributed to the distance of 9.6 nm.

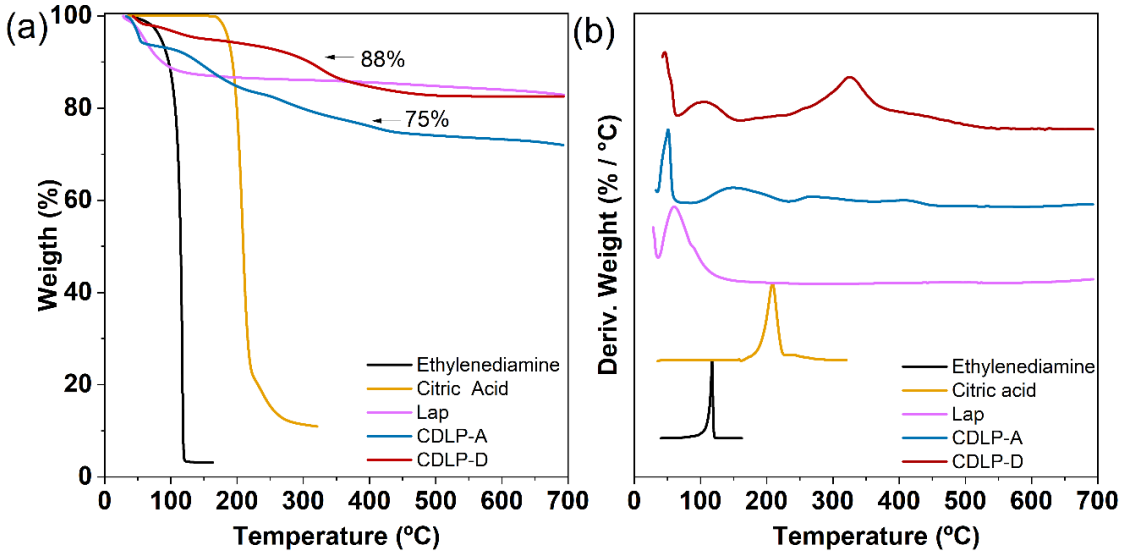

Figure 2.S19. Thermogravimmetic curves (TGA) (a) and derivate thermogravimetric curves (DTG) (b). The weight loss was determinated by TGA curve, using the event obtained in DTG of CDs decomposition, which was 326ºC for CDLP-D and 411 ºC for CDLP-A.

Table 2.S3 - CHN elemental analysis for CDLP-A and CDLP-D samples

Samples	**% C**	**% H**	**% N**
CDLP-A	8.0 (±0.2)	2.1 (±0.1)	0.4 (±0.1)
CDLP-D	9.0 (±0.2)	1.6 (±0.1)	2.2 (±0.1)

CHAPTER 3

Carbon Dots on LAPONITE® Hybrid Nanocomposites: Hg^{2+} sensing and quenching mechanism evaluation

3. Carbon dots on LAPONITE® hybrid nanocomposite: Hg^{2+} sensing and photoluminescence emission quenching mechanism

Bruno S. D. Onishi[a,*], Albano N. Carneiro Neto[b], Sidney J. L. Ribeiro[a,*]

Abstract

Motivated by the importance of Hg^{2+} detection in water due to the harmful effect on the environment and human health, we investigated a recently developed nanocomposite based on carbon dots (CDs) and LAPONITE® as an optical chemical sensor using photoluminescence emission. While several studies have reported the Hg^{2+} detection using CDs photoluminescence emission there is a lack of in-depth investigation into the quenching mechanisms involved in turn-off sensors. In this study, we propose a Stern-Volmer analysis at three different temperatures (288, 298, and 303 K). The results indicated selectivity for Hg^{2+} over the other evaluated metal. The optimum detection range for Hg^{2+} was found to be 0-40 μM, with limits of detection (LOD) and quantification (LOQ) of 2.5 and 8.3 μM respectively. Using the Stern-Volmer models, we found that static quenching dominates over collisional quenching, possibly due to the complexation between nanocomposite's carboxylate groups and Hg^{2+}. Additionally, the modified Stern-Volmer model, which accounts for the fractional accessibility of the fluorophores by the quenchers, suggests that some parts of the sensor are inaccessible to the quencher.

a. Institute of Chemistry, São Paulo State University – UNESP, São Paulo, Araraquara, 14800-060, Brazil,

b. Institute of Physics and CICECO – Aveiro Institute of Materials, University of Aveiro, 3810-193 Aveiro, Portugal

*e-mail: bruno.onishi@unesp.br; sidney.jl.ribeiro@unesp.br

3.1. Introduction

Due to the harmful effects of heavy metals on the human body and the environment, monitoring strategies in water bodies are necessary for detection and quantification. Metal ions such as Cd^{2+}, Cr^{6+}, Co^{2+}, Cu^{2+}, Pb^{2+}, Hg^{2+}, Zn^{2+}, As^{3+}, and Ag^{+}, even in minimal concentrations, cause harmful effects on humans, flora, and fauna. Various studies have associated high concentrations of these contaminants with industrial and urban waste, due to both negligence in waste treatment and industrial accidents.[1–4] The toxicity of metals is primarily associated with the binding of non-essential metals to physiological sites intended for essential metals.[5] A highly toxic metal ion is $Hg^{2+,}$ which has a high affinity for thiol groups, forms covalent bonds with cysteine residues in proteins, and produces reactive oxygen species. Additionally, it reduces antioxidant concentrations, leading to the accumulation of free radicals, which induce cellular DNA damage and can initiate carcinogenic processes.[5–7]

Atomic absorption spectroscopy (AAS), inductively coupled plasma mass spectrometry (ICP-MS), X-ray fluorescence spectroscopy (XRF), and voltammetry are the analytical instruments used for heavy metal quantification.[8] However, common disadvantages of conventional metal detection techniques are primarily associated with high cost, lengthy analysis time, complex instrumentation, and the need for extensive sample preparation. Optical chemical sensors are low-cost sensors that use the interaction of electromagnetic radiation with the analyte to generate an analytical signal based on a specific optical parameter, such as absorption, emission, lifetime, and anisotropy, which can be correlated with concentration.[9,10] Photoluminescence (PL) emission intensity is the most commonly monitored measurement. When an analyte causes quenching, it is possible to establish a relationship between the concentration of the quencher and the emission intensity by developing an analytical curve. This allows for the detection and quantification of the quencher analyte's concentration. This process describes the basic principle of a photoluminescent chemical sensor.[11,12] Fluorescence emission intensity is the most commonly monitored measurement, with quenching reducing the emission intensity. When an analyte causes quenching, it is possible to establish a relationship between the concentration of the quencher and the emission intensity by developing an analytical curve. This allows for the detection and quantification of the quencher analyte's concentration. This process describes the basic principle of a PL chemical sensor.

Given the straightforward of synthetic routes and the optical properties such as tunable PL and remarkable quantum yield, carbon dots (CDs) can be applied in various areas of

photonics.[13–16] One significantly reported application in the literature is as sensors, both chemical sensors for identifying and quantifying ions and molecules, and physical sensors like temperature sensors.[17–19] Their solubility in aqueous media and easily modifiable surface make them potential candidates for applications in various biological and environmental media, and adaptable for greater selectivity towards analytes. Additionally, due to their large surface area, surface states are extremely sensitive, allowing for easy interaction with the environment and consequent changes in emission, either through quenching or fluorescence sensitivity—desirable characteristics in PL chemical sensors.

Recently, we published a study of solid-state emission from nanocomposite based on carbon dots on LAPONITE®.[20] We demonstrated that besides the solid-state emission, the samples presented emission in a water suspension with great absolute quantum yield (0.22). Another result found was the predominance of carboxylate groups in the nanocomposite due to the incorporation of LAPONITE®, which can potentially interact with the Hg^{2+} metal ion. This finding motivated further investigation into its potential application as a PL chemical sensor for Hg^{2+}. Although many studies of Hg^{2+} sensing, none have deeply investigated the quenching mechanism, usually associated with electron transfer from CDs excited states to Hg^{2+} based on emission decay measurements.[21–26] Herein, we propose a Stern-Volmer investigation in three different temperatures (288, 298 and 303 K), and the application of Stern-Volmer and modified Stern-Volmer models, which provide information about the PL quenching mechanism tendencies.

3.2. Experimental

The synthesis and characterization of the nanocomposite based on Carbon dot/LAPONITE® can be found in previous work.[20] The sample used was CDLP-D and CD (sample without LAPONITE®). The photoluminescence (PL) measurements were also carried out on a Horiba-Jobin Yvon Fluorolog – 3 FL3–22 spectrofluorometer equipped with a Hamamatsu R928P photomultiplier. A continuous xenon lamp FL-1039A/40A 450 W was used for the excitation and the emission spectra. For the photoluminescence decay a pulsed diode light source NanoLED-350 (Horiba-Jobin Yvon) with a wavelength of 350 nm.

3.2.1. Pre-sensing assay

To verify the best conditions for the Hg^{2+} sensing assays, photostability experiments were performed in function of pH, sensor concentration, time and ionic strength, without Hg^{2+} species. For all the PL emission measurements, the excitation wavelength (λ_{exc}) was 360 nm.

For pH measurements, 0.1 mg mL^{-1} of CDLP-D or CD was suspended in ultrapure water (MilliQ®) and the pH, measured with a pH meter, was adjusted with NaOH or HCl (concentration adjusted according to the pH). The assay was made in duplicate for each pH ranging from 2-11. The PL emission was measured for each sample with the adjusted pH and the spectra shown in Figure 3.1 (a) are a mean for each pH.

For the sensor concentration assay, the CDLP-D 5.0 mg mL^{-1} water suspension was diluted for concentrations of 0.01, 0.05, 0.1, 0.3, 0.5, 1.0, 2.0, 3.0, and 4.0 mg mL^{-1}. The PL emission was measured for each sample, including for 5.0 mg mL^{-1}. The same procedure was applied for CD but in the range of 0.01 – 0.5 mg mL^{-1}, using a suspension of 1.0 mg mL^{-1}.

The photostability in function of time was performed at a controlled temperature of 298 K using a FL-1027 Single-position thermostatted cell holder coupled with an external circulating temperature bath, that pumped a mixture of ethylene glycol-water. The holder also includes a magnetic stirrer that was used to agitate the suspension during the measurements. This system is coupled to the spectrofluorometer. The spectra were collected every hour until 8 h, in which the CDLP-D or CD 0.1 mg mL^{-1} water suspension remained continuously irradiated by the xenon lamp at 360 nm.

The ionic strength assay was made by suspending the 0.1 mg mL^{-1} CDLP-D or CD sample in KCl solutions, with the concentrations ranging were 0.1, 0.3, 0.5, 0.7 and 0.9 M, prepared from dilution of 1.0 M KCl. It was performed in duplicate and each sample measured the PL emission.

3.2.2. Metals and Hg^{2+} detection

Except for Zn^{2+}, which was prepared from $Zn(NO_3)_2.6H_2O$, all metals were prepared from the chloride salts. The solution was primally prepared with a concentration of 1000 μM in ultrapure water and diluted to 100 μM, where the 0.1 mg mL^{-1} CDLP-D or CD was suspended. The assay was made in triplicate, with a 1.0 mL of volume and the PL

emissions were measured for each sample. Before the measurements, the samples were incubated at 295 K for 10 minutes

The same procedure was made for Hg^{2+} and Fe^{3+}, but the CDLP-D or CD was suspended in a larger range of concentration from 0-900 μM.

3.3. Results and discussion

3.3.1. Pre-sensing

According to the photoluminescence (PL) emission spectra presented in Figure 3.1(a), the emission intensity of CDLP-D remains stable in the range of pH = 4 – 7, with minor quenching in pH 8 and 9 and considerable quenching in pH = 2 and 3; 10 and 11. In addition, in acid pH (2 and 3), it is possible to notice the red shift in emission spectra. Liu et al. demonstrated in their review, three possible mechanisms for the pH-dependent PL mechanisms for CDs: Change of energy level, aggregation and pH-induced electron transfer.[27] Based on previous results,[20] the surface of CDLP-D is predominantly composed of carboxyl and hydroxyl groups, which can protonate and deprotonate in acid and basic pH respectively and possibly affect the energy level state.[27,28–30] In acid pH the higher concentration of H^+ also can contribute to aggregation-induced quenching.[27,31,32] On the other hand, the PL emission of the sample without LAPONITE® (CD) is less intense in basic pH (10 and 11) in comparison with CDLP-D, while the behavior in the range of pH = 4-8 presented stability (Figure 3.S1(a)). These results follow the hypothesis of the CDs emission from surface states due to functional organic groups, however, it is not totally clear the pH-dependent PL mechanisms in our samples, and more studies must be made looking into PL decay, zeta potential and UV-Vis absorption, all in the function of pH, which is not the aim of this work.

The PL emission intensity of CDLP-D enhanced from 0.01 to 2 mg mL^{-1}, following a quenching as the concentration enhanced from 3 to 5 mg mL^{-1}, as can be seen in the PL emission spectra present in Figure 3.1(b). This quenching can be related to an aggregation-induced quenching frequently mentioned in CDs samples.[33,34] This also occurs in the CD sample (Figure 3.S1(b)). However, in this case, the quenching starts at 0.5 mg mL^{-1}, a lower concentration compared to CDLP-D. The CDLP-D sample had a 16% relative integrated area emission reduction at 8h of continuous irradiation by UV source (Figure 3.1(c)), while the CD sample presented 12% at the same time (Figure 3.S1(c)). In addition, CD sample presented higher photostability in function of ionic

strength (Figure 3.S1(d)), with a reduction lower than 5% of the relative integrated while the CDLP-D was lower than 12%.

From an experimental point of view, the work concentration of CDLP-D for sensing assays was 0.1 mg mL^{-1}, in which the suspension's pH was equal to 6.0. Each measurement takes around 3 min of continuous irradiation of UV light per sample. Taking into account that only 2% of the integrated area was reduced in 1h of continuous irradiation, the sample can be considered photostable within the measured timeframe, equating to a proportional reduction of 0.1% reduction. Furthermore, despite the interference from a high concentration of KCl resulting in a 10% hindrance in PL emission, the concentration of the metal salts used fell within the range of μM.

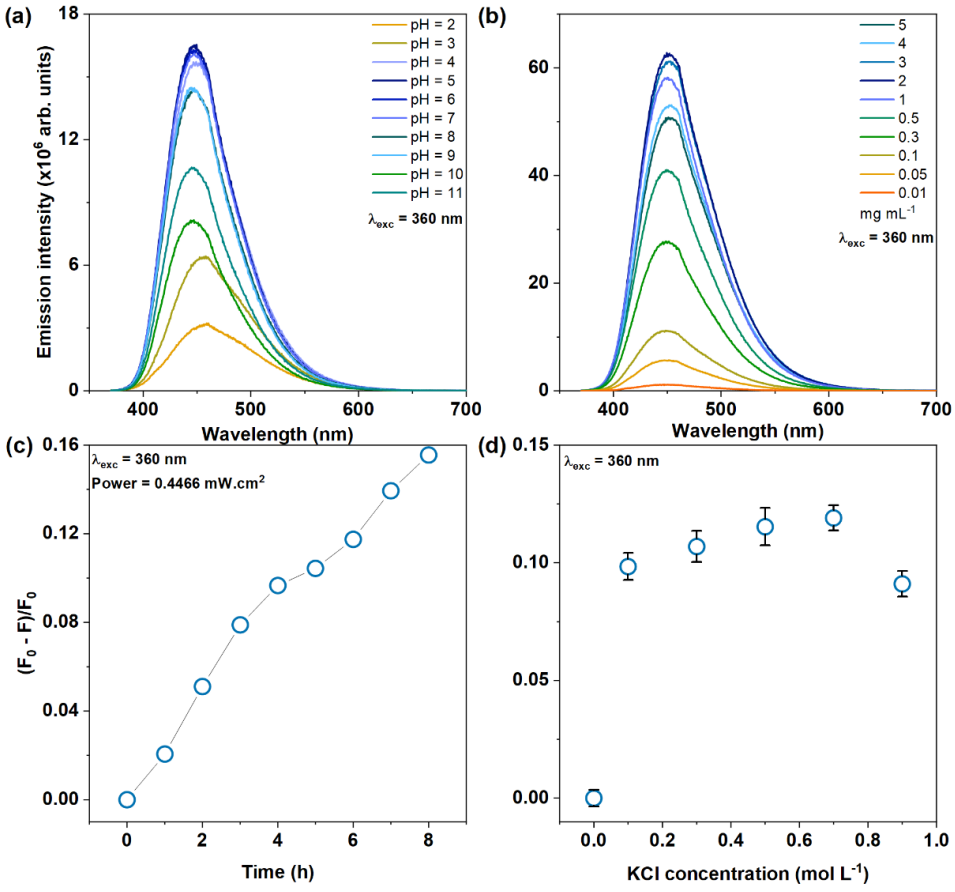

Figure 3.1. Emission spectra of CDLP-D in function of pH (a) and concentration (b); relative integrated area of emission band in function of time (c) and ionic strength (d) – F_0 is the integrated area of the CDLP emission spectrum at 0h (c) and 0 mol L^{-1} KCl (d), and F is the integrated area of the CDLP emission spectrum at xh (c) and y mol L^{-1} (d) (x = 1 to 8h; y = 0.1 to 0.9 mol L^{-1}). For (a), (c) and (d) the CDLP concentration was 0.1 mg mL^{-1}.

3.3.2. Detection of Hg^{2+} by photoluminescence emission quenching

To verify the selectivity of CDLP-D to Hg^{2+}, PL sensing assays with other ions metals such as Mn^{2+}, Fe^{3+}, Fe^{2+}, Co^{2+}, Ni^{2+}, Zn^{2+}, Mo^{2+}, Cd^{2+} and Pb^{2+} were performed as can be seen in Figure 3.2. Notably, in the concentration of 100 μM of Hg^{2+}, there was a reduction of 58% of the relative integrated area emission of CDLP-D, indicating great quenching due to the interaction with Hg^{2+}. In comparison with other metals, the integrated area was affected by less than 5%, except for Fe^{3+}, which affected 18%. This could have occurred due to the absorption in the same excitation wavelength of CDLP-D (λ_{exc}=360 nm) by Fe^{3+} complex ions formed in water such as $Fe(OH)_2^+$ in the work pH.[35] However, in the sensor's range of 1 – 40 μM, the integrated area is affected by less than 7% as can be seen in Figure 3.3(b). In addition, the other metals also did not affect considerably the Hg^{2+} quenching as can be seen in the blue bar of Figure 3.2.

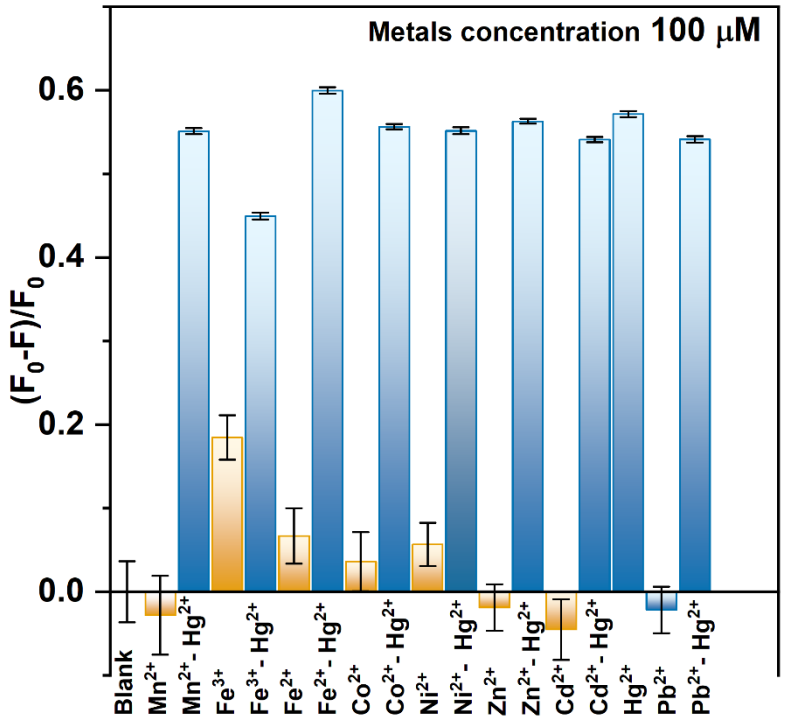

Figure 3.2. Relative emission integrated area of CDLP-D using 100 μM of Mn^{2+}, Fe^{3+}, Fe^{2+}, Co^{2+}, Ni^{2+}, Zn^{2+}, Cd^{2+}, Pb^{2+} (yellow bar) and each one together with Hg^{2+} (blue bar). F_0 is the blank integrated area emission (CDLP-D) and F is the integrated area emission in the presense of the respective metals.

The CDLP-D PL emission in the function of Fe^{3+} concentration was evaluated to verify the interference range in the measurements. Figure 3.3(a) depicts the emission spectra of CDLP-D in 0-900 μM range of Fe^{3+} concentration. It is possible to notice the variation in emission spectra only in high concentrations of Fe^{3+} depicted as green to yellow color, remaining in the range of 100 – 900 μM. However, in 0-40 μM, which is the best work

range for the Hg^{2+} detection, the relative integrated emission area remained below 7%, as can be seen in Figure 3.3(b), indicating minimum Fe^{3+} interference in this range.

In the case of Hg^{2+}, in Figure 3.3(a) it is possible to notice a plateau of quenching in 100-900 μM range, with the same PL emission variation (depicted as green-yellow). Conversely, in 0-90 μM range the emission spectra decrease in intensity as the Hg^{2+} concentration increases, depicted as blue to green-yellow. The optimum range found for Hg^{2+} detection was between 1-40 μM, where it was possible to establish a good linear calibration curve with a great correlation coefficient ($R^2 = 0.992$) and linear equation of $y = 0.016x + 0.024$, which can be used to quantify the Hg^{2+} concentration, where $y = \frac{F_0 - F}{F_0}$ and x the $[Hg^{2+}]$. The limit of detection (LOD) and limit of quantification (LOQ) found by measuring 10 blank samples were 2.5 and 8.3 μM respectively.[36] These values are in the range of following works,[22–24] however, several reports found low LOD in the range of nM.[25,26]

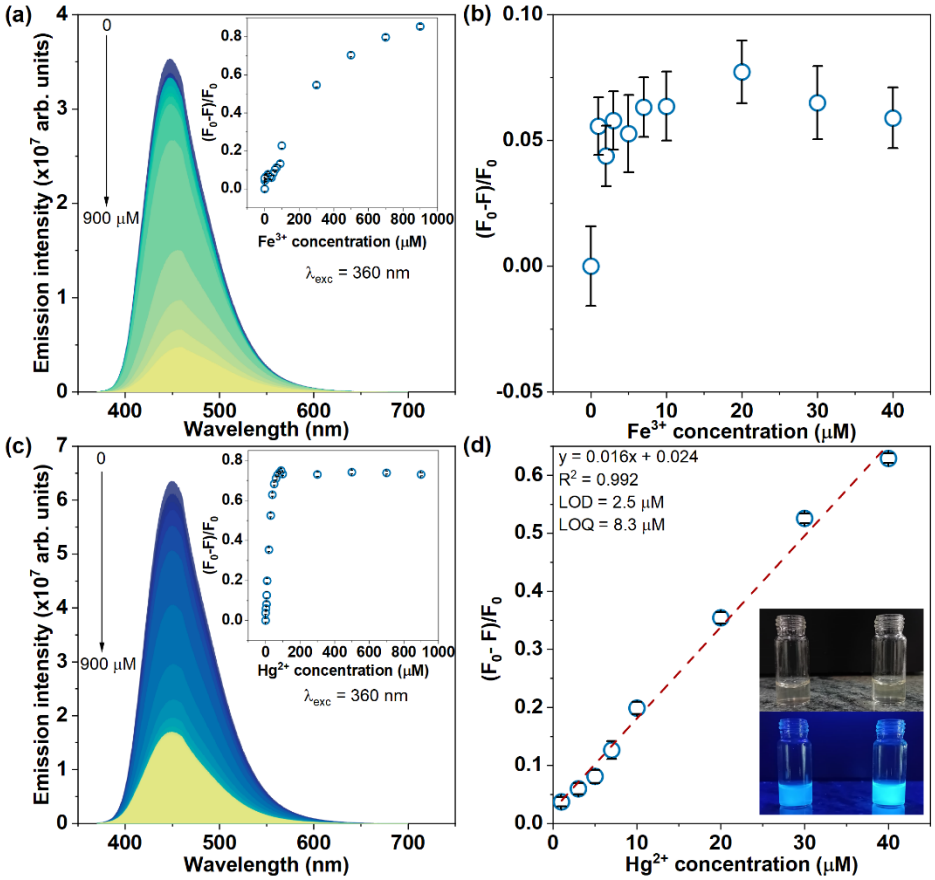

Figure 3.3. PL emission spectra of CDLP-D in function of Fe^{3+} (a) and Hg^{2+} (b) concentration from 0 to 900 μM. The insert graph in (a) and (c) are the relative integrated emission area in function of Fe^{3+} and Hg^{2+} concentration in 0-900 μM range respectively, as well as (b) and (d) in 0-40 μM. The insert picture in (d) represents the CDLP-D suspension with Hg^{2+} 50 μM (left) and without Hg^{2+} (right), where below, it is possible no notice a less intense bright of CDLP-D emission in the presense of Hg^{2+}, under 375 nm UV lamp irradiation.

In comparison with CD sample, the optimum range for Hg^{2+} sensing was between 10 – 60 μM, with R^2 = 0.986, linear equation of y = 0.0058x + 0.10 and LOD and LOQ of 11.9 and 39.3 μM respectively (Figure 3.S2(d)). However, in this range, for CD the relative integrated emission area remained below of 20% for Fe^{3+} ions (Figure 3.S2(b)), indicating high interference of Fe^{3+} ions in Hg^{2+} detection, because the quenching remained below 40% of total emission in Hg^{2+} sensing assay. These results indicate a better performance of the composite for Hg^{2+} detection instead of the CD sample.

3.3.3. Quenching mechanisms of Hg^{2+}

To establish a possible PL emission quenching mechanism by Hg^{2+}, two Stern-Volmer models, were applied at three different temperatures. The analysis in different temperatures could provide information about the mechanism tendencies if it is collisional or static quenching.[37] The first model is described by Stern-Volmer equation (1), where K_{sv} is the Stern-Volmer quenching constant.

$$\frac{F_0}{F} = 1 + K_{sv}[Hg^{2+}] \quad (1)$$

It is possible to notice in Figure 3.4(a) a deviation from linearity in all temperatures when the first model was applied. This can be associated with a high quencher concentration or when the deviation is toward the x-axis, more than one fluorophore population is present.[11,37] As mentioned in previous work,[20] the CDLP-D emission originated from the byproducts on the surface or the nanoparticle's core (high energy) and surface states due to organic functional groups (low energy). Thus, the deviation is expected. The temperature enhancement resulted in lower K_{sv} values, presented in Table 3.1, which is not characteristic of collisional quenching behavior, since higher temperatures promote faster diffusion.[37,38] Conversely, it is consistent with a static behavior with the formation of a non-fluorescent complex, in which the higher temperature promotes the dissociation of the quencher-fluorophore bond. [37,38]

In the case of collisional quenching, the quencher affects the excited state of the fluorophore by collisional interaction, with possible energy or charge transfer mechanisms involved.[12,37,38] The results from emission curve decay revealed that in high Hg^{2+} concentration (100 μM), the excited state was affected. The lifetime without Hg^{2+} obtained was τ_0 = 12.74 $\pm$ 0.03 ns, and with 100 μM decreased to $\tau_{100\,\mu M}$ = 9.16 $\pm$ 0.03

ns. However, in low concentrations of Hg^{2+} (10 μM), $\tau_{10\,\mu M}$ = 12.05 $\pm$ 0.03 ns. Thus, the collisional quenching could occur in high concentrations of Hg^{2+}. In addition, if we consider that the process is diffusion-limited, K_{sv} can be described as $K_{sv} = K_D = k_q\tau_0$, where k_q is the bimolecular quenching constant, which in this case $k_q = 2.81\times10^{12}$ M^{-1} s^{-1}. According to Lakowicz, a diffusion-controlled quenching is around $k_q = 1\times10^{10}$ M^{-1} s^{-1}, and larger values indicated a binding interaction.[37] According to the results, the static quenching process appears to be dominant in low concentrations of Hg^{2+} rather than the collisional process, but the latter can not be disregarded. This could explain the selectivity of Hg^{2+} toward other metals, which possibly coordinated through the surface carboxylates groups of CDLP-D or through the byproducts formed.

Table 3.1 –Stern-Volmer quenching constant (K_{sv}) obtained from slop of Stern-Volmer plot, and Stern-Volmer quenching constant accessible fraction (K_a) obtained from the slop of modified Stern-Volmer plot

Temperature (K)	**K_{sv} (M^{-1})**	**R^2**	**K_a (M^{-1})**	**f_a**	**R^2**
313	3.22×10^4	0.869	2.87×10^5	0.36	0.957
298	3.58×10^4	0.855	3.11×10^5	0.36	0.955
288	3.63×10^4	0.855	3.05×10^5	0.34	0.961

The modified Stern-Volmer equation (2) (Figure 3.4(b)) considers fractional accessibility of the fluorophores by the quenchers, where f_a is the fraction of fluorescence available of the fluorophore and K_a the Stern-Volmer quenching constant of the accessible fraction[12,37,39] Based on the downward curvature in the Stern-Volmer plot and the aforementioned PL emission origin of CDLP-D, it is reasonable to apply this model in the studied system.

$$\frac{F_0}{F_0 - F} = \frac{1}{f_a K_a [Hg^{2+}]} + \frac{1}{f_a} \qquad (2)$$

This model fitted better compared to the Stern-Volmer plot, according to correlation coefficient (R^2) values. The K_a value decreased with high temperature but increased from 288 to 298 K. In addition, according to f_a values, approximately 0.3 fraction of the total

fluorophore's emission is available for the quencher. These results indicate that there are parts of CDLP-D not accessible for Hg^{2+} quenching.

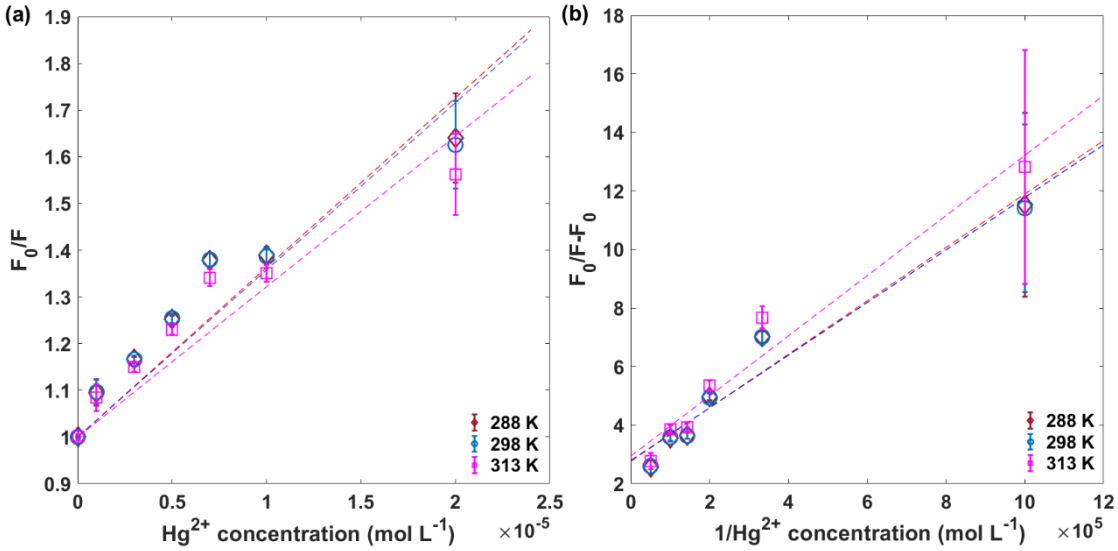

Figure 3.4. Stern-Volmer (a) and modified Stern-Volmer plot (b) at 288, 298 and 313 K

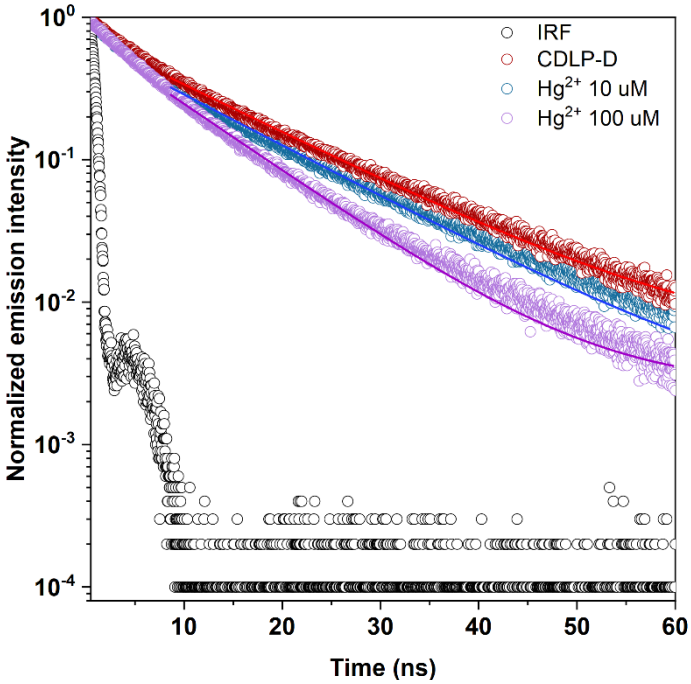

Figure 3.5. Emission decay at room temperature (298 K) for CDLP-D samples in water suspension (red), and in the presence of Hg2+ 10μM (blue) and 10μM (violet) using a 350 nm nanoLED for excitation and monitoring emission at 450 nm. IRF is the instrumental response function. Lifetime (τ) was obtained by fitting emission decay (solid lines). The model used was $y = y_0 + \sum_n A_n exp\ (-(t_n - x_0)/\tau_n)$, where y is the PL emission intensity, y0 is a constant, An the amplitude of the n component of the decay, tn is the experimental decay data, and x0 = 8.7 ns is obtained by the IRF. The best fitting was achieved by applying one component.

3.4. Conclusion

Using the conditions found in the pre-sensing assay, such as neutral pH, low ionic strength and 0.1 mg mL^{-1}, we were able to detect Hg^{2+} in a 0-40 μM range with minimal Fe^{3+} interference in comparison with the evaluated metals. The quenching mechanisms by Stern-Volmer curves indicate a predominance of complex formation over collisional quenching. In addition, there is a part inaccessible for Hg^{2+} quenching.

Conflicts of interest

There are no conflicts to declare.

Acknowledgments

We thank CAPES (finance code:001) for the scholarship.

References

1. Assis, E. M. De *et al.* High concentrations of toxic metals in water consumed by the Maxakali indigenous community in Brazil. *Ambient. e Agua - An Interdiscip. J. Appl. Sci.* **14**, 1 (2019).
2. Da Silva, Y. J. A. B. *et al.* Heavy metal concentrations and ecological risk assessment of the suspended sediments of a multi-contaminated Brazilian watershed. *Acta Sci. - Agron.* **41**, 1–11 (2019).
3. Goncalves, A. C., Nacke, H., Schwantes, D. & Coelho, G. F. Heavy Metal Contamination in Brazilian Agricultural Soils due to Application of Fertilizers. in *Environmental Risk Assessment of Soil Contamination* (InTech, 2014). doi:10.5772/57268.
4. Souza, A. M. *et al.* Seasonal study of concentration of heavy metals in waters from lower São Francisco River basin, Brazil. *Brazilian J. Biol.* **76**, 967–974 (2016).
5. Klaassen, C. & Eaton, D. *The Basic Science of Poisons, 4th ed*. (1991).
6. Valko, M., Morris, H. & Cronin, M. Metals, Toxicity and Oxidative Stress. *Curr. Med. Chem.* **12**, 1161–1208 (2005).
7. Tchounwou, P. B., Yedjou, C. G., Patlolla, A. K. & Sutton, D. J. Heavy Metal Toxicity and the Environment. in *Molecular, Clinical and Environmental*

Toxicology (ed. Luch, A.) vol. 101 133–164 (Springer Basel, 2012).

8. Niessner, H. P. A. G. R. Detection of heavy metals in water by fluorescence spectroscopy : On the way to a suitable sensor system. 182–191 (2000).
9. Li, M., Gou, H., Al-Ogaidi, I. & Wu, N. Nanostructured Sensors for Detection of Heavy Metals: A Review. *ACS Sustain. Chem. Eng.* **1**, 713–723 (2013).
10. Ullah, N., Mansha, M., Khan, I. & Qurashi, A. Nanomaterial-based optical chemical sensors for the detection of heavy metals in water: Recent advances and challenges. *TrAC Trends Anal. Chem.* **100**, 155–166 (2018).
11. Valeur, B. *Handbook of Analytical Techniques Single-Molecule Detection in Solution . Methods and Applications*. *Methods* vol. 8 (2001).
12. Valeur, B. *Molecular Fluorescence Principles and Application*. (Wiley-VHC, 2001).
13. Anwar, S. *et al.* Recent Advances in Synthesis, Optical Properties, and Biomedical Applications of Carbon Dots. *ACS Appl. Bio Mater.* **2**, 2317–2338 (2019).
14. Li, B. *et al.* Recent advances and prospects of carbon dots in phototherapy. *Chem. Eng. J.* **408**, 127245 (2021).
15. Liu, M. L., Chen, B. Bin, Li, C. M. & Huang, C. Z. Carbon dots: synthesis, formation mechanism, fluorescence origin and sensing applications. *Green Chem.* **21**, 449–471 (2019).
16. Yuan, T. *et al.* Carbon quantum dots: an emerging material for optoelectronic applications. *J. Mater. Chem. C* **7**, 6820–6835 (2019).
17. Li, M., Chen, T., Gooding, J. J. & Liu, J. Review of Carbon and Graphene Quantum Dots for Sensing. *ACS Sensors* **4**, 1732–1748 (2019).
18. Seeni Meera, K. M., Murali Sankar, R., Paul, J., Jaisankar, S. N. & Mandal, A. B. The influence of applied silica nanoparticles on a bio-renewable castor oil based polyurethane nanocomposite and its physicochemical properties. *Phys. Chem. Chem. Phys.* **16**, 9276–9288 (2014).
19. Xu, D., Lin, Q. & Chang, H. Recent Advances and Sensing Applications of Carbon Dots. *Small Methods* **4**, 1900387 (2020).
20. Onishi, B. S. D. *et al.* Carbon dots on LAPONITE® hybrid nanocomposites: solid-state emission and inter-aggregate energy transfer. *Nanoscale* **16**, 6286–6295 (2024).
21. Bano, D., Kumar, V., Singh, V. K. & Hasan, S. H. Green synthesis of fluorescent carbon quantum dots for the detection of mercury(ii) and glutathione. *New J.*

Chem. **42**, 5814–5821 (2018).

22. Han, Y., Bian, Y. & Wang, G. A novel nitrogen-doped carbon dots as “on-off-on” fluorescent sensor for ultrasensitive and visual quantitative detection of mercuric (II) and glutathione. *J. Environ. Chem. Eng.* **11**, 110750 (2023).
23. Watcharamongkol, T., Khaopueak, P., Seesuea, C. & Wechakorn, K. Green hydrothermal synthesis of multifunctional carbon dots from cassava pulps for metal sensing, antioxidant, and mercury detoxification in plants. *Carbon Resour. Convers.* **7**, 100206 (2024).
24. Li, L., Yu, B. & You, T. Nitrogen and sulfur co-doped carbon dots for highly selective and sensitive detection of Hg (II) ions. *Biosens. Bioelectron.* **74**, 263–269 (2015).
25. Chan, K. K., Yap, S. H. K. & Yong, K. T. *Biogreen Synthesis of Carbon Dots for Biotechnology and Nanomedicine Applications*. *Nano-Micro Letters* vol. 10 (Springer Berlin Heidelberg, 2018).
26. Ullal, N., Muthamma, K. & Sunil, D. *Carbon dots from eco-friendly precursors for optical sensing application: an up-to-date review*. *Chemical Papers* vol. 76 (Versita, 2022).
27. Liu, C., Zhang, F., Hu, J., Gao, W. & Zhang, M. A Mini Review on pH-Sensitive Photoluminescence in Carbon Nanodots. *Front. Chem.* **8**, 1–9 (2021).
28. Basu, N. & Mandal, D. Time-resolved photoluminescence of pH-sensitive carbon dots. *Carbon N. Y.* **144**, 500–508 (2019).
29. Ozyurt, D., Kobaisi, M. Al, Hocking, R. K. & Fox, B. Properties, synthesis, and applications of carbon dots: A review. *Carbon Trends* **12**, 100276 (2023).
30. Gan, L., Su, Q., Chen, Z. & Yang, X. Exploration of pH-responsive carbon dots for detecting nitrite and ascorbic acid. *Appl. Surf. Sci.* **530**, 147269 (2020).
31. Mondal, T. K., Mondal, S., Ghorai, U. K. & Saha, S. K. White light emitting lanthanide based carbon quantum dots as toxic Cr (VI) and pH sensor. *J. Colloid Interface Sci.* **553**, 177–185 (2019).
32. Wang, R., Wang, X. & Sun, Y. One-step synthesis of self-doped carbon dots with highly photoluminescence as multifunctional biosensors for detection of iron ions and pH. *Sensors Actuators B Chem.* **241**, 73–79 (2017).
33. Ren, J., Stagi, L. & Innocenzi, P. Fluorescent carbon dots in solid-state: From nanostructures to functional devices. *Prog. Solid State Chem.* **62**, 100295 (2021).
34. Wang, J., Yang, Y. & Liu, X. Solid-state fluorescent carbon dots: Quenching

resistance strategies, high quantum efficiency control, multicolor tuning, and applications. *Mater. Adv.* **1**, 3122–3142 (2020).

35. Loures, C. C. A. *et al.* Advanced Oxidative Degradation Processes: Fundamentals and Applications. *Int. Rev. Chem. Eng.* **5**, 102 (2013).
36. EURL. *Guidance Document on the Estimation of LOD and LOQ for Measurements in the Field of Contaminants in Feed and Food*. (2016).
37. Lakowicz, J. R. *Principles of Fluorescence Spectroscopy*. (Springer, 2006).
38. Zu, F. *et al.* The quenching of the fluorescence of carbon dots: A review on mechanisms and applications. *Microchim. Acta* **184**, 1899–1914 (2017).
39. Ba, X.-X. *et al.* Thermodynamics of the Interaction Between Graphene Quantum Dots with Human Serum Albumin and γ-Globulins. *J. Solution Chem.* **49**, 100–116 (2020).

Supplementary information

Carbon dots on LAPONITE® hybrid nanocomposite: Hg^{2+} sensing and photoluminescence emission quenching mechanism

Bruno S. D. Onishi[a,*], Albano N. Carneiro Neto[b], Sidney J. L. Ribeiro[a,*]

a. Institute of Chemistry, São Paulo State University – UNESP, São Paulo, Araraquara, 14800-060, Brazil,

b. Institute of Physics and CICECO – Aveiro Institute of Materials, University of Aveiro, 3810-193 Aveiro, Portugal

*e-mail: bruno.onishi@unesp.br; sidney.jl.ribeiro@unesp.br

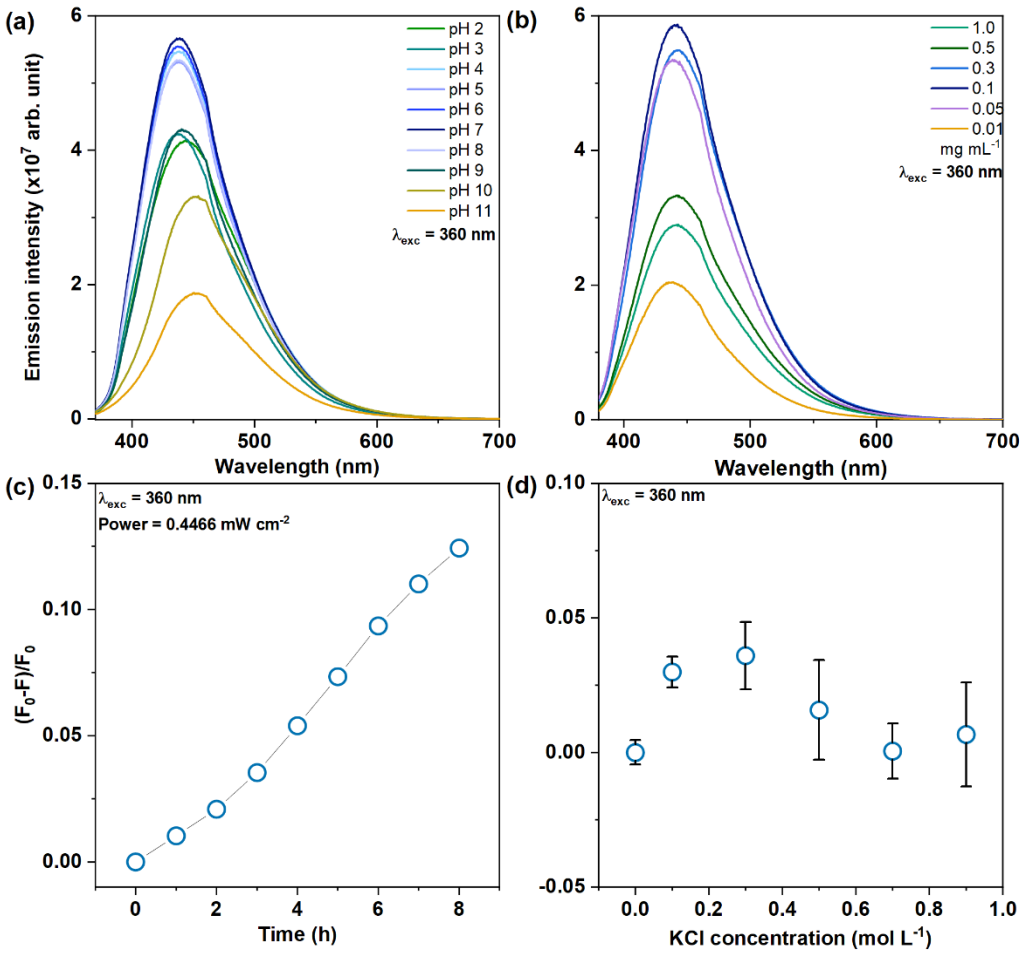

Figure 3.S1. Emission spectra of CD in function of pH (a) and concentration (b); relative integrated area of emission band in function of time (c) and ionic strength (d) – F_0 is the integrated area of the CD emission spectrum at 0h (c) and 0 mol L^{-1} KCl (d), and F is the integrated area of the CD emission spectrum at xh (c) and y mol L^{-1} (d) (x = 1 to 8h; y = 0.1 to 0.9 mol L^{-1}). For (a), (c) and (d) the CD concentration was 0.1 mg mL^{-1}.

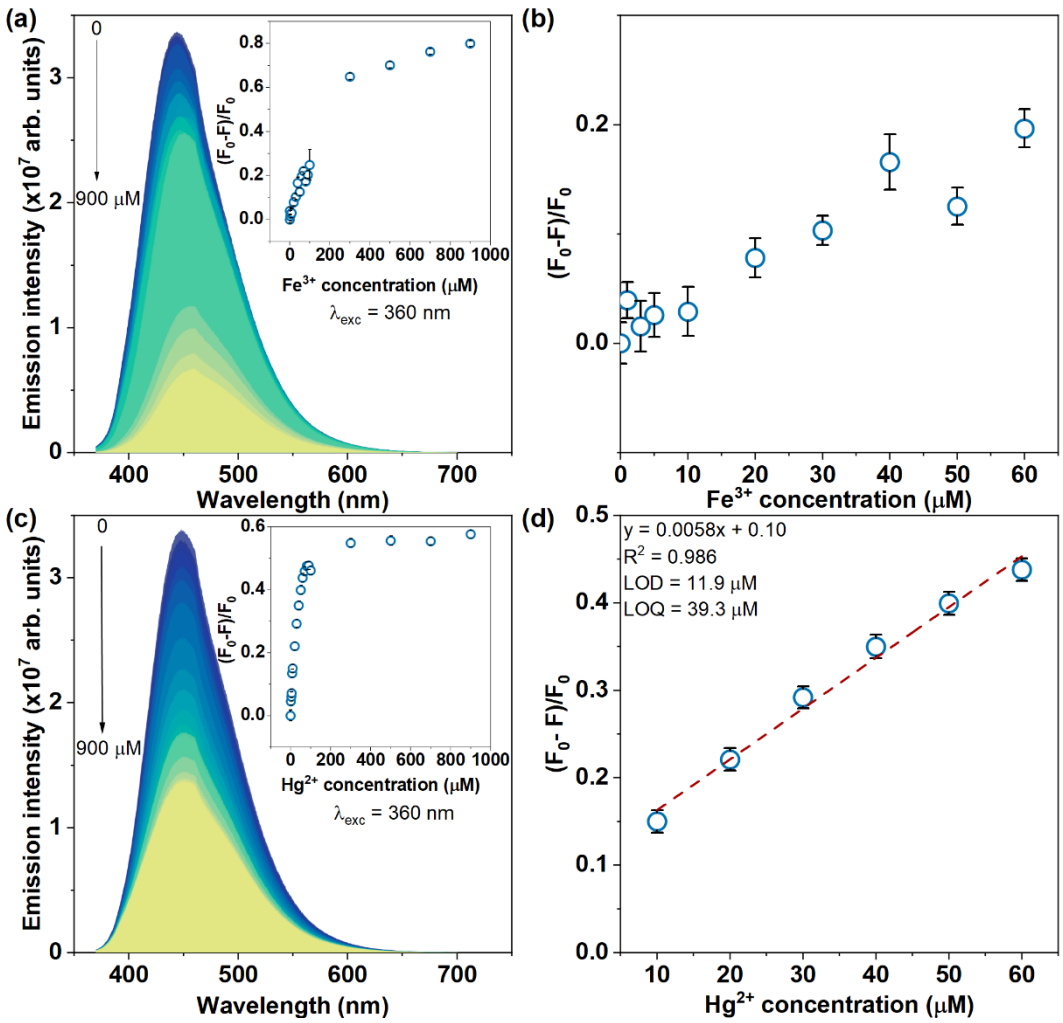

Figure 3.S2. PL emission spectra of CD in function of Fe^{3+} (a) and Hg^{2+} (b) concentration from 0 to 900 μM. The insert graph in (a) and (c) are the relative integrated emission area in function of Fe^{3+} and Hg^{2+} concentration in 0-900 μM range respectively, as well as (b) and (d) in 0-40 μM.

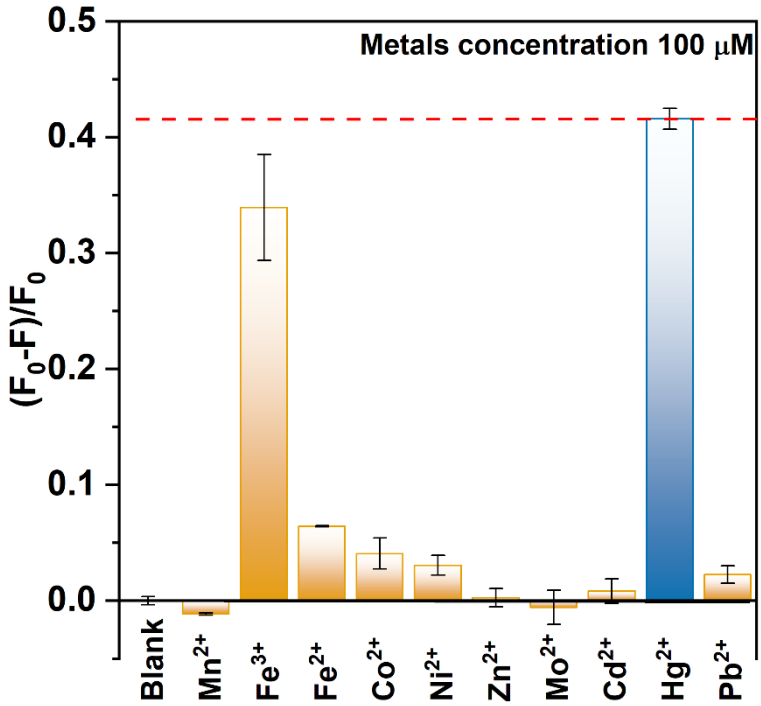

Figure 3.S3. Relative emission integrated area of CD using 100 μM of Mn^{2+}, Fe^{3+}, Fe^{2+}, Co^{2+}, Ni^{2+}, Zn^{2+}, Mo^{2+}, Cd^{2+}, Pb^{2+} (yellow bar) and with Hg^{2+} (blue bar). F_0 is the blank integrated area emission (CD) and F is the integrated area emission in the presense of the respective metals.

CHAPTER 4

LAPONITE®-modified biopolymers as a conformable substrate for optoelectronic devices

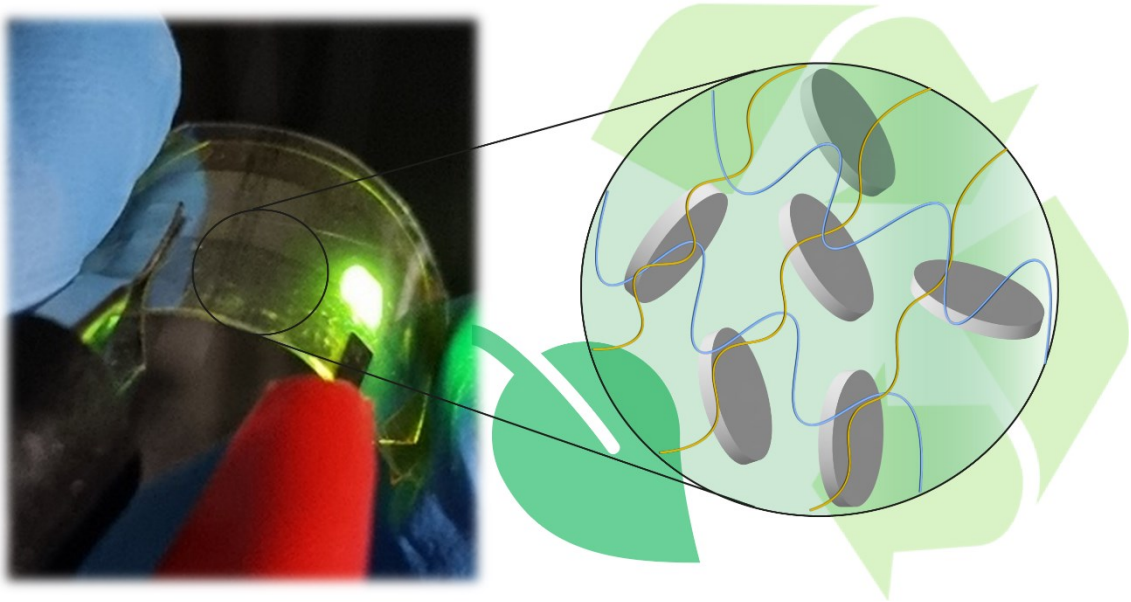

Table of Contents (TOC)/Abstract graphic: Left picture: Organic-light emitting diode (OLED) device bending while in operation. Right scheme: representation of the Carboxymethyl cellulose (orange curved line)/Hyaluronic acid (blue curved line) and Laponite® as round plate.

4. Laponite-modified biopolymers as a conformable substrate for optoelectronic devices

*Bruno S. D. Onishi[a], *Rafael S. Carvalho[c], Ricardo Bortoletto-Santos[a,b], Silvia H. Santagneli[a], Arthur R. J. Barreto[c], Aline M. Santos[c], Marco Cremona[c], Omar G. Pandoli[d,e], Mario N. B. Junior[e], Thales A. Faraco[f], Hernane S. Barud[g], Renan L. de Farias[d], Sidney J. L. Ribeiro[a,✉] Cristiano Legnani[f,✉]

[a]*Institute of Chemistry, São Paulo State University (UNESP), 14800-060 Araraquara-SP, Brazil*

[b]*Postgraduate Program in Environmental Technology, University of Ribeirão Preto (UNAERP), Ribeirão Preto, Brazil*

[c]*Departamento de Física, Pontifícia Univ. Católica do Rio de Janeiro (PUC-Rio), Rio de Janeiro, Brazil 22451-900*

[d]*Departamento de Química, Pontifícia Univ. Católica do Rio de Janeiro (PUC-Rio), Rio de Janeiro, Brazil 22451-900*

[e]*Departamento de Engenharia Química e de Materiais, Pontifícia Univ. Católica do Rio de Janeiro (PUC-Rio), Rio de Janeiro, Brazil 22451-900*

[f]*Departamento de Física, Laboratório de Eletrônica Orgânica (LEO), Univ. Federal de Juiz de Fora (UFJF), Juiz de Fora, Brazil 36036-330*

[g]*Univ. de Araraquara (UNIARA), Laboratório de biopolímeros e Biomateriais (BIOPOLMAt), Araraquara, Brazil 14801-340*

***These authors contributed equally to the work**

✉ Corresponding Authors

E-mail: sidney.jl.ribeiro@unesp.br; cristiano.legnani@ufjf.br

Abstract

Biopolymers such as carboxymethyl cellulose and hyaluronic acid are alternatives substrates for conformable organic light-emitting diodes (OLEDs). However, drawbacks as mechanical stress susceptibility can hinder the device's performance under stretched conditions. To overcome these limitations, herein we developed a nanocomposite based on CMC/HA (Carboxymethyl cellulose/Hyaluronic acid) and synthetic Laponite, intending to improve the mechanical strength without compromising the film flexibility and transparency (transmittance >80% - 380-700 nm) as substrates for conformable OLEDs. From XRD, FTIR, CP-MAS NMR, and TGA/DTG characterization techniques, it was possible to conclude the presence of Laponite randomly dispersed between the polymer chains. The CMC/HA with 5 % (wt/wt) of Laponite, CMC/HA 5, presented higher tensile strength (370.6 MPa) and comparable Young's Modulus (51.0 ± 1.2 Mpa) in comparison to the nanocomposites and pristine films, indicating a better candidate for device's substrates. To produce the OLED, the multilayer structure ITO/MoO_3/NPB/ TCTA:$Ir(ppy)_3$/TPBi:$Ir(ppy)_3$/Bphen/ LiF was deposited onto CMC/HA 5 substrate. of the OLEDs fabricated using CMC/HA 5 substrates showed higher luminance (12 kcd/m^2) and irradiance (0.9 mW/cm^2) values when compared with those based on commercial bacterial cellulose. However, the same device presented lower efficiency (3.2 cd/A) due to higher current density. Moreover, the OLED fabricated onto Laponite modified biopolymer presented a reproductible behavior when submitted to continuous bending stress. Thus, CMC/HA 5 demonstrates potential as a transparent conductor substrate for biopolymer-based OLED with comparable performance to commercial bacterial cellulose features.

Keywords: Biopolymers substrates; conformable OLED; carboxymethyl cellulose; hyaluronic acid; Synthetic clay mineral

4.1. INTRODUCTION

Biopolymers have emerged as promising alternatives to conventional polymers, characterized by their eco-friendly nature, lighter weight, biocompatibility, and cost-effectiveness[1–3]. Carboxymethyl cellulose (CMC) is a water-soluble carboxymethylated derivative composed of glucose units bound to β-1,4-glycosidic linkages with some hydroxyl replaced by anionic carboxymethyl groups[4,5]. Hyaluronic acid (HA) is found as a significant component in the extracellular matrix of animal connective tissues, having hydration and structural stabilization roles. HA comprises glycosaminoglycan polysaccharides with repeating β-1,4-d-glucuronic and β-1,3-N-acetyl-d-glucosamine units[6,7] .

Both HA and CMC biopolymers have excellent film-forming properties to produce highly transparent films for multifunctional applications such as textile, food, cosmetic, and pharmaceutical[5,8–10]. Free-standing CMC and HA-based films can be good candidates as substrates for OLEDs (organic light-emitting diodes), OFETs (organic field effect transistors), and OTFTs (organic thin film transistors)[11]. Additionally, their low-cost manufacturing over glass-based devices has been considered an advance. However, while these organic-based substrates offer benefits over the glass ones in terms of conformability, both HA and CMC biopolymer films have shown some drawbacks that should be taken into consideration, such as mechanical stress susceptibility, more sensitivity to degradation by oxygen and lower thermal stability than inorganic substrates, which can lead to device reduced performance over the time or failure.

One possibility for overcoming these limitations is the development of a polymeric composite. CMC/ HA composites were studied by Kim et al., which related the CMC content with the enhancement of the composite mechanical strength, improving the rigidity and remaining flexibility of the film[12]. Another possible strategy involves the clay minerals incorporation in the film structure, giving rise to the clay-polymer nanocomposites with improved mechanical strength and flexibility preservation[13,14]. Laponite is a synthetic clay with the empirical formula $Na^{+}_{0.7}[(Si_8Mg_{5.5}Li_{0.3})O_{20}(OH)_4]^{-}_{0.7}$ formed by tetrahedral silicate layers compressing an octahedral layer of magnesium oxide[15–17]. The octahedral center is coordinated by oxygen anions and hydroxyls, and undergoes isomorphic substitution of Mg^{2+} by Li^{+}, leading to negative charges on the surface between the layers counterbalanced by Na^{+} cations[15–19].

Properties such as mechanical strength, water permeability, and transparency of nanocomposite films based on Laponite have been investigated by some researchers. Oliveira et al. have developed a nanocomposite based on CMC - Laponite, finding an enhancement in mechanical strength and decrease in water permeability with Laponite content[11]. Interestingly, the synthetic clay did not affect the film transparency. Similar outcomes were found by Perotti et al., which combined Bacterial Cellulose (BC) with Laponite to produce a film with high tensile strength[18]. Both studies associated the H-bonding interactions between clay and polymer with mechanical strength results and highlighted the possible application of substrates as conformable OLEDs.

In the last decades, OLED technology has been growing with research interest in both industrial and academic research areas due to its characteristics such as low energy consumption, wide viewing angles, high efficiency, color purity and mechanical flexibility[20–22]. So far, high efficiency, brightness, and stability under operation have been well solved for commercial devices. However, as pointed out by Murawski and Gather[23], besides the displays in optoelectronic devices (TVs, computers, and mobile devices), OLEDs have been extensively studied for biomedical purposes, such as wearable sensors for heart rate and oxygen content in blood measurement, due to the non-invasive and biocompatibility features. Photodynamic therapy and optogenetics also were demonstrated as other possibilities of OLED technology for biomedicine. Savvatev'ev et al.[24] also reported an application as an integrated OLED-chemical sensor. The authors of these examples highlighted the low temperature and low voltage required for operation, since it works in physiological temperatures 36-39 ºC, and high temperature could damage cells or analytes in the case of integrated sensors. Thus, OLEDs based on biopolymers substrates are desirable for the advance in this field.

As an integral part of our continuous research on biopolymer-based substrates for optoelectronic devices, this study represents a significant advancement as we successfully developed a novel and conformable CMC/HA-Laponite composite. The primary objective was to reinforce the substrate while retaining its exceptional transparency and mechanical flexibility. This work not only involves the development and meticulous characterization of CMC/HA-Laponite nanocomposites as substrates for OLEDs but also serves as a compelling proof of concept for the performance of our developed OLED device in comparison to the OLED based on commercial BC.

4.2. EXPERIMENTAL SECTION

4.2.1. Materials

Hyaluronic acid sodium salt (HA) and lithium fluoride (LiF) were purchased from Sigma Aldrich. Carboxymethyl cellulose sodium salt (CMC) with M.W = 90000 (DS = 0.7) was purchased from Acros Organics. Synthetic Laponite RD was kindly supplied by Buntech (Brazil). Silicon dioxide (SiO_2) and Indium tin oxide (ITO) sputtering targets and aluminum (Al) pellets were purchased from Kurt J. Lesker Company. Molybdenum(VI) oxide (MoO_3), N,N'-Bis(naphthalen-2-yl)-N,N'-bis(phenyl)-benzidine (β-NPB), 4,4',4-Tris(carbazol-9-yl)triphenylamine (TCTA), 1,3,5-Tris(1-phenyl-1Hbenzimidazol-2-yl)benzene (TPBi), Tris(2-phenylpyridine)iridium(III) ($Ir(ppy)_3$) and 4,7-Diphenyl-1,10-phenanthroline (Bphen) were purchased from Luminescence Technology Corp. All the materials were used as received.

4.2.2. Composite films preparation

The nanocomposite films (conformable substrates) were produced using the solvent casting methodology. HA and CMC powders were mixed 50 % (weight/volume = wt/v) in a proportion of deionized water under magnetic stirring agitation at room temperature (298 K) for 24 h. The Laponite was dispersed in 10 mL of deionized water and sonicated (40kHz - 154 W) for 10 min. The percentage of lamellar material dispersed in the CMC/HA mixture was 2.5, 5 and 20 % (weight/weight = wt/wt). After 24 hours of continuous agitation, the polymer/clay mixtures were transferred to polystyrene Petri dishes (60 mm x 15 mm) and dried at 30 ºC in an air circulation oven for 48 hours. For the comparison and interpretation of the structure interactions, the individual pristine films were also prepared according to Table 4.1.

The nanocomposite films were kept in this air circulation oven just until they were transferred in the vacuum chamber for the OLED device’s fabrication.

Table 4.1 - Code and composition of each treatment

Code	Laponite® (g)	CMC (g)	HA (g)
CMC	-	0.50	-
HA	-	-	0.50
CMC/HA	-	0.50	0.50
CMC/HA 2.5	0.025	0.50	0.50
CMC/HA 5	0.050	0.50	0.50
CMC/HA 20	0.20	0.50	0.50

4.2.3. Characterization

Pristine and all prepared nanocomposites were characterized by: UV-Vis Transmittance (300-800 nm), attenuated total reflectance Fourier-Transform Infrared Spectroscopy (ATR-FTIR), X-Ray Diffraction (XRD), Thermogravimetric analysis (TGA), Solid state Cross-polarization - Magic Angle Spinning Nuclear Magnetic Resonance (CP-MAS NMR) and Mechanical properties.

Transmittance was carried out using a Cary 5000 UV–Vis-NIR spectrophotometer (Varian, USA) in the 300 – 800 nm range. ATR-FTIR spectra (400 - 4000 cm^{-1}) were collected with a NICOLET IS5 Infrared Spectrometer Thermo Scientific, employing an attenuated total reflection at iD3 module with germanium crystal, at a resolution of 2 cm^{-1} using 32 scans.

XRD pattern were obtained with a Shimadzu diffractometer / LabX XDR-6000 operating at 30 kV and 30 mA. Scans were performed in the 2θ range between 4º and 70º with a scan step of 0.02 and a Cu Kα radiation source (λ = 1.54 Å). The samples were placed in the cavity of the glass sample holder (plate, 25 mm in diameter, and 1 mm deep).

TGA ranged from 30 to 800 °C with 8 mg of each sample, at a heating rate of 10 ºC/min and synthetic air of 60 mL/min (equipment TGA-Q500/TA Instruments).

CP-MAS NMR experiments of the ^{29}Si and ^{13}C nuclei were collected in a Bruker Avance III HD 400WB spectrometer (9.4 T), using a double resonance probe of 4 mm. The experiments were conducted at a spinning speed of 10 kHz. The CP-MAS $^{29}Si\{^{1}H\}$

and $^{13}C\{^{1}H\}$ spectra were recorded using a contact time of 4.0 and 3.5 ms and a relaxation delay of 3 s, respectively. All spectra were acquired with TPPM proton decoupling during the data acquisition and chemical shifts are reported relative to TMS referencing standard.

Mechanical properties on the films was achieved using a DL-2000 (Emic®, Brazil) universal testing machine, setting with a 50 kgf load cell, initial grip separation of 10 mm, and a crosshead speed of 0.83 mm/s[25]. Mechanical parameters, such as ultimate tensile strengths and elongation at fracture, were collected by Tesc v3.04 software from the stress-strain curves. Likewise, Young's modulus was calculated as the slope of the initial linear portion of those curves.

4.2.4. OLED preparation

To validate the potential of CMC/HA 5 as a conformable substrate for OLED technology, we fabricated a multilayer device based on phosphorescent compound. Additionally, we fabricated the same OLED using a commercially available BC substrate which is a biopolymer platform reference[26]. This BC substrate, derived from bacterial cellulose, served as the control group in our study, providing a benchmark for comparison and evaluation of the OLED's performance and characteristics.

A 200 nm SiO_2 interlayer was deposited onto both polymer substrates to functionalize them, followed by 150 nm ITO[27] film used to make the substrates conductive. Both SiO_2 and ITO thin films were deposited by rf-magnetron sputtering technique in argon atmosphere. The SiO_2 film was deposited at 100 W power for a period of 90 minutes. On the other hand, the ITO film was deposited using 120 W power for 15 minutes. An argon flow rate of 30 sccm was maintained during both deposition processes.

The OLED devices were fabricated with the following structure: ITO (150 nm)/MoO_3 (2 nm)/ NPB (30 nm)/ TCTA:$Ir(ppy)_3$ (7 wt% (20 nm) /TPBi:$Ir(ppy)_3$ (7% wt% (10 nm)/ Bphen (40 nm)/ LiF (0.1 nm)/Al (100 nm), (Figure 4.S1). The organic molecules, the MoO_3, and the LiF were deposited by the thermal evaporation technique in a high vacuum environment (~10^{-4} Pa). The deposition system used for the fabrication of the devices is fully integrated within an MBraun glove box to prevent exposure of materials and devices to the ambient atmosphere. The deposition rate for the organic layers was 0.5 Å/s, and the active area of the devices was about 3 mm^2. All measurements were performed in ambient atmosphere and under ambient atmospheric conditions without any encapsulation. The

same multilayer device was also fabricated onto a commercial glass/ITO patterned substrate, from Luminescence Technology Corp. as a reference OLED[28].

4.3. RESULTS AND DISCUSSION

4.3.1. Optical and structural characterization

The prepared nanocomposite films were free-standing, transparent and macroscopically homogenous, as shown in Figure 4.1 which also reveals the good flexibility of the film without breaking or causing damage to the material. The average thickness of nanocomposite films was (100 ± 40) μm. The UV-Vis transmittance spectra are also represented in Figure 1, where it is possible to notice the high transmittance in the visible range (380-700 nm) of the substrates with low content of Laponite. 90% for CMC/HA 2.5 and 87% for CMC/HA 5. On the other hand, the Laponite-free and CMC/HA 20 films presented 80% of transmittance. Silva et al. suggests an aggregation of cellulose nanofibers promoted by Laponite, resulting in a reduction of light scattering[29]. The hypothesis could work for the low content of Laponite® in the CMC/HA films. However, higher amount of Laponite could induce some aggregation of the layers of the clay itself[30].

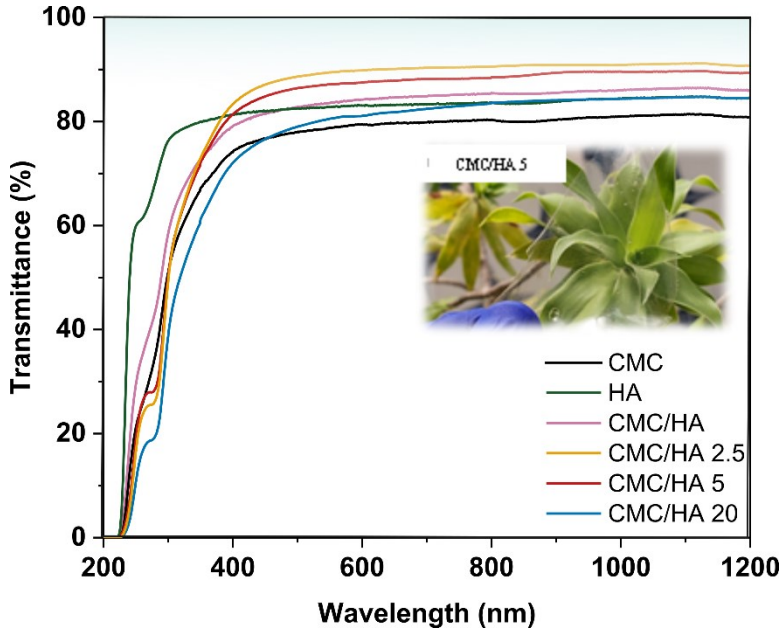

Figure 4.1. Optical transmittance of the CMC, HA, and nanocomposites films. In the inset a picture of the nanocomposite CMC/HA 5 transparent film.

ATR-FTIR spectra of the CMC/HA nanocomposite films (Figure 4.S2) revealed the combination of the bond vibrations of CMC or HA and Laponite backbones. The broad band at 3359 cm^{-1} corresponds to the OH stretching vibration from CMC and HA and can be assigned to the lattice hydroxyl groups[31,32]. The bands at 2924 and 2848 cm^{-1} are assigned to symmetric and asymmetric stretching of $-CH_2$ groups from CMC and HA structure, while the 1603 cm^{-1} band come from the -OH bending from water molecules[33,34]. The bending vibration of the $-CH_2$ group appears in 1419, 1375, and 1323 cm^{-1}, related to symmetric deformation (also known as crystallinity band), antisymmetric deformation, and wagging motion or out-of-plane deformation, respectively[29,31,33,35]. The bands at 1159 and 891 cm^{-1} correspond to the stretching of the C-O-C β-glycosidic linkage between the glucose units of CMC and HA, and the band at 1046 cm^{-1} to the C-O stretching vibration[31,35]. The band at 999 cm^{-1} is assigned to the Si-O stretching vibration of Laponite tetrahedral layers[32,36]. When the Laponite content is low, at 2.5 and 5%, this band appears as a shoulder of the CO stretching band. However, with 20% of clay mineral, the intensity is enhanced. The 652 cm^{-1} band is attributed to the Mg-OH-Mg bending vibration[32,36]. From the analysis of the ATR-FTIR spectra it was possible to verify the successful incorporation of Laponite in the nanocomposites.

Figure 4.2 shows the XRD patterns for CMC, HA, Laponite, and all prepared nanocomposites containing different amounts of Laponite. The CMC and HA diffractograms showed a typically amorphous structure with 2θ reflection of 20 and 22º, respectively. On the other hand, Laponite indicated defined peaks characteristic of a material with a crystallinity degree, as well as it is possible to notice the basal peak (001) of the lamellar material at 2θ = 7.30º with d_{001}= 1.21 ± 0.01 nm. In the XRD patterns of CMC/HA 2.5 and CMC/HA 5 nanocomposites, there are no reflections attributed to Laponite structure, suggesting the formation of an exfoliated nanocomposite[37]. However, in the case of CMC/HA 20, the reflection of the Laponite basal peak (001) at 5.36º indicates a random dispersion of exfoliated Laponite within the polymeric chains of CMC/HA. This suggests that the polymeric matrix and the lamellar material were partially combined through the exfoliation and/or tactoid formation of Laponite® in the polymeric matrix, leading to an increase in the interlayer spacing of d_{001}= 1.65 ± 0.01 nm. In addition, it can be observed that increased concentrations of Laponite in the polymer matrix promote particle agglomeration and the formation of tactoids, where some Laponite layers are stacked within the nanocomposite.

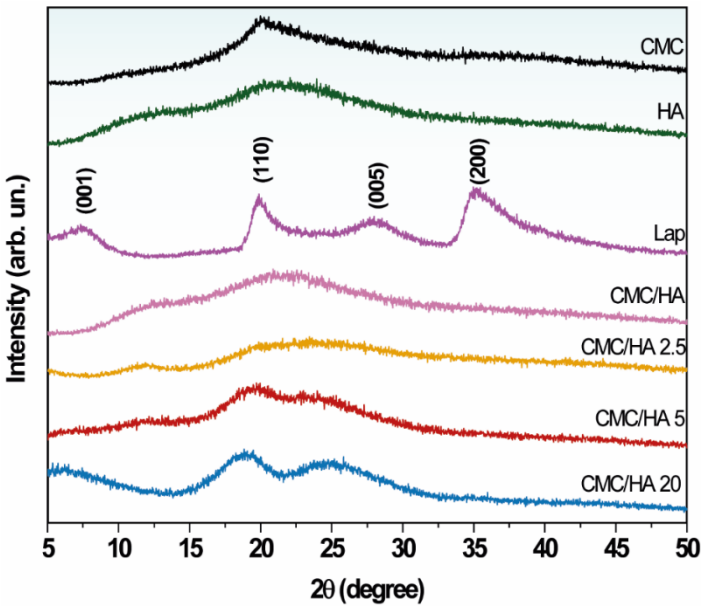

Figure 4.2. XRD patterns of CMC, HA, Lap powder and all prepared nanocomposites films.

To understand the formation and distribution of Laponite in the nanocomposite films, the solid-state ^{29}Si and ^{13}C NMR were used as a structural probe to the nanocomposites with a higher concentration of Laponite. Additionally, nanocomposite films only with CMC or HA were prepared for this analysis to verify if there was a preference for interaction between the biopolymer and the synthetic clay. From the ^{29}Si and ^{13}C nuclei chemical environments, it is possible to follow the interactions between nanocomposite films and Laponite® added. The ^{13}C NMR spectra of CMC, HA, and CMC/HA 20 are shown in Figure 4.3(a). The data for the CMC/HA 20 nanocomposite films show the characteristic peaks of the CMC and HA, confirming the success of HA incorporation. The peak at 25 ppm is characteristic of the methyl group of acetamide, and the peak at 56 ppm is relative to the C2 (N-acetylated) of HA. The broad peak observed in the 66 to 95 ppm range corresponds to carbons C-2,3,5 and C4 of the CMC, C2',4, and C- 3',4',5,5' of the HA, respectively. Additionally, the peaks at 101, 176, and 179 ppm correspond to the carbon C1 and the carbonyl peak of HA and CMC, respectively[38–40]. For ^{29}Si NMR data, depicted in Figure 4.3(b), peaks are observed at -76 and -68 ppm, characteristic of the crystalline Laponite[18], indicating that the Laponite particles were incorporated in the nanocomposite films. However, the NMR results suggest that there is no chemical interaction between Laponite and CMC/HA, also observed by Perotti et al.[18]. The results agree with those observed data by XRD, the exfoliated Laponite® are randomly dispersed into the polymeric chains of CMC/HA and the polymeric matrix. This observation is further supported by the TG/TDA analysis presented below, which indicates a decrease

in the organization of the polymeric chain with increasing Laponite concentration. The observed behavior can be attributed to the random dispersion of Laponite nanoparticles between the polymeric chains, leading to a reduction in cross-interactions among them.

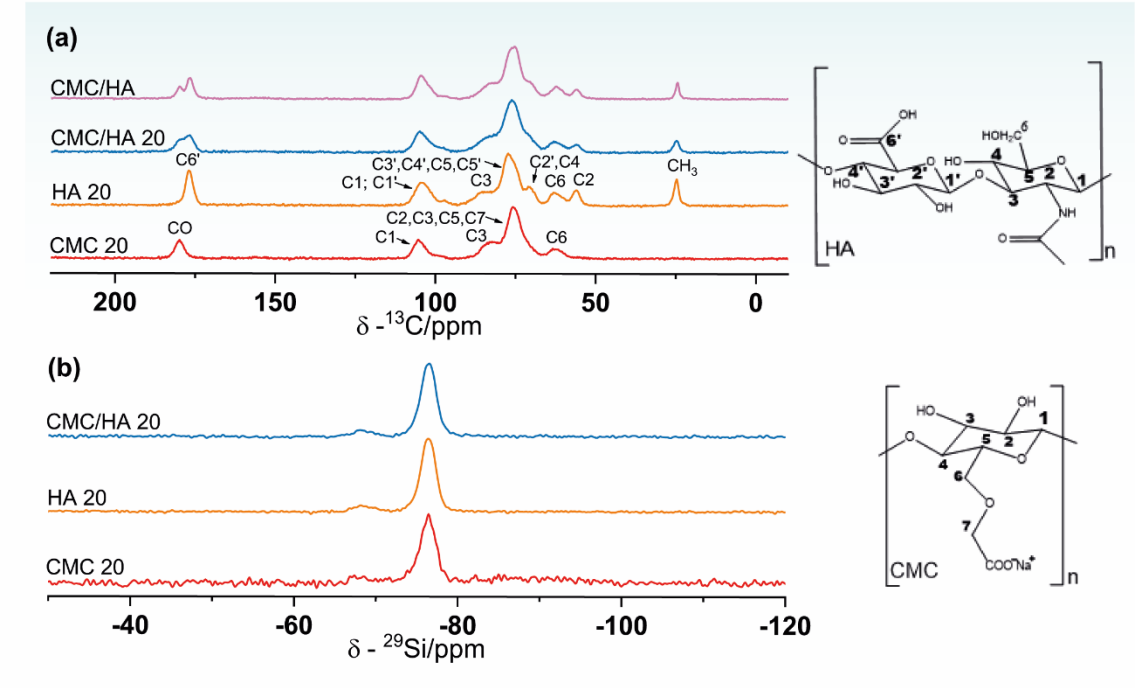

Figure 4.3. CP-MAS NMR spectra of ^{13}C (a) and ^{29}Si (b) nuclei for nanocomposite films

4.3.2. Thermal analysis

Figure 4.4 shows the TGA and derivate thermogravimetric (DTG) curves for CMC, HA, Laponite, and nanocomposites in the presence of different Laponite contents. CMC presented three mass loss processes: the first one attributed to the water loss between 30-100 ºC, the second and third processes at 277.9 and 616.8 °C were attributed to thermal degradation of cellulose from side chain degradation and CO_2 loss, and are responsible for the mass loss of 9.4, 45.6, and 27.1%, respectively[41,42]. HA showed three mass loss processes, where the first one attributed to the water loss from the material between 30-100 ºC. The second and third processes refer to the polysaccharide degradation and HA decomposition at 227.3 and 606.8 ºC, respectively[10,43,44].

The Laponite thermal profile showed two mass loss processes. The first one was attributed to the adsorbed water between 30-150 ºC with a mass loss of 8.4%. The second process occurred at 692.2 ºC and it is related to the dehydroxylation of the lamellar material layers with a mass loss of 5.2%.

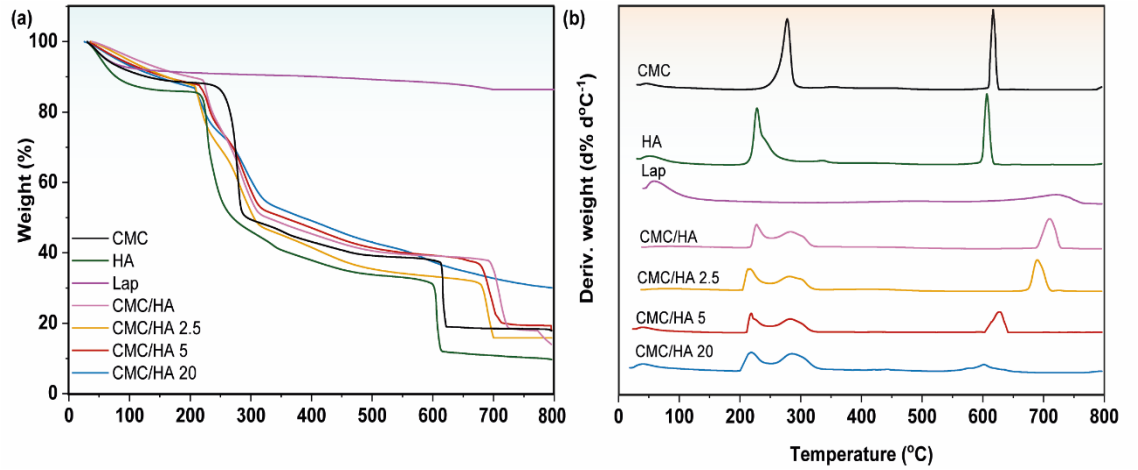

Figure 4.4. TGA (a) and DTG (b) of CMC, HA, Lap and nanocomposites films showing the main mass loss profiles.

The nanocomposites showed similar mass loss profiles with three mass loss processes. The first and second are characteristics being the HA and CMC, which make up the polymer matrix, respectively. In addition, CMC/HA also showed a third mass loss process at 710.1 ºC. From Figure 4(b), it is possible to notice that the first process for CMC/HA showed a slight reduction in temperature when compared to HA, while the second process showed an increase of 5.7 ºC about CMC. The third mass loss process showed a significant increase of 93.3 and 103.3 ºC compared to CMC and HA, respectively.

On the other hand, the nanocomposites showed a reduction in temperatures related to the HA component (first mass loss process), reaching a reduction of 11.3, 9.5, and 9.3 ºC for CMC/HA 2.5, CMC/HA 5, and CMC/HA 20. Moreover, the second mass loss process, referring to the CMC component of the polymer matrix, showed an increase in temperature between 4.5 and 8.1 ºC. The third loss process also showed a reduction for all treatments concerning CMC/HA, reaching a reduction between 20.4 - 108.4 ºC. This thermal behavior suggests a decrease of polymeric chain organization as a function of Laponite concentration and the interaction of Laponite with the polymer matrix, which influenced the polymer crystallinity in some segments. This can be associated with the random dispersion of Laponite nanoparticles between the polymeric chains, which reduces the cross interactions between them due to the physical interaction of Laponite with the polymers.

Although the films did not present stability at high temperatures, as mentioned in the introduction section, the films are still suitable for applications in the biomedical field

and integrated chemical sensors, as these applications work in low temperatures of operation, and the precursors are biocompatible.

4.3.3. Stress-Strain analysis

Mechanical parameters were examined by uniaxial tensile test (Figure 4.S3). For polymeric films, elastic deformation occurs at sufficient low stress causing the unfolding and alignment of chains, resulting in reversive changes of intermolecular forces. Accordingly, a small Young's modulus is expected for substrates with elevated susceptibility to deformation[45]. As follows, HA polymer has ultimate tensile strength (UTS) of 277.2 MPa, elongation at the break (EAB) of 30.9% and Young's modulus (YM) of 56.1 ± 1.7 MPa. On the other hands, pure CMC film, has UTS of 171.0 MPa, EAB of 9.60 %, and YM of 47.9 ± 1.4 MPa (Table 4.S2). According to the results, the CMC/HA films exhibited lower ultimate tensile strength and Young's modulus compared to the pure films, indicating reduced resistance to stretching but increased flexibility with the addition of HA to CMC. This observation is consistent with previous studies that have reported higher EAB values for CMC/HA films compared to pure CMC films[12,25,26]. However, the incorporation of 2.5 and 5% of Laponite into the CMC/HA matrix resulted in increased UTS and YM values compared to the CMC/HA films. This indicates that the addition of 2.5 and 5% of Laponite enhances the film's resistance to stretching, while still maintaining a certain degree of deformability, as evidenced by the YM values. On the other hand, with the 20% loading of the synthetic clay, the UTS lowered, probably because of the Laponite aggregation which causes a point of stress concentration, reducing the surface area of interaction between the biopolymers[46]. Nevertheless, CMC/HA 5 is more resistant to stretch than all the CMC/HA composites including the pure and CMC/HA films with 370.6 MPa of UTS, 16.5% EAB, and 51.0 ± 1.2 MPa of YM, making it a good candidate for final application as a substrate for OLED devices[47].

4.3.4. OLED characterization

Atomic Force Microscopy (AFM) measurements were performed using a Bruker model Multimode-8 operated in Peak Force mode with a tin-doped silicon cantilever (Spring constant Ks= 3N/m and resonant frequency of 75 kHz). Figures 4.5(a) and 4.5(b) show the surface morphology of the pristine CMC/HA 5 and the ITO-coated CMC/HA 5 substrates. Pristine CMC/HA 5 substrate (Figure 4.5(a)) exhibits a smooth and even

surface. However, the presence of aggregated particles can be observed at specific points. This phenomenon is generally explained by the difficulty in achieving a perfect uniformity in the filmogenic solution, uneven solvent evaporation and the aggregation of hyaluronic acid units due to interactions[44,48,49]. The observed striations can be attributed to the surface of the polystyrene Petri dishes during the solvent casting process.

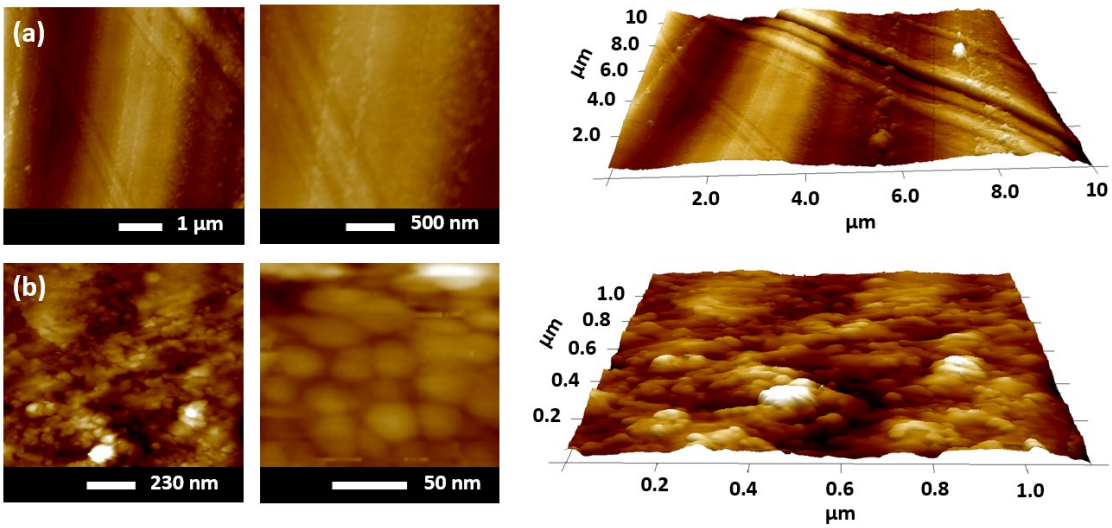

Figure 4.5. AFM surface images of the pristine CMC/HA 5 (a) and ITO-coated CMC/HA 5 substrates (b), with 2D and 3D visualization.

Figure 4.5(b) reveals the presence of ITO grains responsible for the granular appearance observed on the surface of the ITO film using AFM. The ITO film deposited on the CMC/HA 5 substrate showed an electrical resistivity of 5.0×10^{-4} Ω/m (sheet resistance of 35 Ω/□), a value very close to that exhibited by the commercial ITO-coated glass substrate[50].

This granular appearance indicates the crystalline nature of the material. During the sputtering deposition of ITO, the material undergoes rearrangement, resulting in the formation of grains in accordance with the crystallinity standards of ITO. This phenomenon is influenced by factors such as nucleation and grain growth[50]. It is widely acknowledged that ITO films exhibit a cubic bixbite polycrystalline structure[51] as confirmed by the diffraction pattern shown in Figure 4.S4, and this polycrystallinity is commonly attributed to the enhanced electrical conductivity compared to amorphous ITO[52].

Considering the well-established literature[53–56] in the field of OLEDs and structural similarity with the nanocomposite studied, the bacterial cellulose (BC) biopolymer was

selected as a reference substrate material for performance comparison with the CMC/HA 5 substrate for the fabrication of conformable OLEDs. Figure 4.6(a) shows the characteristic curves for the OLEDs based on commercial BC and based on CMC/HA 5. The maximum luminance and irradiance values for commercial BC were 5000cd/m^2 and 0.5mW/cm^2 with turn-on voltage around 3.0 V, while for CMC/HA 5 these values were 12890 cd/m^2 and 0.92mW/cm^2 for the same turn-on voltage. Both devices have an active area of about 3 mm^2 and present the $Ir(ppy)_3$ characteristic peak emission in their electroluminescence spectrum (Figure 4.6(b)). For the OLED fabricated onto glass/ITO substrate the values were: 72000cd/m^2, 8.4 mW/cm^2 with EQE_{max} = 8.8%.

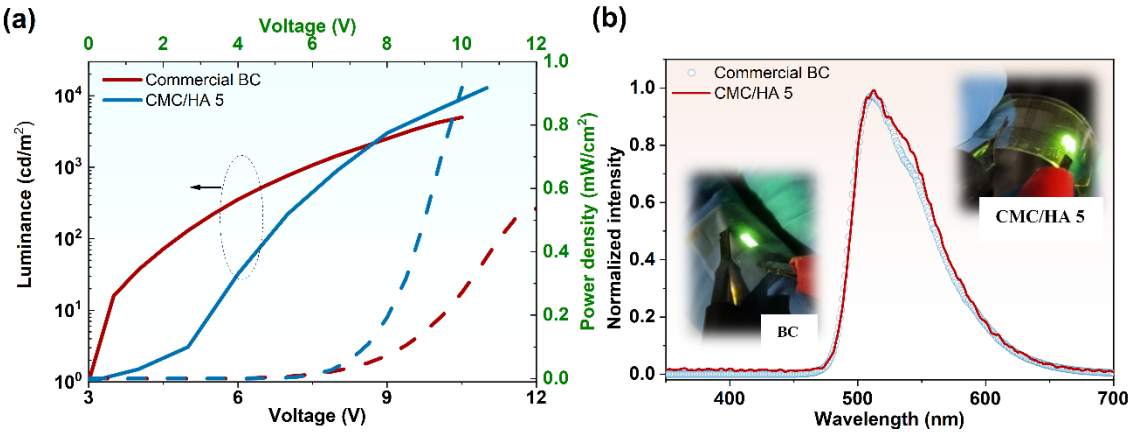

Figure 4.6. (a) Characteristic curves of OLEDs with commercial BC and CMC/HA 5; solid curves associated with luminance measurements and dash curves with power density; (b) Electroluminescence spectra of OLEDs fabricated onto commercial BC and CMC/HA 5. In the inset: pictures of the fabricated devices;

Even though CMC/HA 5-based OLED produces more than twice the luminance and irradiance of the commercial BC-based device, in terms of efficiency, it shows four times less (EQE 2.5% CMC/HA 5 and 10% commercial BC, @1000cd/m2) due to its higher current density. However, it is evident that the overall performance of CMC/HA 5-based OLED as a conformable and biocompatible substrate is comparable with those based on commercial BC with additional features mentioned previously. In order to demonstrate the CMC/HA 5 substrate conformability, we performed two different bending tests (Figure 4.7)[57]. In the first test we measured JxV curves for each configuration from 0V to 10V with 0.5V step. The cycle is: extended OLED – bent (r = 4mm) OLED. After ten cycles the current density became lower than the first sweep. It can indicates that the device electrode (SiO_2/ITO), after many cycles, starts to experience some losses in the

conduction properties due to the bend of the substrate. In the second bending test, 10V were applied continuously in two configurations: 30s the device was left extended, then the device was bent (r = 4mm) for more 30s. After some cycles, besides the typical current density drift (Figure 4.7b – red line), the current density stops to experience decrease and reach a saturation regime.

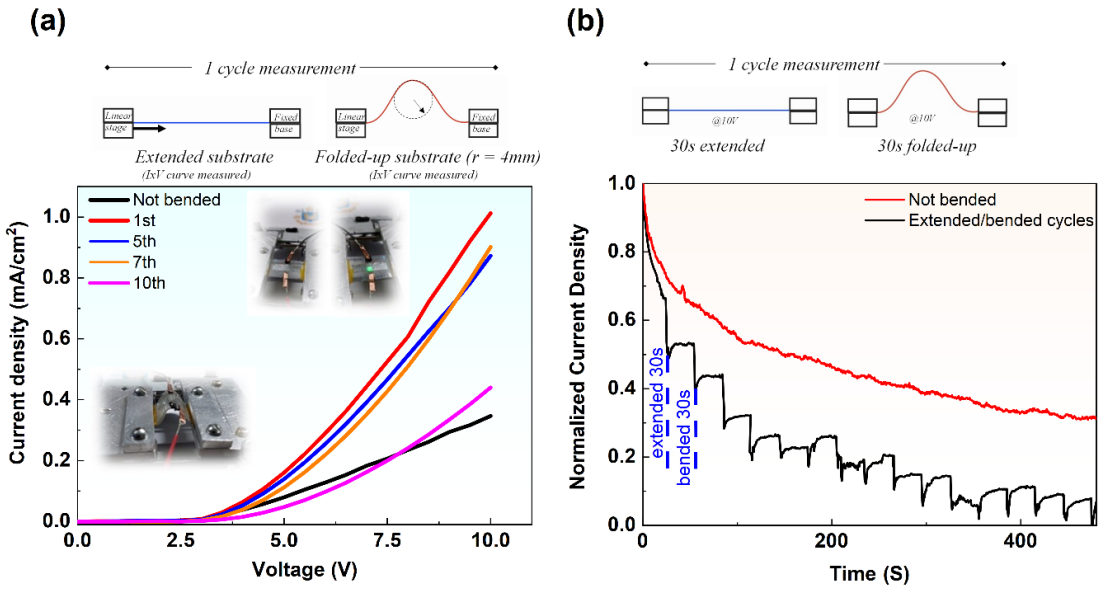

Figure 4.7. (a) First bending test: current density x voltage curves for 10 cycles of flexibility test. (b) second bending test: current density values as function of time for several bending cycles. The red line is the current density drift of a not bended device.

4.4. CONCLUSION

The nanocomposite films based on CMC/HA and Laponite successfully produced by solvent casting technique presented flexibility and high transmittance in comparison with the films without the synthetic clay. Based on the overall characterization, the Laponite was incorporated in the polymeric matrix randomly dispersed between the polymeric chains. Among the samples, CMC/HA 5 demonstrated superior performance for conformable OLEDs, as indicated by the stress-strain analysis, showcasing high tensile strength of 370.6 MPa and the ability to withstand deformation without breaking. This flexibility enables the OLED device to operate in stretched conditions. Additionally, the AFM results confirmed the successful coating of ITO on the CMC/HA 5 films, enabling the development of the OLED device. The comparative analysis of OLEDs fabricated with commercial BC and CMC/HA 5 substrates reveals similar characteristics and performance metrics. While the CMC/HA 5-based OLED demonstrated higher maximum luminance (12 kcd/m^2) and irradiance (0.9 mW/cm^2) values compared to the commercial

BC-based device, its efficiency was compromised by the higher current density. Overall, the study highlights the potential of CMC/HA 5 as a viable substrate option with comparable performance to commercial BC and additional conformability feature, offering additional advantageous features for future biocompatible OLED advancements.

DECLARATION OF COMPETING INTEREST

The authors declare that they have no known competing financial interests or personal relationships that could have appeared to influence the work reported in this paper.

ACKNOWLEDGMENTS

The authors are grateful for the financial support given by CAPES (Finance Code 001) for the scholarship. Additionally, thanks to CNPq (Grants 309614/2021-0;312086/2022-9; INCT-INFO; 312086/2022-9), FAPESP (Grant 2013/07276-1), FAPEMIG (Grant APQ-03319-18), FINEP (Grant 01.16.0065.04), FAPERJ, INCT of Polysaccharides and INCT-INEO.

REFERENCES

(1) Zhu, Y.; Romain, C.; Williams, C. K. Sustainable Polymers from Renewable Resources. *Nature* **2016**, *540* (7633), 354–362. https://doi.org/10.1038/nature21001.

(2) Wang, Z.; Ganewatta, M. S.; Tang, C. Sustainable Polymers from Biomass: Bridging Chemistry with Materials and Processing. *Prog. Polym. Sci.* **2020**, *101*, 101197. https://doi.org/10.1016/j.progpolymsci.2019.101197.

(3) Filiciotto, L.; Rothenberg, G. Biodegradable Plastics: Standards, Policies, and Impacts. *ChemSusChem* **2021**, *14* (1), 56–72. https://doi.org/10.1002/cssc.202002044.

(4) Zhivkov, A. M. Electric Properties of Carboxymethyl Cellulose. In *Cellulose - Fundamental Aspects*; InTech, 2013. https://doi.org/10.5772/56935.

(5) Rahman, M. S.; Hasan, M. S.; Nitai, A. S.; Nam, S.; Karmakar, A. K.; Ahsan, M. S.; Shiddiky, M. J. A.; Ahmed, M. B. Recent Developments of Carboxymethyl Cellulose. *Polymers (Basel).* **2021**, *13* (8), 1345. https://doi.org/10.3390/polym13081345.

(6) Gupta, R. C.; Lall, R.; Srivastava, A.; Sinha, A. Hyaluronic Acid: Molecular Mechanisms and Therapeutic Trajectory. *Front. Vet. Sci.* **2019**, *6* (JUN). https://doi.org/10.3389/fvets.2019.00192.

(7) Fallacara, A.; Baldini, E.; Manfredini, S.; Vertuani, S. Hyaluronic Acid in the Third Millennium. *Polymers (Basel).* **2018**, *10* (7), 701. https://doi.org/10.3390/polym10070701.

(8) Panahirad, S.; Dadpour, M.; Peighambardoust, S. H.; Soltanzadeh, M.; Gullón, B.; Alirezalu, K.; Lorenzo, J. M. Applications of Carboxymethyl Cellulose- and Pectin-Based Active Edible Coatings in Preservation of Fruits and Vegetables: A Review. *Trends Food Sci. Technol.* **2021**, *110* (November 2020), 663–673. https://doi.org/10.1016/j.tifs.2021.02.025.

(9) Kanikireddy, V.; Varaprasad, K.; Jayaramudu, T.; Karthikeyan, C.; Sadiku, R. Carboxymethyl Cellulose-Based Materials for Infection Control and Wound Healing: A Review. *Int. J. Biol. Macromol.* **2020**, *164*, 963–975. https://doi.org/10.1016/j.ijbiomac.2020.07.160.

(10) Lopez, K. M.; Ravula, S.; Pérez, R. L.; Ayala, C. E.; Losso, J. N.; Janes, M. E.; Warner, I. M. Hyaluronic Acid–Cellulose Composites as Patches for Minimizing Bacterial Infections. *ACS Omega* **2020**, *5* (8), 4125–4132. https://doi.org/10.1021/acsomega.9b03852.

(11) Oliveira, R. L. de; Barud, H. da S.; De Salvi, D. T. B.; Perotti, G. F.; Ribeiro, S. J. L.; Constantino, V. R. L. Transparent Organic–Inorganic Nanocomposites Membranes Based on Carboxymethylcellulose and Synthetic Clay. *Ind. Crops Prod.* **2015**, *69*, 415–423. https://doi.org/10.1016/j.indcrop.2015.02.015.

(12) Kim, S.; Cho, D.-H.; Kweon, D.-K.; Jang, E.-H.; Hong, J.-Y.; Lim, S.-T. Improvement of Mechanical Properties of Orodispersible Hyaluronic Acid Film by Carboxymethyl Cellulose Addition. *Food Sci. Biotechnol.* **2020**, *29* (9), 1233–1239. https://doi.org/10.1007/s10068-020-00771-1.

(13) Mukhopadhyay, R.; Bhaduri, D.; Sarkar, B.; Rusmin, R.; Hou, D.; Khanam, R.; Sarkar, S.; Kumar Biswas, J.; Vithanage, M.; Bhatnagar, A.; Ok, Y. S. Clay–Polymer Nanocomposites: Progress and Challenges for Use in Sustainable Water Treatment. *J. Hazard. Mater.* **2020**, *383* (August), 121125. https://doi.org/10.1016/j.jhazmat.2019.121125.

(14) Okada, A.; Usuki, A. Twenty Years of Polymer-Clay Nanocomposites. *Macromol. Mater. Eng.* **2006**, *291* (12), 1449–1476. https://doi.org/10.1002/mame.200600260.

(15) Zhao, L. Z.; Zhou, C. H.; Wang, J.; Tong, D. S.; Yu, W. H.; Wang, H. Recent Advances in Clay Mineral-Containing Nanocomposite Hydrogels. *Soft Matter* **2015**, *11* (48), 9229–9246. https://doi.org/10.1039/C5SM01277E.

(16) Becher, T. B.; Braga, C. B.; Bertuzzi, D. L.; Ramos, M. D.; Hassan, A.; Crespilho, F. N.; Ornelas, C. The Structure–Property Relationship in LAPONITE® Materials: From Wigner Glasses to Strong Self-Healing Hydrogels Formed by Non-Covalent Interactions. *Soft Matter* **2019**, *15* (6), 1278–1289. https://doi.org/10.1039/C8SM01965G.

(17) Misra, C.; Ranganathan, V. T.; Bandyopadhyay, R. Influence of Medium Structure on the Physicochemical Properties of Aging Colloidal Dispersions Investigated Using the Synthetic Clay LAPONITE®. *Soft Matter* **2021**, *17* (41), 9387–9398. https://doi.org/10.1039/D1SM00987G.

(18) Perotti, G. F.; Barud, H. S.; Messaddeq, Y.; Ribeiro, S. J. L.; Constantino, V. R. L. Bacterial Cellulose–Laponite Clay Nanocomposites. *Polymer (Guildf).* **2011**, *52* (1), 157–163. https://doi.org/10.1016/j.polymer.2010.10.062.

(19) Domeneguetti, R. R.; Sakai, V. Y.; Perotti, G. F.; Silva, I. C.; Tercjak, A.; Barud, H. S.; Pavan, F.; Constantino, V. R. L.; Ribeiro, S. J. Structural and Morphological Properties of In-Situ Biosynthesis of Biocompatible Bacterial Cellulose/Laponite Nanocomposites. *Appl. Clay Sci.* **2023**, *234* (May 2022), 106851. https://doi.org/10.1016/j.clay.2023.106851.

(20) Hu, X.; Aizawa, N.; Kim, M.; Huang, M.; Li, Z.; Liu, G.; Gao, H.; Gao, T.; Dong, X.; Zhang, Y.; Liu, J.; Wang, P.; Yi, Y.; Pu, Y.-J.; Wang, Y. Dual-Acceptor Thermally Activated Delayed Fluorescence Emitters: Achieving High Efficiency and Long Lifetime in Orange-Red OLEDs. *Chem. Eng. J.* **2022**, *434* (January), 134728. https://doi.org/10.1016/j.cej.2022.134728.

(21) Han, T.-H.; Lee, Y.; Choi, M.-R.; Woo, S.-H.; Bae, S.-H.; Hong, B. H.; Ahn, J.-H.; Lee, T.-W. Extremely Efficient Flexible Organic Light-Emitting Diodes with Modified Graphene Anode. *Nat. Photonics* **2012**, *6* (2), 105–110. https://doi.org/10.1038/nphoton.2011.318.

(22) Zou, Y.; Hu, J.; Yu, M.; Miao, J.; Xie, Z.; Qiu, Y.; Cao, X.; Yang, C. High-Performance Narrowband Pure-Red OLEDs with External Quantum Efficiencies up to 36.1% and Ultralow Efficiency Roll-Off. *Adv. Mater.* **2022**, *34* (29), 2201442. https://doi.org/10.1002/adma.202201442.

(23) Murawski, C.; Gather, M. C. Emerging Biomedical Applications of Organic Light-Emitting Diodes. *Adv. Opt. Mater.* **2021**, *9* (14), 2100269. https://doi.org/10.1002/adom.202100269.

(24) Savvate'ev, V.; Chen-Esterlit, Z.; Aylott, J. W.; Choudhury, B.; Kim, C.-H.; Zou, L.; Friedl, J. H.; Shinar, R.; Shinar, J.; Kopelman, R. Integrated Organic Light-Emitting

Device/Fluorescence-Based Chemical Sensors. *Appl. Phys. Lett.* **2002**, *81* (24), 4652–4654. https://doi.org/10.1063/1.1518154.

(25) Mussagy, C. U.; Remonatto, D.; Picheli, F. P.; Paula, A. V.; Herculano, R. D.; Santos-Ebinuma, V. C.; Farias, R. L.; S. D. Onishi, B.; J. L. Ribeiro, S.; F. B. Pereira, J.; Pessoa Jr, A. A Look into Phaffia Rhodozyma Biorefinery: From the Recovery and Fractionation of Carotenoids, Lipids and Proteins to the Sustainable Manufacturing of Biologically Active Bioplastics. *Bioresour. Technol.* **2022**, *362* (August), 127785. https://doi.org/10.1016/j.biortech.2022.127785.

(26) Cebrian, A. V. S.; Carvalho, R. S.; Barreto, A. R. J.; Maturi, F. E.; Barud, H. S.; Silva, R. R.; Legnani, C.; Cremona, M.; Ribeiro, S. J. L. Development of Conformable Substrates for OLEDs Using Highly Transparent Bacterial Cellulose Modified with Recycled Polystyrene. *Adv. Sustain. Syst.* **2022**, *6* (2), 2000258. https://doi.org/10.1002/adsu.202000258.

(27) Yu, Z.; Perera, I. R.; Daeneke, T.; Makuta, S.; Tachibana, Y.; Jasieniak, J. J.; Mishra, A.; Bäuerle, P.; Spiccia, L.; Bach, U. Indium Tin Oxide as a Semiconductor Material in Efficient P-Type Dye-Sensitized Solar Cells. *NPG Asia Mater.* **2016**, *8* (9), e305. https://doi.org/10.1038/am.2016.89.

(28) Baldo, M. A.; Lamansky, S.; Burrows, P. E.; Thompson, M. E.; Forrest, S. R. Very High-Efficiency Green Organic Light-Emitting Devices Based on Electrophosphorescence. *Appl. Phys. Lett.* **1999**, *75* (1), 4–6. https://doi.org/10.1063/1.124258.

(29) Silva, J. M.; Barud, H. S.; Meneguin, A. B.; Constantino, V. R. L.; Ribeiro, S. J. L. Inorganic-Organic Bio-Nanocomposite Films Based on Laponite and Cellulose Nanofibers (CNF). *Appl. Clay Sci.* **2019**, *168* (September 2018), 428–435. https://doi.org/10.1016/j.clay.2018.12.003.

(30) Wu, W.; Dong, Z.; He, J.; Yu, J.; Zhang, J. Transparent Cellulose/Laponite Nanocomposite Films. *J. Mater. Sci.* **2016**, *51* (8), 4125–4133. https://doi.org/10.1007/s10853-016-9735-8.

(31) Cichosz, S.; Masek, A. IR Study on Cellulose with the Varied Moisture Contents: Insight into the Supramolecular Structure. *Materials (Basel).* **2020**, *13* (20), 4573. https://doi.org/10.3390/ma13204573.

(32) Mahdavinia, G. R.; Ettehadi, S.; Amini, M.; Sabzi, M. Synthesis and Characterization of Hydroxypropyl Methylcellulose-g-Poly(Acrylamide)/LAPONITE®

RD Nanocomposites as Novel Magnetic- and PH-Sensitive Carriers for Controlled Drug Release. *RSC Adv.* **2015**, *5* (55), 44516–44523. https://doi.org/10.1039/C5RA03731J.

(33) Md Salim, R.; Asik, J.; Sarjadi, M. S. Chemical Functional Groups of Extractives, Cellulose and Lignin Extracted from Native Leucaena Leucocephala Bark. *Wood Sci. Technol.* **2021**, *55* (2), 295–313. https://doi.org/10.1007/s00226-020-01258-2.

(34) Habibi, N. Preparation of Biocompatible Magnetite-Carboxymethyl Cellulose Nanocomposite: Characterization of Nanocomposite by FTIR, XRD, FESEM and TEM. *Spectrochim. Acta Part A Mol. Biomol. Spectrosc.* **2014**, *131*, 55–58. https://doi.org/10.1016/j.saa.2014.04.039.

(35) Oh, S. Y.; Yoo, D. Il; Shin, Y.; Seo, G. FTIR Analysis of Cellulose Treated with Sodium Hydroxide and Carbon Dioxide. *Carbohydr. Res.* **2005**, *340* (3), 417–428. https://doi.org/10.1016/j.carres.2004.11.027.

(36) Madejová, J.; Gates, W. P.; Petit, S. IR Spectra of Clay Minerals. In *Developments in Clay Science*; 2017; Vol. 8, pp 107–149. https://doi.org/10.1016/B978-0-08-100355-8.00005-9.

(37) Liu, J.; Boo, W. J.; Clearfield, A.; Sue, H. J. Intercalation and Exfoliation: A Review on Morphology of Polymer Nanocomposites Reinforced by Inorganic Layer Structures. *Mater. Manuf. Process.* **2006**, *21* (2), 143–151. https://doi.org/10.1080/AMP-200068646.

(38) Pouyani, T.; Harbison, G. S.; Prestwich, G. D. Novel Hydrogels of Hyaluronic Acid: Synthesis, Surface Morphology, and Solid-State NMR. *J. Am. Chem. Soc.* **1994**, *116* (17), 7515–7522. https://doi.org/10.1021/ja00096a007.

(39) de Oliveira, S. A.; da Silva, B. C.; Riegel-Vidotti, I. C.; Urbano, A.; de Sousa Faria-Tischer, P. C.; Tischer, C. A. Production and Characterization of Bacterial Cellulose Membranes with Hyaluronic Acid from Chicken Comb. *Int. J. Biol. Macromol.* **2017**, *97*, 642–653. https://doi.org/10.1016/j.ijbiomac.2017.01.077.

(40) Hernández, M.; Leyva, G.; Magaña, J. J.; Guzmán-Vargas, A.; Felipe, C.; Lara, V.; Lima, E. New Copolymers as Hosts of Ribosomal RNA. *BMC Chem.* **2019**, *13* (1), 33. https://doi.org/10.1186/s13065-019-0555-1.

(41) Abe, T. O.; Lajide, L.; Owolabi, B. J.; Adebayo, A. O.; Ogunjobi, J. K.; Oluwasina, O. O. Synthesis and Application of Carboxymethyl Cellulose from Gliricidia Sepium and Cola Gigantea. *BioResources* **2018**, *13* (3), 6077–6097. https://doi.org/10.15376/biores.13.3.6077-6097.

(42) Zhang, Y.; Li, Y.; Li, M.; Xu, M.; Yue, J. Preparation of Carboxymethyl Cellulose from Tea Stalk and Its Use as a Paper-Strengthening Agent. *Nord. Pulp Pap. Res. J.* **2019**, *34* (3), 310–317. https://doi.org/10.1515/npprj-2019-0001.

(43) Jiang, B.-P.; Zhang, L.; Zhu, Y.; Shen, X.-C.; Ji, S.-C.; Tan, X.-Y.; Cheng, L.; Liang, H. Water-Soluble Hyaluronic Acid–Hybridized Polyaniline Nanoparticles for Effectively Targeted Photothermal Therapy. *J. Mater. Chem. B* **2015**, *3* (18), 3767–3776. https://doi.org/10.1039/C4TB01738B.

(44) Ahire, J. J.; Robertson, D.; Neveling, D. P.; van Reenen, A. J.; Dicks, L. M. T. Hyaluronic Acid-Coated Poly(D, L -Lactide) (PDLLA) Nanofibers Prepared by Electrospinning and Coating. *RSC Adv.* **2016**, *6* (41), 34791–34796. https://doi.org/10.1039/C6RA01996J.

(45) Faraco, T. A.; Silva, H. de O. X.; Barud, H. D. S.; Ribeiro, T. D. C.; Maciel, I. O.; Quirino, W. G.; Fragneaud, B.; Cremona, M.; Ginoble Pandoli, O.; Legnani, C. Biosubstrates Obtained from Gellan Gum for Organic Light-Emitting Diodes. *ACS Appl. Electron. Mater.* **2021**, *3* (5), 2333–2340. https://doi.org/10.1021/acsaelm.1c00217.

(46) Sampath U. Gunathilake, T. M.; Ching, Y. C.; Chuah, C. H.; Rahman, N. A.; Nai-Shang, L. PH-Responsive Poly(Lactic Acid)/Sodium Carboxymethyl Cellulose Film for Enhanced Delivery of Curcumin in Vitro. *J. Drug Deliv. Sci. Technol.* **2020**, *58* (May), 101787. https://doi.org/10.1016/j.jddst.2020.101787.

(47) Faraco, T. A.; de O. X. Silva, H.; da S. Barud, H.; Maciel, I. O.; da Silva, R. R.; Quirino, W. G.; Fragneaud, B.; Ribeiro, C. A.; dos S. Dias, D.; G. Pandoli, O.; Cremona, M.; Legnani, C. Ecological Biosubstrates Obtained from Onion Pulp (Allium Cepa L.) for Flexible Organic Light-Emitting Diodes. *ACS Appl. Mater. Interfaces* **2019**, *11* (45), 42420–42428. https://doi.org/10.1021/acsami.9b14029.

(48) Ondreas, F.; Dusankova, M.; Sita, J.; Cepa, M.; Stepan, J.; Belsky, P.; Velebny, V. Self-Assembly of Hydrophobically Modified Hyaluronic Acid. *Appl. Surf. Sci.* **2021**, *546* (November 2020), 149161. https://doi.org/10.1016/j.apsusc.2021.149161.

(49) Kim, E. H.; Kim, G.; Lee, G. H.; Park, J. W. Nucleation and Growth of Crystalline Indium Tin Oxide (ITO) Coatings on Polyethylene Terephthalate (PET). *Surf. Coatings Technol.* **2010**, *205* (1), 1–8. https://doi.org/10.1016/j.surfcoat.2010.05.012.

(50) de Oliveira Xavier Silva, H.; Faraco, T. A.; Maciel, I. O.; Quirino, W. G.; Fragneaud, B.; Pereira, P. G.; Legnani, C. High Optoelectronic Quality of AZO Films Grown by RF-Magnetron Sputtering for Organic Electronics Applications. *Semicond. Sci. Technol.* **2023**, *38* (6). https://doi.org/10.1088/1361-6641/acd13d.

(51) Kurdesau, F.; Khripunov, G.; da Cunha, A. F.; Kaelin, M.; Tiwari, A. N. Comparative Study of ITO Layers Deposited by DC and RF Magnetron Sputtering at Room Temperature. *J. Non. Cryst. Solids* **2006**, *352* (9-20 SPEC. ISS.), 1466–1470. https://doi.org/10.1016/j.jnoncrysol.2005.11.088.

(52) Ahmed, N. M.; Sabah, F. A.; Abdulgafour, H. I.; Alsadig, A.; Sulieman, A.; Alkhoaryef, M. The Effect of Post Annealing Temperature on Grain Size of Indium-Tin-Oxide for Optical and Electrical Properties Improvement. *Results Phys.* **2019**, *13* (February), 102159. https://doi.org/10.1016/j.rinp.2019.102159.

(53) Ummartyotin, S.; Juntaro, J.; Sain, M.; Manuspiya, H. Development of Transparent Bacterial Cellulose Nanocomposite Film as Substrate for Flexible Organic Light Emitting Diode (OLED) Display. *Ind. Crops Prod.* **2012**, *35* (1), 92–97. https://doi.org/10.1016/j.indcrop.2011.06.025.

(54) Pinto, E. R. P.; Barud, H. S.; Silva, R. R.; Palmieri, M.; Polito, W. L.; Calil, V. L.; Cremona, M.; Ribeiro, S. J. L.; Messaddeq, Y. Transparent Composites Prepared from Bacterial Cellulose and Castor Oil Based Polyurethane as Substrates for Flexible OLEDs. *J. Mater. Chem. C* **2015**, *3* (44), 11581–11588. https://doi.org/10.1039/c5tc02359a.

(55) Legnani, C.; Barud, H. S.; Caiut, J. M. A.; Calil, V. L.; Maciel, I. O.; Quirino, W. G.; Ribeiro, S. J. L.; Cremona, M. Transparent Bacterial Cellulose Nanocomposites Used as Substrate for Organic Light-Emitting Diodes. *J. Mater. Sci. Mater. Electron.* **2019**, *30* (18), 16718–16723. https://doi.org/10.1007/s10854-019-00979-w.

(56) Faraco, T. A.; Fontes, M. de L.; Paschoalin, R. T.; Claro, A. M.; Gonçalves, I. S.; Cavicchioli, M.; Farias, R. L. de; Cremona, M.; Ribeiro, S. J. L.; Barud, H. da S.; Legnani, C. Review of Bacterial Nanocellulose as Suitable Substrate for Conformable and Flexible Organic Light-Emitting Diodes. *Polymers (Basel).* **2023**, *15* (3), 1–16. https://doi.org/10.3390/polym15030479.

(57) Wang, H.; Totaro, M.; Veerapandian, S.; Ilyas, M.; Kong, M.; Jeong, U.; Beccai, L. Folding and Bending Planar Coils for Highly Precise Soft Angle Sensing. *Adv. Mater. Technol.* **2020**, *5* (11), 1–13. https://doi.org/10.1002/admt.202000659.

Suplementary Material

Laponite-modified biopolymers as a conformable substrate for optoelectronic devices

*Bruno S. D. Onishi[a], *Rafael S. Carvalho[c], Ricardo Bortoletto-Santos[a,b], Silvia H. Santagneli[a], Arthur R. J. Barreto[c], Marco Cremona[c], Omar G. Pandoli[d,e], Mario N. B. Junior[e], Thales A. Faraco[f], Hernane S. Barud[g], Renan L. de Farias[d], Sidney J. L. Ribeiro[a,✉] Cristiano Legnani[f,✉]

[a] *Institute of Chemistry, São Paulo State University (UNESP), 14800-060 Araraquara-SP, Brazil*

[b]*Postgraduate Program in Environmental Technology, University of Ribeir˜ao Preto (UNAERP), Ribeir˜ao Preto, Brazil*

[c] *Departamento de Física, Pontifícia Univ. Católica do Rio de Janeiro (PUC-Rio), Rio de Janeiro, Brazil 22451-900*

[d]*Departamento de Química, Pontifícia Univ. Católica do Rio de Janeiro (PUC-Rio), Rio de Janeiro, Brazil 22451-900*

Departamento de Engenharia Química e de Materiais, Pontifícia Univ. Católica do Rio de Janeiro (PUC-Rio), Rio de Janeiro, Brazil 22451-900

[f]*Departamento de Física, Laboratório de Eletrônica Orgânica (LEO), Univ. Federal de Juiz de Fora (UFJF), Juiz de Fora, Brazil 36036-330*

[g]*Univ. de Araraquara (UNIARA), Laboratório de biopolímeros e Biomateriais (BIOPOLMAt), Araraquara, Brazil 14801-340*

***These authors contributed equally to the work**

✉ Corresponding Authors

E-mail: sidney.jl.ribeiro@unesp.br; cristiano.legnani@ufjf.br

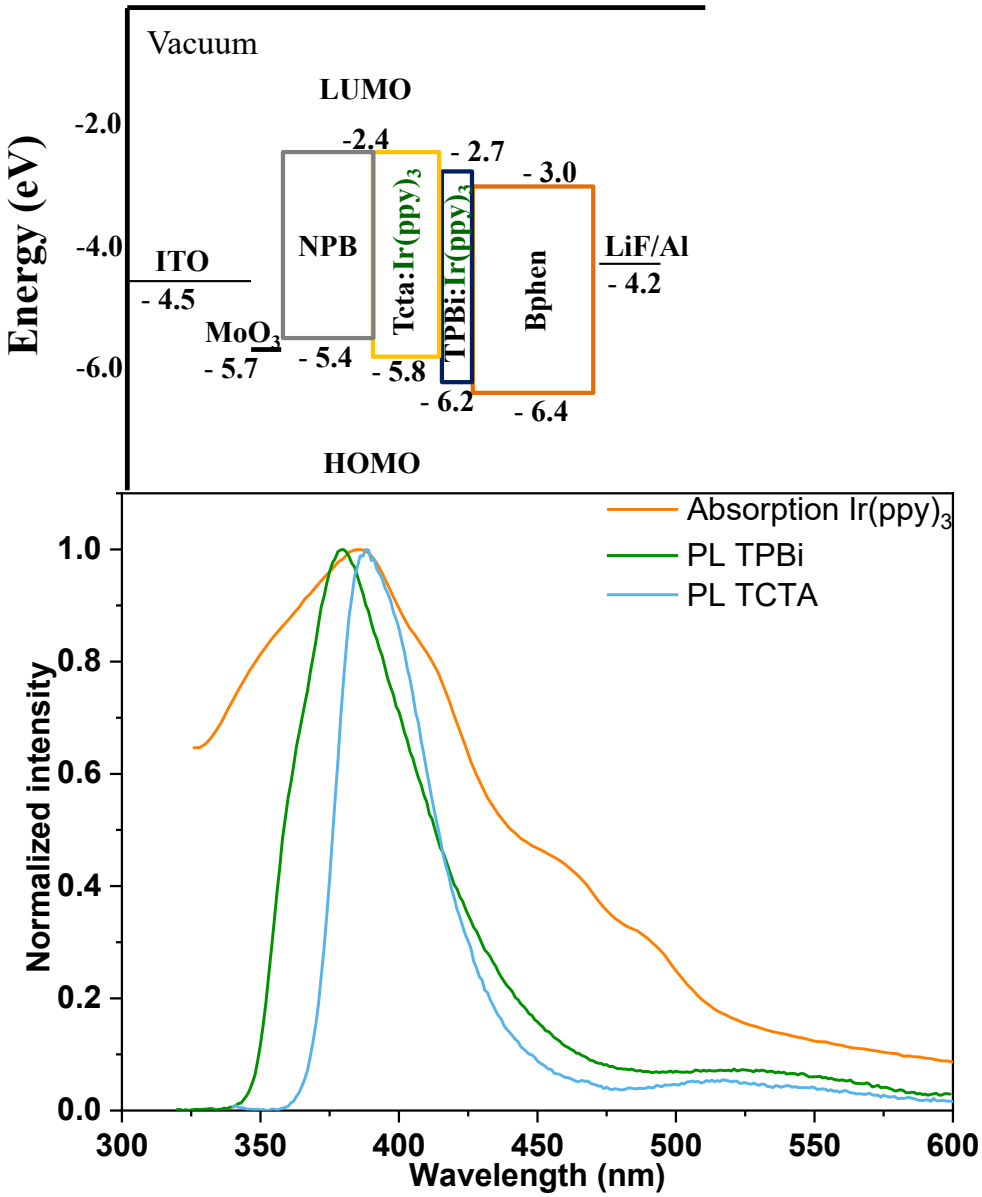

Figure 4.S1. Energy level diagram of fabricated OLED (upper) and overlap of the photoluminescence (PL) spectrum of the matrix and absorption spectrum of Ir(ppy)3 in the film solid-state (below) respectively

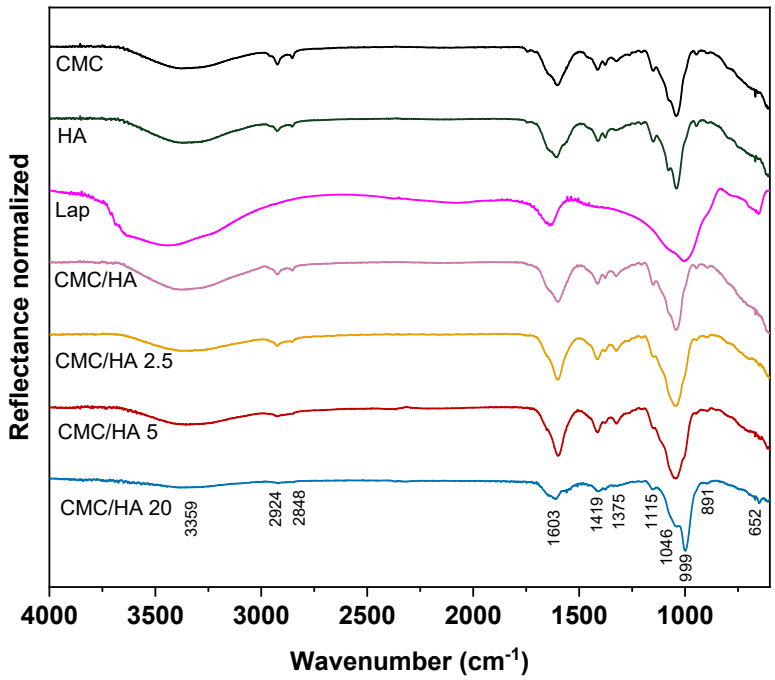

Figure 4.S2. ATR-FTIR spectra of CMC, HA, Laponite® (Lap) powder and nanocomposites films

Table 4.S1 - Process of mass loss with respective temperature and the amount of Laponite® calculated by TGA and DTG curves

Treatments	**Maximum temperature of mass loss processes (°C)**			**TGA residue (%)**	**Calculated Laponite® (%) or (g)**	
CMC	-	277.6	616.8	17.87	-	-
HA	227.9	-	606.8	9.67	-	-
CMC/HA	227.3	283.3	710.1	13.77	-	-
CMC/HA 2.5	216.6	283.2	689.7	15.82	2.39	0.025
CMC/HA 5	218.4	282.1	627.5	18.11	5.0	0.052
CMC/HA 20	218.6	285.7	601.7	30.07	19.05	0.240

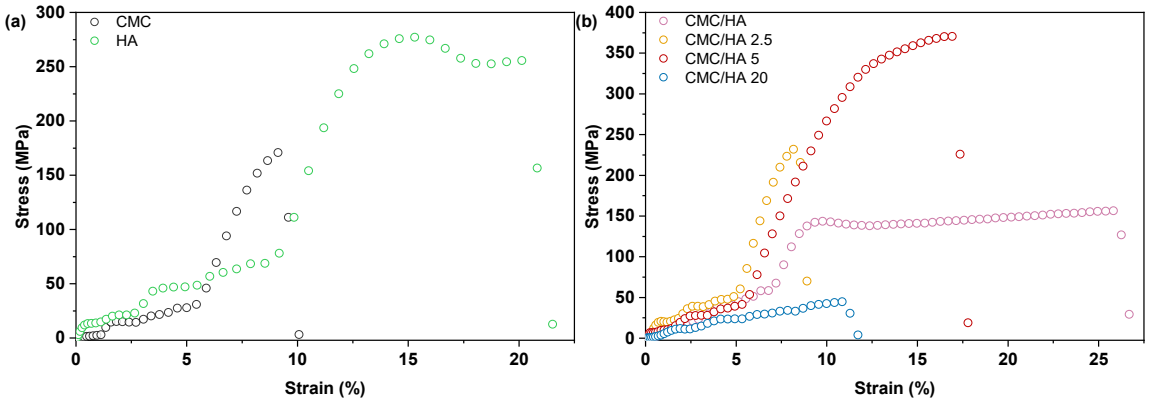

Figure 4.S3. Stress-strain curves for the CMC, HA films (a) and CMC/HA, CMC/HA 2.5, CMC/HA 5, and CMC/HA 20 films (b). Experimental conditions: load cell of 50 kgf and crosshead rate 0.83 mm s^{-1}, at room temperature.

Table 4.S2 - Tensile strength, elongation at break and Young's modulus of CMC, HA, and nanocomposites films

Specimen	Tensile Strength (MPa)	Elongation (%)	Young's modulus (MPa)
CMC	171.0	9.60	47.9 ± 1.4
HA	277.2	30.9	56.1. ± 1.7
CMC/HA	143.7	25.8	40.26 ± 2.7
CMC/HA 2.5	232.0	7.80	69.6. ± 2.4
CMC/HA 5	370.6	16.5	51.0 ± 1.2
CMC/HA 20	44.80	10.4	40.3± 2.7

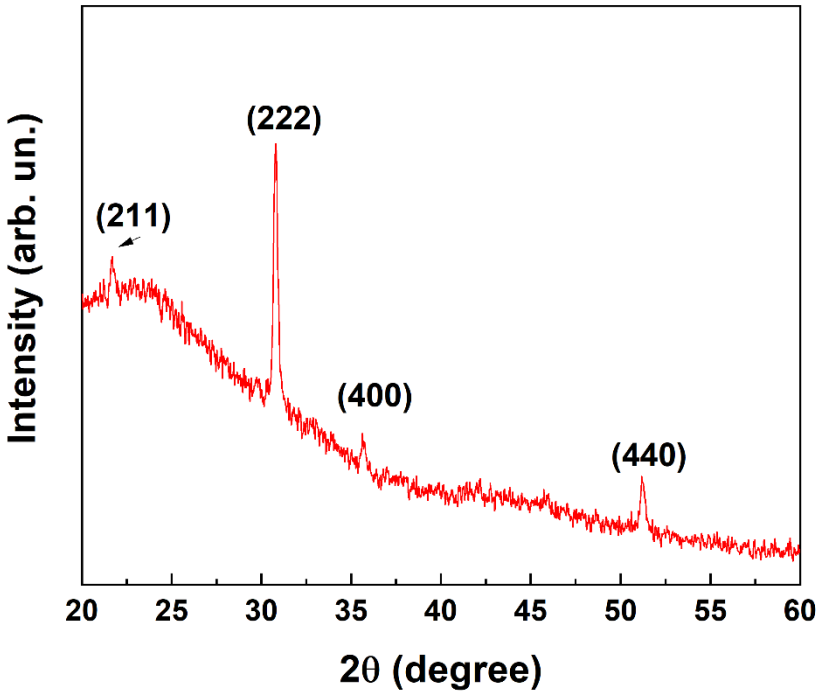

Figure 4.S4. X-ray diffraction pattern of the ITO-coated CMC/HA 5 substrate reveals crystal planes corresponding to (211), (222), (400), and (440).

CHAPTER 5

General conclusions and perspectives

5. General conclusions and perspectives

This section provides a general conclusion of the chapters, discusses the relationship between the chapters, and addresses the work's limitations and perspectives.

According to the developed PhD research, nanocomposites based on CDs-clay minerals can be synthesized using the in situ-hydrothermal method. However, more purification methods should be developed for solid-state CDs in powder form. Although conventional CDs are typically purified using dialysis and column chromatography, these methods are still experimentally challenging for solid-state soluble water CDs. It is important to understand the physical-chemical features of the clay mineral, mainly its possible interactions with the reaction medium, as their structures can have pH-dependent charges and permanent charges that impact the final microstructures. Clay minerals can act as nanoplatforms for CDs synthesis, creating confined spaces for nanoparticle formation and influencing the final structure and PL properties. Additionally, clay minerals can provide the steric hindrance necessary between CDs to resist quenching. However, the quantum yield values found are still low compared to water suspension samples, necessitating improvements. One proposed solution is to directly bind the CDs to the clay mineral structure through chemical modification using the CDs precursors, followed by *in situ*-hydrothermal synthesis. The high-energy states associated with by-products or the CDs' core undergo quenching in solid-state form, while the surface states in low energy remain stable. Energy transfer processes between CDs aggregates are involved in the PL emission properties of solid-state CDs, which should be explored for other CDs structures. Additionally, a universal protocol should be established for CDs synthesis, as the core structure is not fully defined and is highly dependent on synthesis conditions.

Due to the ability to suspend the samples in water and the presence of carboxylate functional groups on the surface, the nanocomposite could be applied for Hg^{2+} detection in water in the 1 – 40 μM range. It showed better performance for Hg^{2+} detection compared to CDs synthesized without LAPONITE®. It was also possible to verify the influence of pH and concentration on sample photostability. Using Stern-Volmer models at different temperatures, it was possible to verify the preference for complexation over collisional quenching, and the sensor is not fully accessible to the quencher. However, analysis in real water samples should be conducted to evaluate the nanocomposite's applicability. Additionally, studies of sorption-desorption and kinetics of Hg^{2+} with the

nanocomposite and zeta potential analysis of the sensors could provide more physical-chemical details between the sensor and quencher interactions. Both chapters 2 and 3 offer insights into the applicability of LAPONITE® for nanocomposite synthesis involving CDs and as PCS, demonstrating the potential of this clay mineral in the photonic field.

Chapter 4 explored another application of LAPONITE® in the photonic field, specifically for the fabrication of nanocomposites based on biopolymers for OLED substrates. The clay mineral remains randomly dispersed in the CMC/HA mixture, but higher concentrations hinder the film's tensile strength properties. Thus, a limit of 5% was established (between 2.5%, 5%, and 20%) to enhance tensile strength without compromising flexibility. The results obtained from OLED characterization showed that improvements are needed to smooth the surface to enhance OLEDs' EQE. One possibility is to change the film formation method (solvent casting) or the substrate. Additionally, heat treatment during ITO deposition could facilitate the formation of highly crystalline and uniform grains. Although the efficiency is lower compared to BC commercial substrates, the values of luminance and irradiance prove to be higher, demonstrating potential applications mainly in biological systems, where the input voltage is lower and low working temperatures are needed. Studies of the thermal coefficient must be conducted in relation to LAPONITE® concentration to achieve low values, reducing the difference between the substrate and metal layers and avoiding higher thermal stress, as displays can generate heat during operation and temperature fluctuations can occur during device manufacturing and usage.

In conclusion, the knowledge acquired through this thesis includes:

- Synthesis of nanocomposites
- Synthesis of CDs and solid-state emissive CDs
- Nanomaterials characterization techniques
- PL properties
- Application of PL for PCS
- Evaluation of quenching mechanisms
- Synthesis of biopolymer films and nanocomposites
- Film characterization.

ATTACHMENTS

The articles included in Chapter 2 of this thesis were reused in accordance with the licenses, copyrights, and permissions provided by the Royal Society of Chemistry, as detailed at available at RSC Author Information

The graphic below (available at RSC Permissions Flowchart) outlines the process for obtaining permission to reuse RSC materials when the author of the material wishes to reuse their own work.

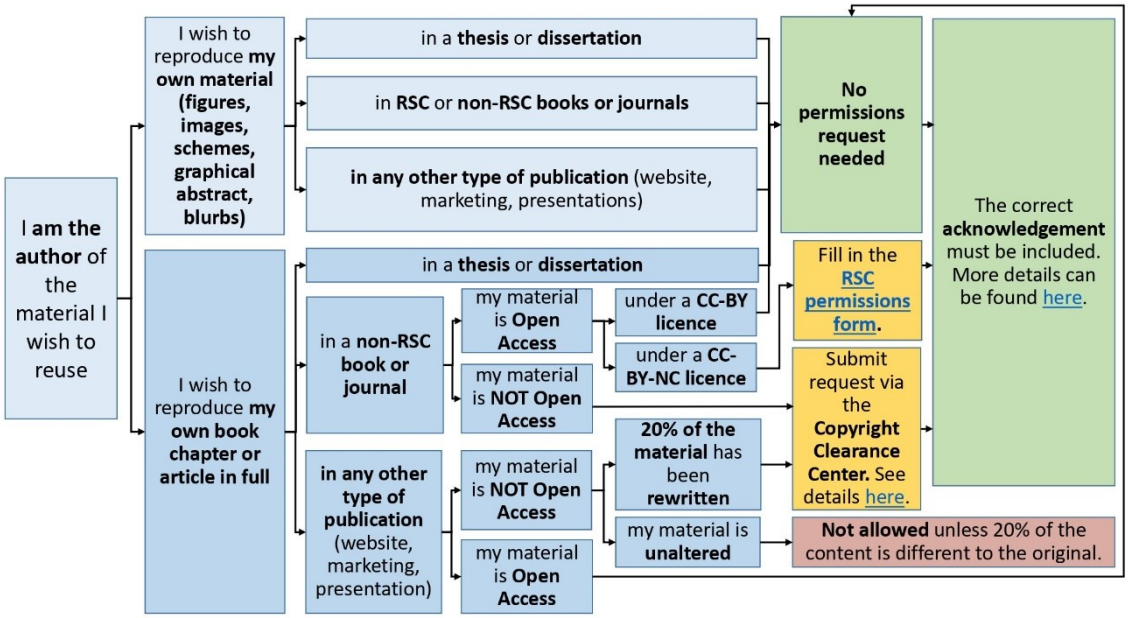

As illustrated in the figure, no permission request is necessary to reproduce one's own articles in full within a thesis or dissertation.

Chapter 2 B. S. D. Onishi *et al. Nanoscale* 2024, Nanoscale, 2024, 16, 6286. Available at http://doi.org/10.1039/d3nr06336d Copyright © 2024 Royal Society of Chemistry.